CALIFORNIA STATE UNIVERSITY, NORTHRIDGE

^{238}U-^{230}Th disequilibrium dating of chevkinite from La Primavera, Jalisco, Mexico

A thesis submitted in partial fulfillment of the requirements
for the degree of Master of Science
in Geology

by

Noel Odorico Velasco

August 2010

The thesis of Noel Odorico Velasco is approved:

Axel K. Schmitt, Ph.D.	Date
Elena A. Miranda, Ph.D.	Date
Jorge A. Vazquez, Ph.D., Chair	Date

California State University, Northridge

DEDICATION

To my loved ones.

ACKNOWLEDGMENT

I thank Dr. Jorge Vazquez for his exceptional dedication and enthusiasm as my advisor, I could never thank him enough. I thank Dr. Elena Miranda and Dr. Axel Schmitt for being in my thesis committee. I thank Dr. Kathleen Marsaglia for all her help and guidance. I thank the Catalyst program mentors and all the faculty and staff of the Department of Geological Sciences at CSUN.

TABLE OF CONTENTS

LIST OF FIGURES

LIST OF TABLES

ABSTRACT

^{238}U-^{230}Th disequilibrium dating on chevkinite from La Primavera, Jalisco, Mexico

by

Noel Odorico Velasco

Master of Science in

Geology

This thesis describes a new ion microprobe method for dating the accessory mineral chevkinite using *in situ* ion microprobe measurement of 238U-230Th disequilibrium. Chevkinite is an accessory mineral found in igneous rocks ranging from kimberlites to peralkaline granites and rhyolites, it also contains high concentrations of U and Th (up to 2 wt %) which makes it a good candidate for the application of U-Th dating. Our study analyzes chevkinite and zircon grains from four La Primavera domes. The ages obtained from chevkinite and zircon for each given sample overlap within error confirming that U-Th disequilibrium dating on chevkinite can be used as a geochronology proxy. Chevkinite model and isochron ages were measured. Sample LP001 yield a model age of $88.5^{40.7}_{29.6}$ ka and an isochron age of 100 ± 120 ka (MSWD=2.5), sample LP002B yield a model age of $84.0^{40.7}_{29.6}$ka and an isochron age of 91 ± 120 ka (MSWD = 3.1), and sample LP008 yield a model age of $49.4^{29.4}_{23.1}$ka and an isochron age of 54 ± 84 ka (MSWD = 3.3). Zircon model and isochron ages were measured. Sample LP001 yields a model age of $104.9^{14.9}_{13.1}$ka and an isochron age of 115 ± 39 ka (MSWD = 0.47), sample LP002B yield a model age of $113.6^{17.2}_{14.8}$ ka and an isochron age of 113 ± 48 ka (MSWD = 0.7), sample LP006 yield a model age of $74.1^{12.4}_{11.1}$ka and an isochron age of 56 ± 24 ka (MSWD = 0.47), and sample LP008 yields a model age of $101.0^{23.1}_{19.1}$ka and an isochron age of 102 ± 28 ka (MSWD = 0.7). Finally, the isochron ages for each samples LP001, LP002B, and LP008 were calculated using all chevkinite and zircon measurements of each sample. Sample LP001 yield a chevkinite-zircon isochron age of 102.3 ± 4.1 ka (MSWD = 1.2), sample LP002B yield a chevkinite-zircon isochron age of 108.7 ± 8.2 ka (MSWD = 1.8), and Sample LP008 yield a chevkinite-zircon isochron age of 92 ± 12 ka (MSWD = 2.3).

Chapter I

Introduction

Caldera volcanoes such as Yellowstone, Long Valley, and Toba have the ability to produce some of the largest and most destructive eruptions on Earth (Newhall and Dzurisn, 1988). These large volcanic eruptions are geologically and biologically significant because they may generate aerially extensive deposits which in turn may cause global climate change (Rampino and Self, 1992) and influence human and biota evolution (Rampino and Self, 1993; Bailey 2000). Long-lived caldera systems, such as Toba and Yellowstone, are characterized by long (10^5-10^6 years) periods of quiescence between large eruptions (Chesner *et al.*, 1991; Christiansen *et al.*, 2007). In the interval between eruptions, caldera magma reservoirs may experience episodes of magma recharge, cooling-induced crystallization, and/or re-melting (Hildreth *et al.*, 1984, 1991; Spell *et al.*, 1993; Bindeman and Valley, 2001; Costa, 2008). However, the timescales associated with magma storage and differentiation at long-lived caldera volcanoes are unclear.

Geochronology using short-lived nuclides may provide a detailed chronology of magma storage and evolution prior to eruption. Since the repose between eruptions and magmatic evolution occurs over timescales on the order of 10^5 years, the ^{238}U-^{230}Th system has been used to determine the absolute ages of crystallization, and in turn, magma/crystal residence prior to eruption because of the relatively short half life of ^{230}Th (e.g., Reid *et al.,* 1997; Bacon *et al.*, 2000; Lowenstern *et al.*, 2000; Heumann *et al.*, 2002; Vazquez and Reid, 2002). Early ^{238}U-^{230}Th dating of accessory minerals used multi-grain aliquots (e.g., Fukuoka and Kigoshi, 1974; Charlier and Zellmer, 2000;

Heumann *et al.*, 2002) such that high-resolution crystallization records (i.e., core to rim ages) of single crystals were essentially impossible to resolve. In the last decade, the advent of ^{238}U-^{230}Th-^{206}Pb dating of young zircon (Reid *et al.*, 1997; Brown and Fletcher, 1999; Bacon *et al.*, 2000; Lowenstern *et al.*, 2000; Reid and Coath, 2000) and allanite (Vazquez and Reid, 2004) using high resolution secondary ion mass spectrometry (SIMS) has allowed *in situ* dating of single crystals, particularly zircon (see review by Schmitt, 2009). Zircon has proven to be a robust chronometer of magma evolution because of its high U content, its resistance to alteration, and because U-Th-Pb diffusion is insignificant even at magmatic temperatures (Cherniak and Watson, 2003). Although zircon may contain significant zoning in the concentrations of rare earth elements (REE) and Hf (Hoskin and Shaltegger, 2003), the partitioning relation between crystal and melt are poorly known (Heaman *et al.,* 1990; Hoskin and Shaltegger, 2003) and hence the magma evolution recorded by single zircons is unclear.

In situ geochronology using Th- and U-rich accessory minerals that host a variety of REE and "major" elements such as Mg, Ti, and Mn, may provide unique information about magma composition during crystallization (e.g., Vazquez and Reid, 2004; Simon *et al.*, 2009; Schmitt, 2009). Vazquez and Reid (2004) used ion microprobe ^{238}U-^{230}Th dating of allanite (Th-LREE rich epidote-group mineral) from the Youngest Toba Tuff to demonstrate that the Toba magma underwent a relatively long-lived period of stagnation followed by magma and crystal mixing circa 35 ka before eruption. Simon *et al.*(2009) compared $^{40}Ar/^{39}Ar$, and allanite-zircon ^{238}U-^{230}Th ages to demonstrate that reliable magma crystallization ages can be obtained from different accessory minerals. Allanite may have compositional zoningdue to changing magma composition during

crystallization (Chesner and Ettlinger, 1989; Vazquez and Reid, 2004) and is relatively large compared to the size of the ion microprobe primary beam (Vazquez and Reid, 2004).

Similar to allanite, chevkinite is a Th-LREE rich accessory mineral with potential for determining the absolute age of magma crystallization and differentiation via ion microprobe ^{238}U-^{230}Th dating. However, chevkinite differs from allanite in that it is essentially anhydrous and has high concentrations of Ti. In metaluminous rhyolites, chevkinite appears to generally occur at higher temperatures than allanite (Izett and Wilcox, 1968; Vazquez *et al.*, 2004; Robinson and Miller, 1999). Chevkinite occurs in a variety of igneous and metamorphic rocks, and even inclusions in diamonds (Macdonald and Belkin, 2002). In addition to La Primavera caldera, volcanic chevkinite is reported in a variety of metaluminous and alkaline rhyolites, including Yellowstone lavas and tuffs (Izett and Wilcox, 1968; Hildreth *et al.*, 1984; Macdonald and Belkin 2002; Vazquez, 2008), East African rhyolites (Macdonald *et al.*, 2002; Lowenstern *et al.*, 2005), and Canarian trachytes (Troll *et al.*, 2003). The high concentration of Th and large fractionation between Th and U makes chevkinite an ideal mineral for ^{238}U-^{230}Th dating (Vazquez, 2008; Schmitt, 2009). Volcanic chevkinite typically contains between 9-25 weight % $(Ce, La)_2O_3$ and 1-2 weight % ThO_2, with large vaues of LREE/HREE, Th/U, and Nb/Ta (Macdonald and Belkin, 2002; Troll *et al.*, 2003).

In this study, I performed ion microprobe analyses to evaluate the feasibility and utility of ^{238}U-^{230}Th disequilibrium dating of Pleistocene chevkinite by comparing the ages of coexisting and/or intergrown chevkinite and zircon microphenocrysts from La Primavera rhyolites. In addition, I evaluated the utility of a Himalayan chevkinite as a

standard for measurement of ^{238}U-^{230}Th secular equilibrium. La Primavera caldera was chosen for this study for the following reasons: 1) La Primavera rhyolites contain euhedral chevkinites that appear cogenate to their host magmas (Michael, 1988), 2) La Primavera chevkinites coexist with zircons that can be used as an independent check of ^{238}U-^{230}Th ages, 3) The eruption ages and stratigraphic relations of the host rhyolites are established by field relations and K-Ar dating of sanidine and whole rock glass (Mahood, 1980, 1981, 1988), and 4) The petrologic evolution of La Primavera rhyolites is established by several published studies (e.g., Mahood, 1981; Mahood and Halliday, 1988).

For this study I sampled four eruptive units of La Primavera and obtained chevkinite isochron and model ages, zircon isochron and model ages, and chevkinite-zircon isochron ages. Chevkinite model and isochron ages for samples LP001, LP002B, and LP008 were measured. Sample LP001 yields a model age of $88.5^{40.7}_{29.6}$ka and an isochron age of 100 ± 120 ka (MSWD=2.5), sample LP002B yields a model age of $84.0^{40.7}_{29.6}$ka and an isochron age of 91 ± 120 ka (MSWD = 3.1), and sample LP008 yields a model age of $49.4^{29.4}_{23.1}$ka and an isochron age of 54 ± 84 ka (MSWD = 3.3). Also, zircon model and isochron ages for samples LP001, LP002B, LP006, and LP008 were measured. Sample LP001 yields a model age of $104.9^{14.9}_{13.1}$ka and an isochron age of 115 ± 39 ka (MSWD = 0.47), sample LP002B yields a model age of $113.6^{17.2}_{14.8}$ka and an isochron age of 113 ± 48 ka (MSWD = 0.7), sample LP006 yields a model age of $74.1^{12.4}_{11.1}$ka and an isochron age of 56 ± 24 ka (MSWD = 0.47), and sample LP008 yields a model age of $101.0^{23.1}_{19.1}$ka and an isochron age of 102 ± 28 ka (MSWD = 1.6). Finally, the isochron ages for samples LP001, LP002B, and LP008 were calculated using all

chevkinite and zircon measurements of each sample. Sample LP001 yields a chevkinite-zircon isochron age of 102.3 ± 4.1 ka (MSWD = 1.2), sample LP002B yields a chevkinite-zircon isochron age of 108.7 ± 8.2 ka (MSWD = 1.8), and Sample LP008 yields a chevkinite-zircon isochron age of 92 ± 12 ka (MSWD = 2.3).

Chapter II

Geologic Background of La Primavera Caldera

La Primavera caldera is a major Quaternary volcano located adjacent to the city of Guadalajara, Jalisco, Mexico. La Primavera is situated in the northwestern portion of the Trans-Mexican Volcanic Belt (TMVB) and the southern end of the Cordillera Province in Mexico (Figure 1). The TMVB is a 20-150 km wide, 1000 km long, 2000 m high volcanic plateau which extends across central Mexico from the Pacific Ocean to the Gulf of Mexico. Andesitic and dacitic compositions dominate the eruptive products in the TMVB region; a minority of TMVB volcanoes have erupted silicic and alkaline magmas (Urrutia-Fucugauchi and Böhnel, 1988). The Cordillera Province extends along the Sierra Madre Occidental from the Pacific coast up to 400 km inland. The Cordillera Province is composed of about 1700 m of Tertiary-aged ignimbrite sheets overlain by olivine basalt and basaltic andesite (Gunn and Mooser, 1969). La Primavera caldera is located on the Tepic-Zacoalco rift (Figure 2). The Tepic-Zacoalco rift intersects with the Chapala and the Colima rifts about 50 km SSW of the city of Guadalajara. These three extensional zones create a rifting triple junction (Nelson and Hegre, 1990; Rossotti *et al.*,2002). Peralkaline volcanism occurs within the Tepic-Zacoalco rift at La Primavera and Tequila Volcano, in the area around Guadalajara, and near Pachuca in central Mexico. These volcanic centers have erupted high silica peralkaline rhyolites (comendite) with Las Navajas having erupted rhyolites of pantelleritic composition (Nelson and Hegre, 1990). Rhyolites at La Primavera are mildly peralkaline and highly evolved (SiO_2: ~76 weight %)(Mahood, 1981). In total, La Primavera has erupted 50-60 km^3 (dense rock equivalent) of rhyolite (Walker *et al.*, 1981).

La Primavera rhyolites reflect a protracted volcanic history that spans nearly 100 ka in duration (Mahood, 1980). Multiple eruptions have generated a series of rhyolitic domes and lavas that are scattered over 500 km^2 (Appendix 1)(Walker *et al.*, 1981). Volcanism can be divided into major phases of explosive and effusive eruptions based on the work of Mahood (1980, 1982) (summarized in Table 1):

1. Eruption of pre-caldera porphyritic and aphyric domes and flows between 120 ka and 100 ka.
2. Explosive eruption of 20 km^3 rhyolitic Tala Tuff over a 700 km^2 area at ca. 95 ka and concomitant formation of ~11-km diameter caldera.
3. Post-collapse eruption of several rhyolitic domes ("central domes" and "older ring domes") at ca. 95 ka in the center and margins of the lake-filled caldera. The older ring domes contain about 10% phenocrysts and represent approximately 5 km^3 of magma.
4. After an approximate 20 ka hiatus, eruption of approximately 3 km^3 of aphyric and porphyritic rhyolite ("younger ring domes") at ca. 75 ka.
5. Resurgence of caldera floor at ca. 60 ka.
6. Eruption of approximately 7 km^3 of aphyric rhyolite flows and domes ("southern arc lavas") between ca. 60 ka and ca. 30 ka.

Numerous hot springs around La Primavera reflect an active hydrothermal system driven by heat from underlying intrusions (new or residual) (Walker *et al.*, 1981).

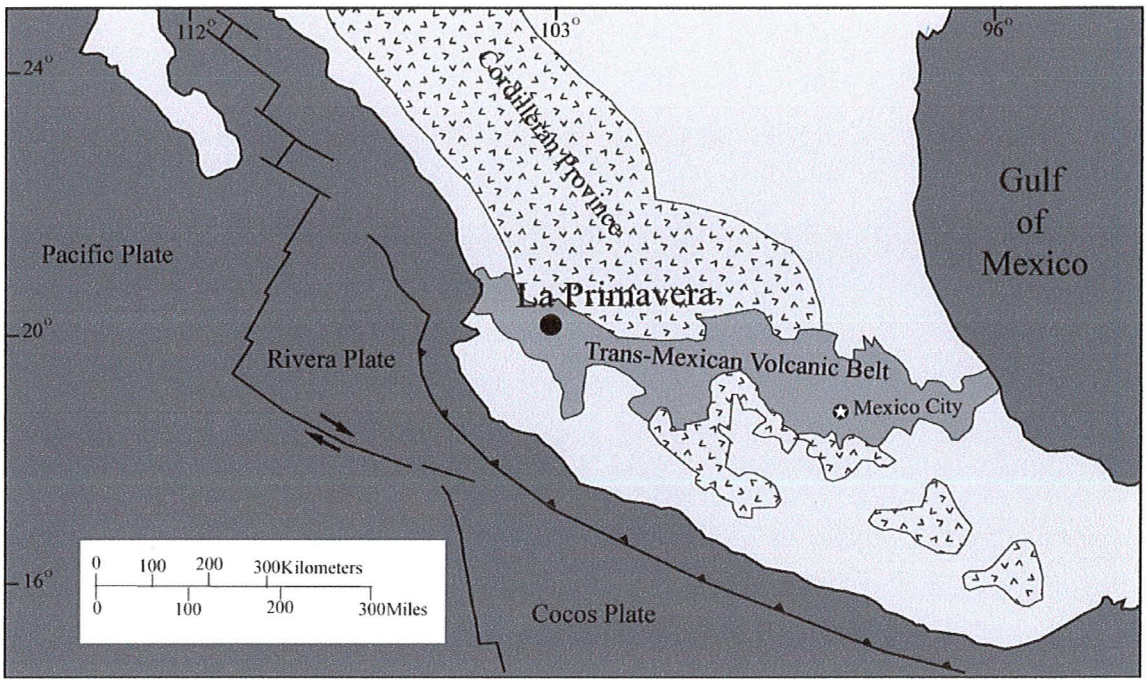

Figure 1 Map of central Mexico showing the locality of La Primavera caldera (black circle) with respect to the Cordilleran Province and the Trans-Mexican Volcanic Belt. Figure after Ferrari *et al.*(2000).

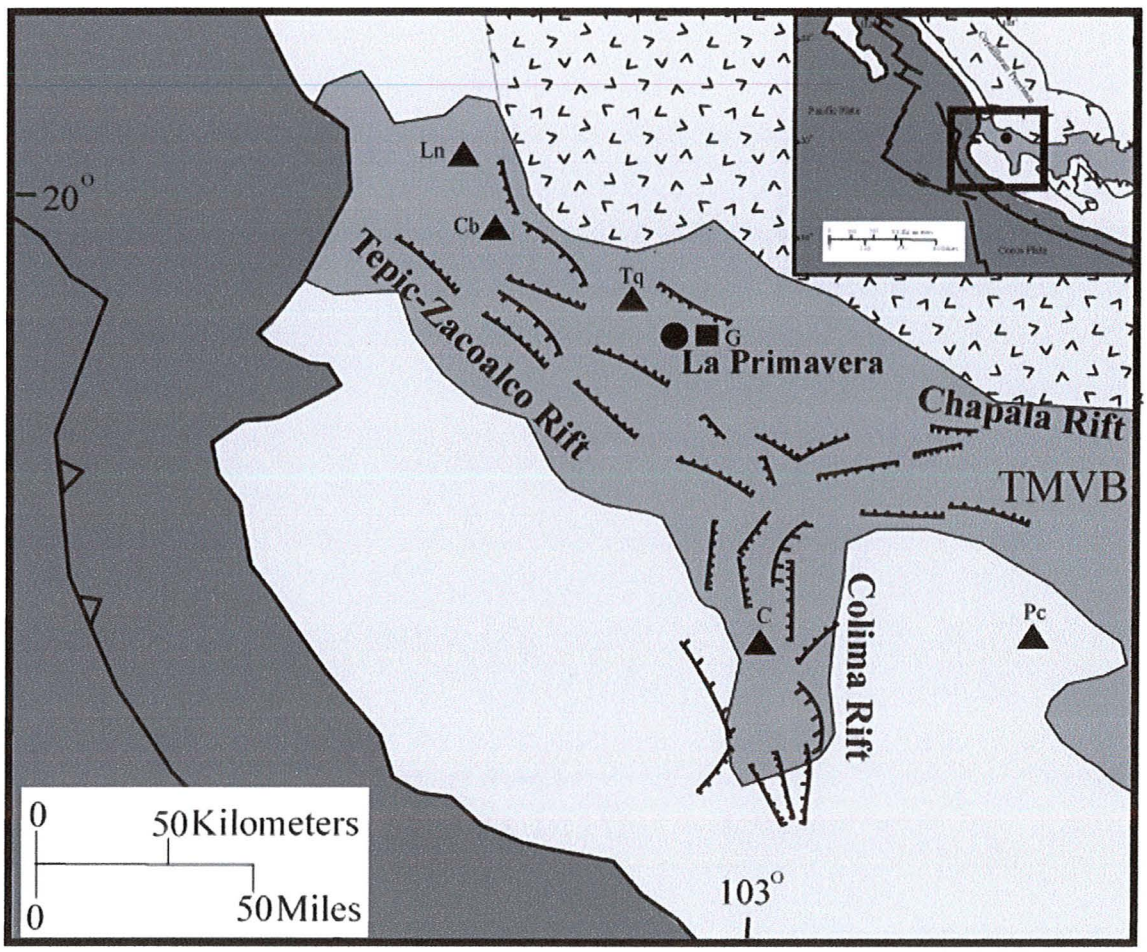

Figure 2 Map of western Mexico showing the major volcanic centers and rift zones. La Primavera is shown as solid circle. The city of Guadalajara is shown as a solid square. Volcanoes shown as triangles are Ln:Las Navajas; Cb:Ceboruco; Tq:Tequila; C:Colima; Pc, Paricutin. Figure after Nelson and Hegre (1990).

Table 1 Summary of the geologic history of La Primavera (Mahood, 1980)

Event	Age	Dating method	Material Dated
Pre-caldera lavas	120 -100 ka	K-Ar	Sanidine, glass, and whole rock glass
Eruption of Tala Tuff	95 ka	K-Ar	Sanidine
Caldera Collapse	95 ka	Determined from field relation observations	-
Eruption of central domes	96 ka	K-Ar	Sanidine and glass
Eruption of giant pumice horizon	95 ka	K-Ar	Sanidine
Eruption of older ring domes	95 ka	K-Ar	Sanidine and glass
Eruption of younger ring domes	75 ka	K-Ar	Sanidine, glass, and whole rock glass
Uplift	75 ka	Determined from field relation observations	-
Eruption of southern arc lavas	60 -20 ka	K-Ar	Whole rock glass

Chapter III

^{238}U-^{230}Th Disequilibrium Dating of Accessory Minerals

Uranium-series nuclides have a wide set of geochronologic applications because of a diverse and long decay chain where the radiogenic daughters are themselves radiogenic (Dickin, 2005). Uranium decays to stable Pb via two separate chains (Figure 3). In the first chain, parental ^{238}U decays to stable daughter ^{206}Pb via eight α-decays of short-lived intermediate daughter isotopes. In the second chain, ^{235}U decays to its stable daughter ^{207}Pb via seven α-decays of short-lived intermediate daughter isotopes. This decay chain implies that in a uranium-bearing system that has remained undisturbed for a few million years, a state of 'secular equilibrium' is reached. The decay chain is in a state of secular equilibrium state when the activity of each intermediate daughter nuclide in the chain is equal to that of the parent. The activity of a radioactive nuclide (with units of decays per second or Becquerels) is equal to the number of atoms (N) multiplied by its decay constant (λ). By convention, activity of a nuclide is denoted by parentheses. A decay chain is in secular equilibrium when the activity of the parent and intermediate daughters are equal:

$$(1) \quad (\text{Activity}) = \lambda_o N_o = \lambda_1 N_1 = \lambda_2 N_2 = \lambda_n N_n$$

in which λ_o and N_o are the decay constant and number of atoms of the original parent, and λ_1 and N_1 are the decay constant and abundance of the first daughter and so on. Non-equal activities between parent and intermediate daughters in this decay chain is the basis of ^{238}U-^{234}U-^{230}Th disequilibrium geochronology.

Differential partitioning of parent and intermediate daughters during crystallization of minerals with U/Th $\neq 1$ results in disequilibrium between the activities

of U and Th nuclides in the U-Pb decay chain. For example, U is preferentially partitioned into zircon relative to Th (Blundy and Wood, 2003), which leads to an initial condition where (^{234}U)/(^{230}Th) is >1. Accessory minerals typically have high U/Th (e.g., zircon, baddelyite) or low U/Th (e.g., chevkinite, allanite, monazite) so there is a relatively high degree of (^{238}U)/(^{230}Th) disequilibrium during crystallization (e.g., Fukuoka, 1974; Gill and Condomines, 1982; Reid *et al.*, 1997; Blundy and Wood, 2003; Vazquez and Reid, 2004; Schmitt, 2009). If initial parent-daughter relations are known or assumed, the magnitude of disequilibrium between parent and daughter isotopes in the U decay chain can be used to quantify the elapsed time between the event that generated radioactive disequilibrium at t = 0 and a later time t (e.g., today). The magnitude of radioactive disequilibrium between daughter (index 2) and parent nuclides (index 1) is related to time (t) by:

$$(2) \qquad N_2\lambda_2 = N_1\lambda_1\left(\frac{\lambda_2}{\lambda_2-\lambda_1}\right)\left(1-e^{-(\lambda_2-\lambda_1)t}\right) + N_2^0\lambda_2 e^{-\lambda_2 t}$$

Where N^0 is the number of atoms present at t = 0. Time can be solved for in equation (2) assuming a closed system since the attainment of disequilibrium. In a closed system, isotopic abundances reflect radioactive decay and ingrowth. Since the decay constant of the short lived parent (λ_2) is much greater than the decay constant (λ_1) of the long lived parent such that $\lambda_2 >> \lambda_1$, then equation (2) simplifies to:

$$(3) \qquad N_2\lambda_2 = N_1\lambda_1\left(1-e^{-\lambda_2 t}\right) + N_2^0\lambda_2 e^{-\lambda_2 t}.$$

In the ^{238}U-^{234}U-^{230}Th system, the long lived parent (N_1) is ^{234}U and the short lived daughter (N_2) is ^{230}Th. Uranium-238 activity is typically used as proxy for ^{234}U activity (i.e., (^{238}U) = (^{234}U)) because high mass isotopes are essentially not fractionated from each other during crystallization of magmas. Accordingly, equation (3) can be written:

$$(4) \quad (^{230}\text{Th}) = (^{238}\text{U}) \times (1 - e^{-\lambda_{230}t}) + (^{230}\text{Th})e^{-\lambda_{230}t}$$

Since this equation has the form of a straight line (y = mx + b), minerals that crystallize at the same time but with different ^{238}U contents will form a linear array (isochron) whose slope is proportional to age. For normalization, equation (4) is divided by ^{232}Th (half life = 14 Ga), which is effectively stable over the short timescales associated with radioactive disequilibrium between ^{234}U and ^{230}Th (Condomines, 1982). Accordingly, equation (4) is:

$$(5) \quad \frac{(^{230}\text{Th})}{(^{232}\text{Th})} = \frac{(^{238}\text{U})}{(^{232}\text{Th})} \times (1 - e^{-\lambda_{230}t}) + \frac{(^{230}\text{Th})}{(^{232}\text{Th})} e^{-\lambda_{230}t}.$$

Equation (5) plots as a straight line in the (^{230}Th)(^{232}Th) vs. (^{238}U)(^{232}Th) isochron diagram. Samples in secular equilibrium have equal (^{230}Th)/(^{232}Th) and (^{238}U)/(^{232}Th) activity ratios and lie on a line with a slope of unity (called the equiline) (Dickin, 2005). The age of the system is calculated from the slope m of the isochron and λ_{230} in the equation:

$$t = -\frac{\ln (1 - m)}{\lambda_{230}}$$

As time passes after crystallization and excess ^{238}U or ^{230}Th decays, the isochron rotates about its point of intersection with the equiline (Figure 4). This point of intersection remains constant if the system remains closed and represents the initial value of ^{230}Th/^{232}Th for the components defining the isochron. Due to the short half life of ^{230}Th ($t_{1/2}$ = 75 ka) and relatively long half lives of ^{238}U and ^{232}Th, the (^{230}Th)/(^{232}Th) ratio increase or decreases depending on initial sense of disequilibrium whereas the (^{238}U)/(^{232}Th) remains essentially constant. Accordingly, individual data will move up or down towards the equiline as time progresses (Figure 4). An isochron with a slope of

zero indicates that the system is at the time of crystallization (t_0). After approximately 5 half lives for ^{230}Th (~350 ka), ^{238}U and ^{230}Th approach secular equilibrium so the isochronous data (with their associated uncertainties) will reach a slope of unity and will effectively overlap the equiline. Accordingly, systems that are older than ~350 ka are beyond the limits of ^{238}U-^{230}Th dating and rocks/minerals in secular equilibrium (that were initially in disequilibrium) are older than approximately 350 ka (Dickin, 2005).

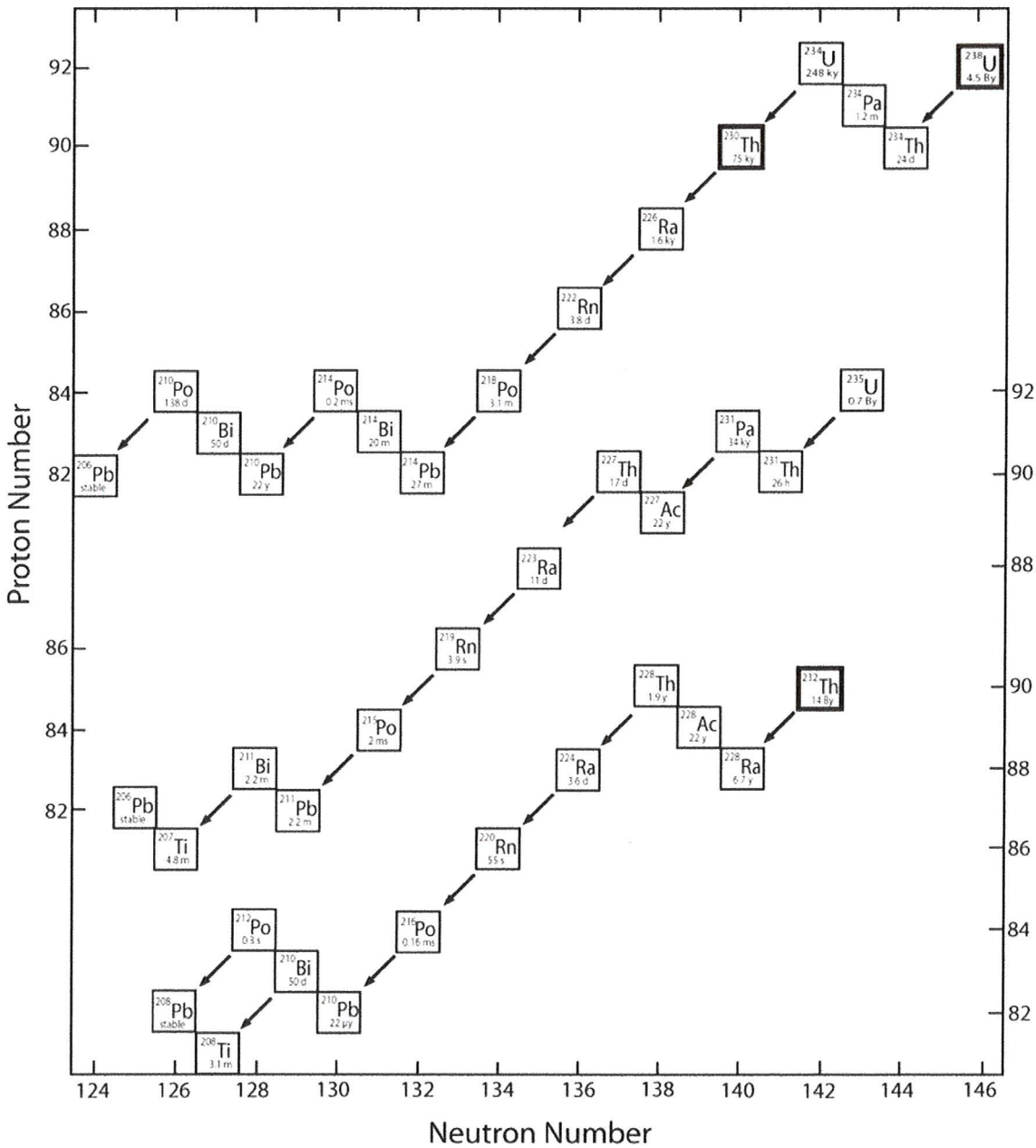

Figure 3 Parents and daughter nuclides in the ^{238}U-^{235}U-^{232}Th decay chains and their half-lives. After Dickin (2005).

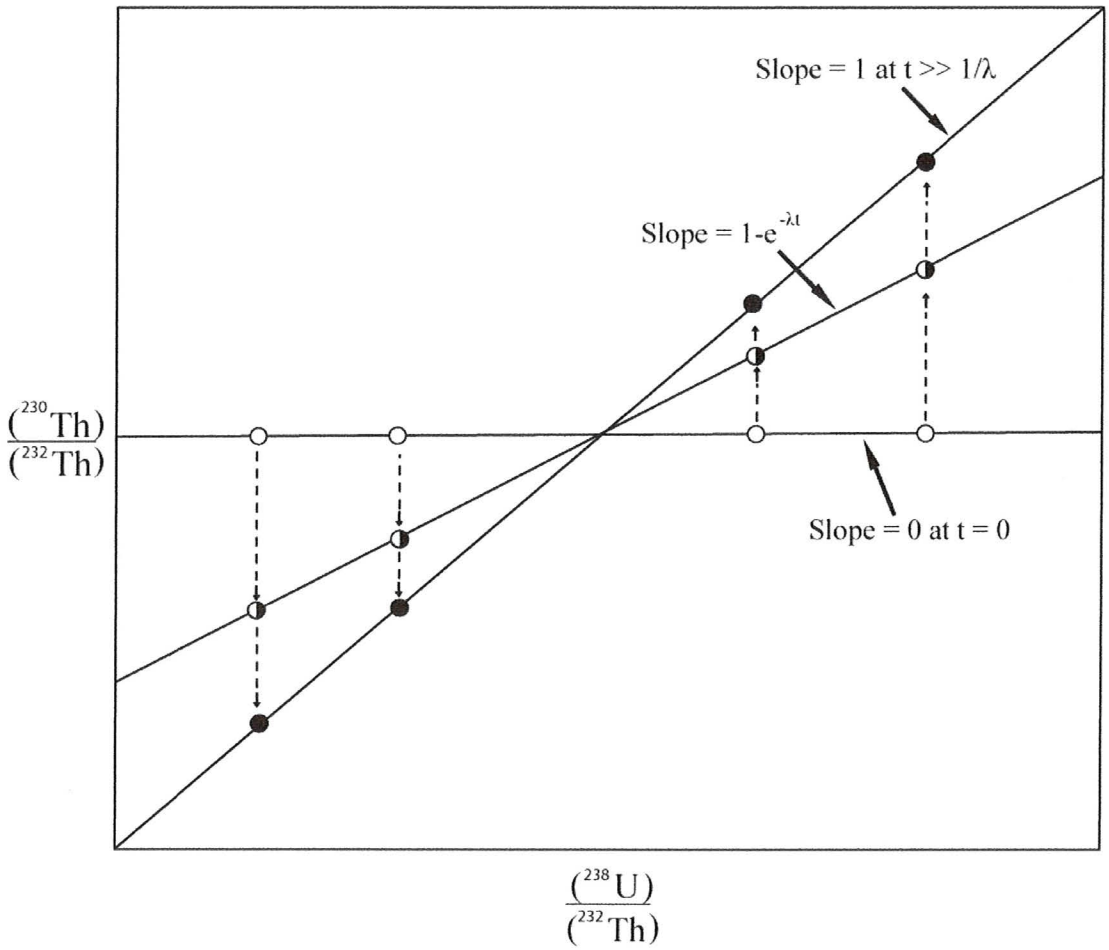

Figure 4 Isotopic evolution of isochronous rocks or minerals on the (^{230}Th)/(^{232}Th) versus (^{238}U)/(^{232}Th) isochron diagram. Symbols: Open circles represent samples at initial time t=0; half-filled circle is t>0; Solid circles denotes samples after ~ 350 ka, at this time samples are in statistical secular equilibrium ($t >> 1/\lambda$). Minerals such as chevkinite, allanite, titanite, and monazite with low U/Th ratios plot to the left of the point of intersection (equipoint) between the t=0 line and equiline (slope =1). Minerals such as zircon with high U/Th ratios typically plot right of the equipoint. After Dickin (2005).

Chapter IV

Chevkinite-(Ce) in Silicic Magmas

Accessory minerals such as chevkinite, zircon, allanite, monazite, titanite, and xenotime are important because they are hosts for large fractions of trace elements in intermediate and felsic magmas (Miller and Mittelfehldt, 1982; Hanson, 1980; Bacon, 1989). Fractionation of accessory phases results in depletion of otherwise incompatible elements in evolved silicic magmas and explains rare earth element (REE) patterns and incompatible elements ratios in high silica rhyolites; most notably, Th/U fractionation in high-silica rhyolites (Bacon, 1989). In similar manner, allanite and chevkinite have a strong preference for light rare earth elements (LREE) and may greatly influence the REE budget of silicic magmas by reducing the relative concentration of otherwise incompatible REE (such as La, Ce, and Nd), Nb, Zr, and Y in residual melts (Troll *et al.*, 2003; Gromet and Silver, 1983). Hence, understanding chevkinite is important for evaluating petrologic questions using trace element modeling, such as the role of fractional crystallization in magma evolution and the role of restitic accessory phases in anatexis (Macdonald and Belkin, 2002).

Igneous chevkinite occurs in a range of silicic magma compositions. In volcanic rocks, chevkinite typically occurs in evolved peralkaline magmas such as trachyte, comendite, and pantellerite (e.g., Young and Powers, 1960; Schmitt *et al.*, 2000; Scaillet and Macdonald, 2001; Macdonald *et al.*, 2002; Heumann and Davies, 2002; Troll *et al.*, 2003; Johnson *et al.*, 1989) as well as some evolved "A-type" metaluminous rhyolites (e.g. Izett and Wilcox, 1968; Schmitt *et al.*, 2000; Macdonald and Belkin, 2002; Johnson *et al.*, 1989). An extensive review of chevkinite paragenesis is given by Macdonald *et al.*

(2002, 2009).

Chevkinite crystallizes over a wide range of pressures and temperatures and it may have a variable chemical composition depending on its occurrence and paragenesis. Chevkinite from Little Chief granite is estimated to have crystallized in the 700-750°C range at a pressure near 1.5 kbar (McDowell, 1979). Rhyolites from the Greater Olkaria Volcanic Complex in the Naivasha area of the Kenyan Rift Valley are calculated to have crystallized chevkinite at ~675°C in ~1.5 kbar in 4 weight % H_2O conditions (Scaillet and Macdonald, 2001).

The chemical formula and charge-balance relationship of chevkinite varies depending on occurrence (Kauffman and Jaffe, 1946; Ito, 1967; Green and Pearson, 1988; McDowell, 1979; Calvo and Faggiani, 1974; Macdonald *et al.*, 2002; Macdonald and Belkin, 2002) but follows the general formula:

$$A_4BC_2D_2Si_4O_{22}$$

Where A=REE, Ca, Sr, Na, K, Th; B=Fe^{2+}, Mg, Mn, Ca; C=Ti, Mg, Mn, Fe^{3+}, Fe^{2+}, Al, and D=Ti; the most common REE in chevkinite are La, Ce, Pr, Nd, Pm, and Sm. In chevkinite, the general charge-balanced relationship applies:

$$(Ca+Sr)_A + Ti_C = REE_A + M_C^{3+,2+}$$

Where REE= rare earth elements, A=A site, C=C site, M_C= Fe, Al, Mg, Zr, Nb, P, and K (McDowell, 1979; Macdonald and Belkin, 2002). The A site contains LREE concentration that is derived from a surrounding volume of melt about 1000 times larger than its own volume. Moreover, chevkinite may extract these elements at a fairly constant rate over magmatic time scales, as evidence by the absence of textual and compositional zoning in some chevkinite crystals (Troll *et al.*, 2003; Macdonald and

Belkin, 2002). Nevertheless, zoned chevkinites occur in some volcanic rocks (Macdonald and Belkin, 2002) such as the rhyolitic tuffs from Yellowstone (Figure 5).

Chevkinite in La Primavera Rhyolites

Chevkinite in La Primavera rhyolites makes up <1% of the modal crystal population (Michael, 1988; This study). La Primavera chevkinite is generally <30 μm in size with a few crystals as large as 100 μm (Figure 6). Chevkinite from La Primavera is distinguished by its brownish-black to reddish-brown color and vitreous luster. La Primavera chevkinite generally occurs as inclusions (<60 μm in size) within zircon grains, groundmass glass, ferrohendenbergite and fayalite phenocrysts, or occasionally occurs as microphenocrysts (Figure 6)(Michael, 1988; this study).

In La Primavera rhyolites, chevkinite inclusions are rich in LREE. Typical values for LREE in igneous chevkinite (including those for La Primavera) are: La_2O_3=10-13 wt%, Ce_2O_3=19-22wt%, Pr_2O_3=1-2Wt%, Nd_2O_3=6-7wt%, Sm_2O_3=<1wt% (Table 1). In general, Th concentrations in chevkinites from silicic magmas range between 0.3 to 5.0 weight % with a mean of 1.4 wt.% (Table 2). LREE concentrations in La Primavera chevkinite are comparable to examples from different localities (Table 3). Relative to chevkinites from Canary Island trachytes and rhyolites (Troll et al., 2003), synthetic chevkinite from experiments using silicic melts (Green and Pearson, 1988), and chevkinite in syenite pegmatites in Olso Region, Norway (Salgastad and Larsen, 1978), chevkinites from La Primavera rhyolites (Michael, 1988) contain lower concentrations of LREE and lower concentrations of Th. Relative to chevkinites from East African peralkaline rhyolites (Macdonald *et al.*, 2002), Little Chief granite California (McDowell,

1979), syenitic intrusion complex from China (Jiang, 2006), and Lava Creek Tuff in Yellowstone (Macdonald and Belkin, 2002), La Primavera chevkinites contain slightly higher concentrations of LREE and comparative concentrations of Th. For more chemical analysis of chevkinite from different localities, see Macdonald and Belkin (2002) and the works of the aforementioned authors.

Arondu Chevkinite

This study utilizes natural igneous chevkinite from Arondu, Basha Valley, Baltistan, Pakistan, as a secular equilibrium standard. The standard material is taken from a single large crystal, ~4 cm in length and ~2 cm in width, which was acquired from a commercial mineral dealer (Figure 7**)**. Arondu chevkinite is non-metamict and occurs in a "high-temperature pneumatolitic vein" (Liziero, 2008) in the uplifted Himalayas; This suggests that it is pre-Quaternary in age and is in ^{238}U-^{230}Th secular equilibrium. Also, a thin selvage of green tourmaline covers the chevkinite crystal. Backscatter electron images and energy dispersive x-ray analysis reveals that the Arondu chevkinite is compositionally zoned, with significant zoning in Ca concentrations (Figure 8, Table 4). Although electron microprobe data of the specific Arondu chevkinite crystal used in this study was not performed, a database of electron microprobe analysis for Arondu chevkinite is available and published by the RRUFF^{TM} project (Downs, 2006) and in the dissertation of Liziero (2008).

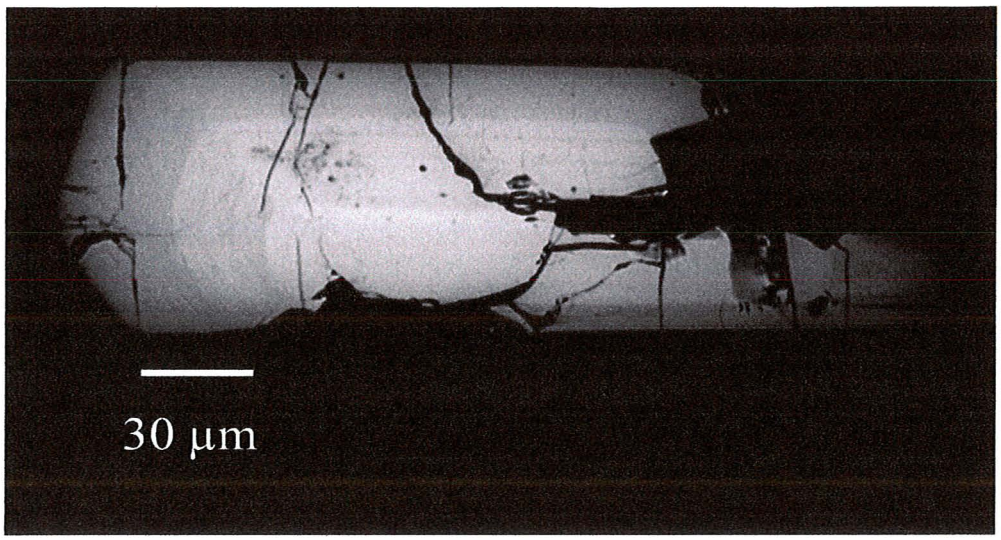

Figure 5 BSE image of chevkinite from Mesa Falls Tuff, Yellowstone Plateau, showing compositional (including REE) zoning (image provided by J. Vazquez).

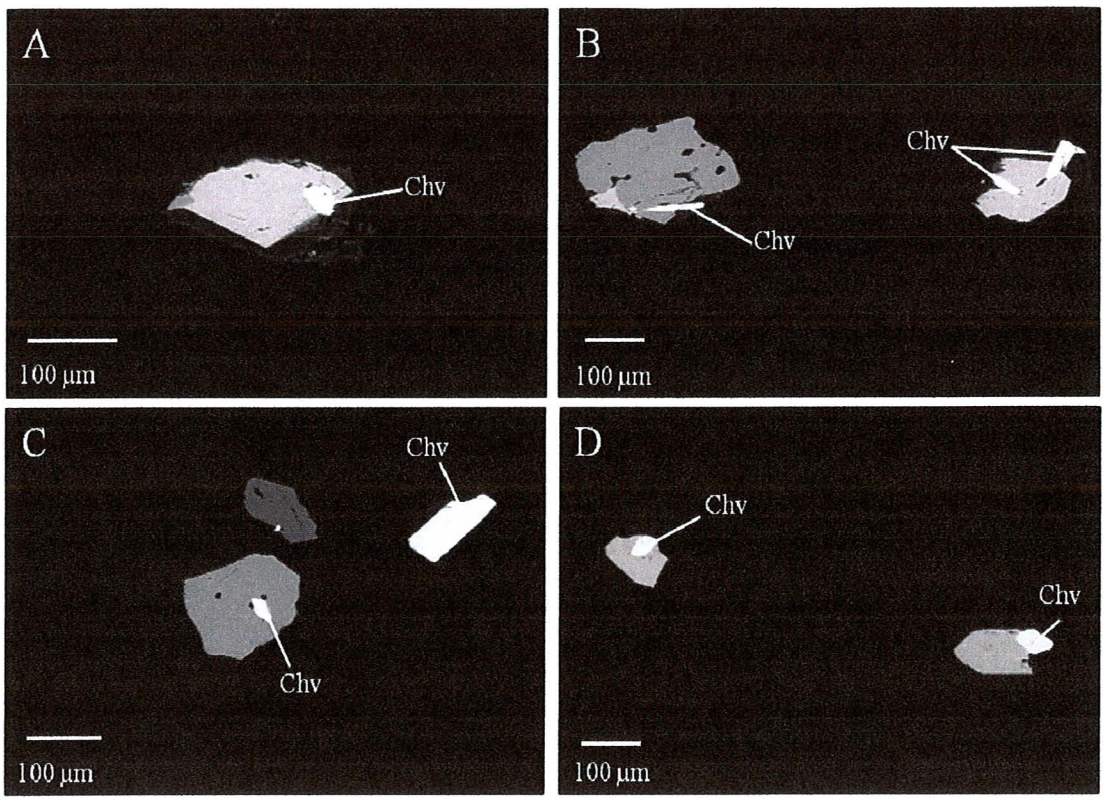

Figure 6 BSE images of chevkinite (Chv) as inclusions, intergrowths, or individual grains held in place by epoxy mount (black). A) Image of a chevkinite inclusion in fayalite. B) Chevkinite inclusion in fayalite (right) and microcryst in glass (left). C) Chevkinite crystal in glass (left) and chevkinite phenocryst (right). D) Chevkinite inclusion in fayalite (left) and chevkinite inter-grown with fayalite (right).

Figure 7 Chevkinite from Arondu, Pakistan, used as a ^{238}U-^{230}Th secular equilibrium standard.

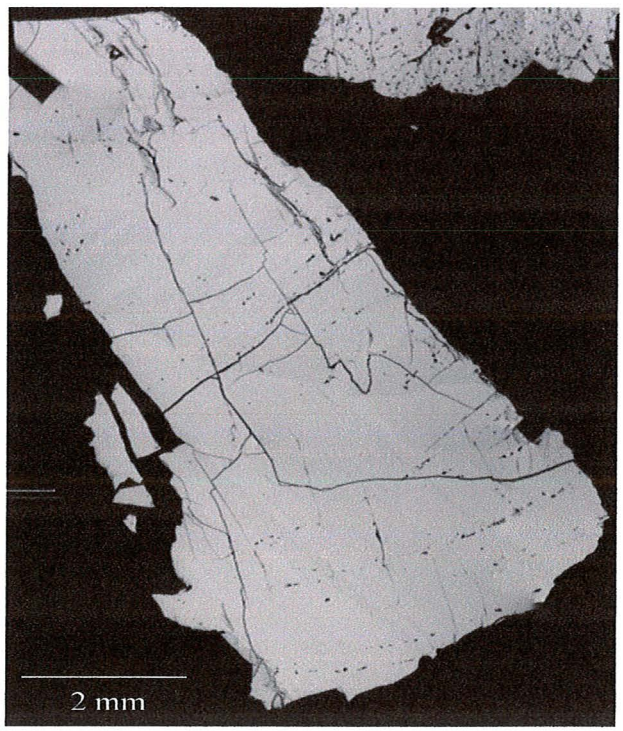

Figure 8 BSE image of Arondu chevkinite (grain one). Faint zoning represents compositional heterogeneity.

Table 2 Electron microprobe analysis of chevkinite included in La Primavera pyroxenes. Data from Michael (1988).

	Sample 514 Older ring dome (~95 ka) 20° 43' 40"N, 103° 35' 00"W	Sample 992-151 Younger ring dome (~75 ka) 20° 38'N, 103° 30W
SiO_2	19.4	20.6
TiO_2	19.2	17.7
Al_2O_3	1.01	0.26
FeO	10.1	11.6
CaO	2.36	3.20
P_2O_5	0.05	0.09
La_2O_3	13.0	12.0
Ce_2O_3	21.3	21.4
Pr_2O_3	1.96	1.94
Nd_2O_3	6.65	7.51
Sm_2O_3	0.90	0.88
Y_2O_3	0.60	0.47
ThO_2	0.60	0.67
Total	97.13	98.32

Table 3 Chemical composition (weight %) of chevkinite from select localities. The chemical composition of Arondu chevkinite is the average of 15 analyses done on a single grain.

	Arondu (Downs, 2006) Sample: R060282	La Primavera (Michael, 1988) Sample: 514	Little Chief California (Douglas, 1979) Samples: 63-1 & 63-2 (average of two samples)	Lava Creek Tuff Yellowstone (MacDonald and Belkin, 2002) Sample: 50-61A (H)
SiO_2	18.23	19.4	19.74	20.48
Al_2O_3	0.11	1.01	2.05	0.65
La_2O_3	9.47	13.0	15.12	11.99
Ce_2O_3	24.67	21.3	18.24	20.61
CaO	1.75	2.36	4.27	3.40
TiO_2	17.17	19.2	17.16	17.16
MgO	0.35	-	0.52	0.15
FeO	10.89	10.1	9.34	11.70
Nb_2O_5	0.52	-	0.23	1.23
ThO_2	0.93	0.60	0.97	1.35
Nd_2O_3	9.36	6.65	4.32	6.92
MnO	-	-	0.93	0.11
Pr_2O_3	-	-	0.88	1.97
Sm_2O_3	-	-	0.60	-
Y_2O_3	-	-	0.11	0.89
Total	93.46	97.13	96.32	99.86

Table 4 Average of standardless (normalized to 100%) energy dispersive x-ray analysis of Arondu chevkinite. Averages represent 52 spots on "grain one."

Element	Weight %	Standard Deviation
Mg	0.22	0.14
Al	0.14	0.11
Si	9.76	0.35
Ca	1.6	0.21
Ti	10.28	0.41
Mn	0.49	0.2
Fe	8.99	0.37
Nb	0.18	0.25
La	9.86	0.74
Ce	20.72	0.65
Pr	1.64	0.7
Nd	6.28	0.57
Sm	0.27	0.43
Th	1.53	0.4
O	28.42	0.43

Chapter V

Sample Preparation and SIMS ^{238}U-^{230}Th Analysis of Chevkinite and Zircon

Sample Preparation

Fresh (glassy) samples of La Primavera rhyolites were obtained from outcrops using the geologic map from Mahood (1980) and brought to the lab for processing. The hammer-crushed rock samples were ground in a steel urn and sieved to a size between 250-40 μm. Heavy minerals (ρ>2.9 g/cm^3) were separated from crushed samples using sodium polytungstate. These heavy minerals were then collected and placed in a petri dish where individual chevkinite and zircon grains were handpicked using a stereoscopic microscope. The samples were then prepared for SIMS (secondary ion mass spectrometry) analysis. SIMS analysis requires samples to be solid, ultra high vacuum proof, and flat. To achieve these SIMS instrument analysis pre-requisites, chevkinite and zircon grains were embedded in a 2.54 cm diameter mount made of epoxy resin. In some instances, analysis of small grains embedded in epoxy mounts proved to be problematic because of beam overlap with the surrounding epoxy. During analysis of zircon and chevkinite, a doubly charged Th-O-C ($^{232}Th_2{}^{12}C^{16}O^{2+}$) molecule is generated and interferes at mass 246 when the epoxy is partly sputtered by the primary beam (Schmitt *et al.*, 2006; Schmitt, 2009). In general, all sources of carbon are detrimental to $^{230}ThO^+$ analysis as the Th-O-C interference is unresolved even at extremely high mass resolution (Schmitt, 2009). To avoid this interference derived from epoxy-beam overlap, a mount with indium metal was used to analyze small (comparable to SIMS instrument spatial resolution) chevkinite grains. The soft indium allows embedment of euhedral crystals into the mount by simply pushing the grains into the mount; crystal faces are flush with

the mount surface and no further grinding (but minimal polishing) is required (Figure 9). Prior to analysis, samples were washed in an ultrasonic bath with soapy water and a final cleaning with 1 N HCl to remove surface contaminants. Finally, the mounts were coated with a thin (~10 nm) layer of gold to create a conducting surface on the mount.

Analysis with CAMECA IMS-1270 Ion Microprobe

In the past decade, secondary ion mass spectrometry (SIMS) has been applied to ^{238}U-^{230}Th dating of various igneous minerals (e.g. Reid, *et al.* 1997; Bacon *et al.*, 2000; Lowenstern *et al.*, 2000; Charlier *et al.*, 2003; Vazquez and Reid, 2004; Schmitt and Vazquez, 2006; Schmitt, 2009). The advantage of SIMS analysis is that it allows *in situ* measurements of intracrystal isotopic composition. SIMS analysis is based on the observation that (secondary) ions are ejected from a sample surface when bombarded by a primary beam of ions (Figure 10). SIMS analysis is typically performed using ion microprobes with large radius magnets for high mass resolution analysis of isotopic composition. Most commonly used ion microprobes (e.g., SHRIMP or CAMECA IMS series) consist of a primary beam source that supplies a bombarding species of positively or negatively charged ions, a sample chamber containing a target sample, a secondary ion collector, an electrostatic analyzer that discriminates based on ion energy, a mass analyzer that isolates the ion of interest, and an ion detection system that records the intensity of the secondary ion signal.

Chevkinite and zircon analyses were performed with the CAMECA IMS 1270 high resolution ion microprobe at the University of California, Los Angeles (Figure 11, Figure 12). For sputtering, a primary beam of mass filtered $^{16}O^-$ at ~20-50 nA intensity

was focused into a ~40 μm spot on sample surfaces; primary beam impact energies were ~22.5 kV and secondary ions were extracted at 10 kV. Samples were pre-sputtered for 10 seconds at the start of each measurement. Measurements of chevkinite and zircon were made with a mass resolving power (m/Δm) of ~4400 at 10% peak width, while potential isobaric interferences in chevkinite were resolved using a mass scan with a mass resolving power (m/Δm) of ~6000 (Figure 13).

The oxides $^{230}Th^{16}O^{+}$ and $^{238}U^{16}O^{+}$ were measured instead of their corresponding metal species (i.e., ^{230}Th, ^{238}U) because yields for these oxides are up to 10 times more abundant than their metals (Schmitt, 2006, 2009). For chevkinite analyses, detection of $^{230}Th^{16}O^{+}$,$^{238}U^{16}O^{+}$ and other masses was performed in single collector mode using an electron multiplier detector (Figure 14). For chevkinite, $^{230}Th^{16}O^{+}$ intensities were <1 count per second (cps) and $^{232}Th^{16}O^{+}$ intensities were approximately 10^{4}-10^{5} cps. Average background counting rates during the analysis of chevkinite were 0.07± 0.1 cps (as measured for mass 246.3). For zircon analyses, detection of $^{230}Th^{16}O^{+}$, $^{238}U^{16}O^{+}$, $^{232}Th\ ^{16}O^{+}$ and other masses was performed in multicollector mode using a combination of electron multiplier and Faraday cup (Figure 15) detectors. For zircon, $^{230}Th^{16}O^{+}$ intensities were ~10 cps and $^{238}U^{16}O^{+}$ intensities were approximately 10^{4}-10^{5} cps. Average background counting rates during the analysis of zircon were 0.04± 0.08 cps (as measured for mass 246.3). Detectors used for each session of chevkinite and zircon analyses are described in Appendix 2.

Relative Sensitivity Factor

Thorium and uranium (and their oxides) have different ionization yields during

sputtering of zircon and allanite (Reid *et al.*, 1997; Vazquez and Reid, 2004; Schmitt, 2009), such that a correction factor must be applied to measured $^{230}Th^{16}O^{+}$ /$^{238}U^{16}O^{+}$ or $^{238}U^{16}O^{+}$/$^{232}Th^{16}O^{+}$ ratios (Reid *et al.*, 1997). To account for this bias, a relative sensitivity factor (RSF) is determined from an ancient (>350 ka) standard that has (^{230}Th)/(^{238}U) = 1 (Reid *et al.*, 1997). Ancient zircons or chevkinites that are non-metamict should be in secular equilibrium (i.e., (^{230}Th)/(^{238}U) = 1). In high U/Th minerals such as zircon and baddeleyite, U is preferentially ionized over Th (Ireland, 1995; Reid *et al.*, 1997; Schmitt, 2009). In low U/Th minerals such as allanite (Vazquez and Reid, 2004) and chevkinite (this study), Th is preferentially ionized over U. For this study, the U/Th RSF for chevkinite and zircon was determined from measurements of (^{238}U)/(^{230}Th) of Arondu chevkinite (this study) and AS3 zircon (Paces and Miller, 1993; Schmitt, 2009) respectively. The RSF is obtained from the measured (^{238}U)/(^{230}Th) relative to the secular equilibrium value of (^{238}U)/(^{230}Th) = 1. RSF corrections on standard materials strongly depend on analytical conditions (e.g. primary bean species, sample charging, energy window analyzed) during SIMS analysis (Schmitt, 2009). Hence, appropriate RSF factors need to be determined on individual analysis sessions. The relative sensitivity factor for correction of measured Th/U obtained from Arondu chevkinite and AS3 zircon during individual analytical sessions are summarized in Table 5 and figures 17-21.

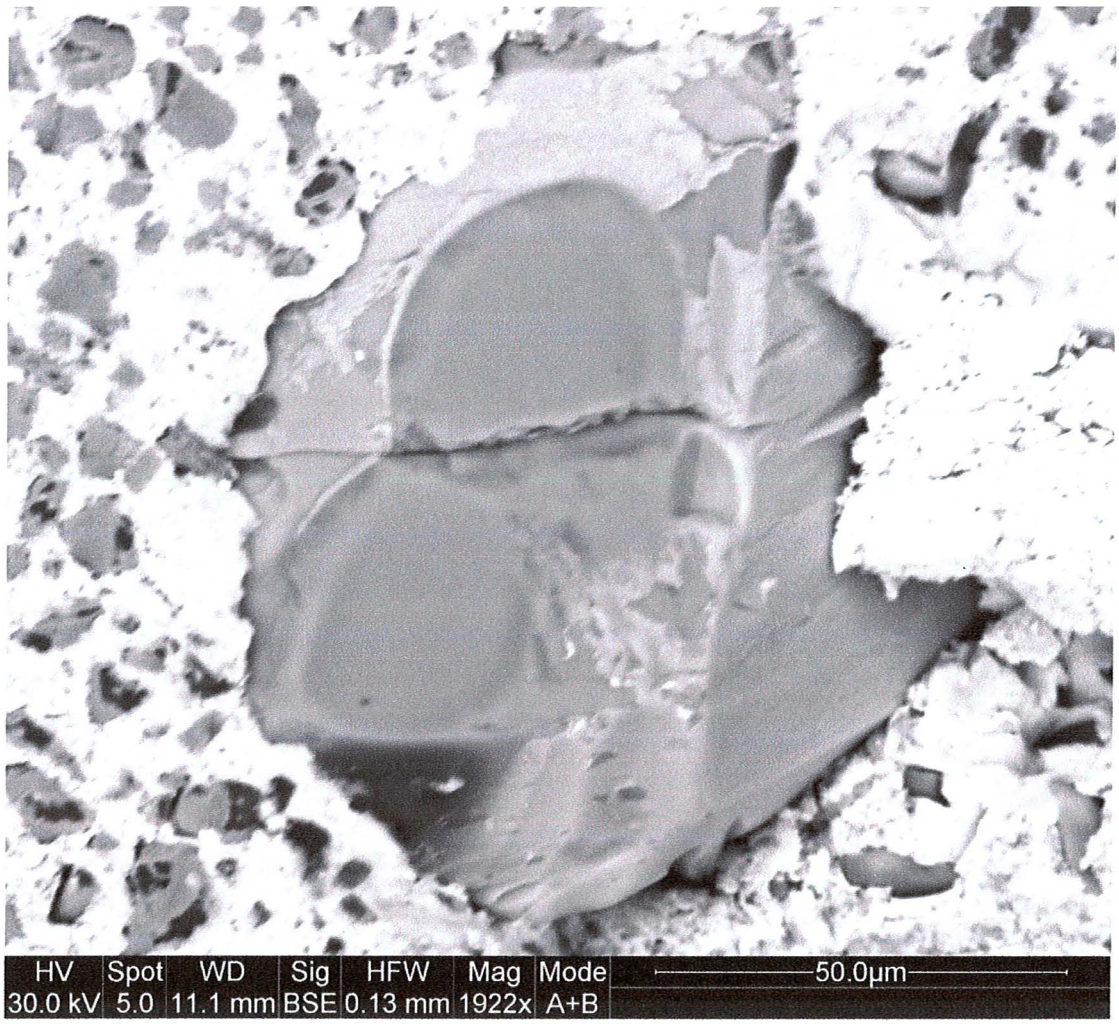

Figure 9 Image of chevkinite in indium mount.

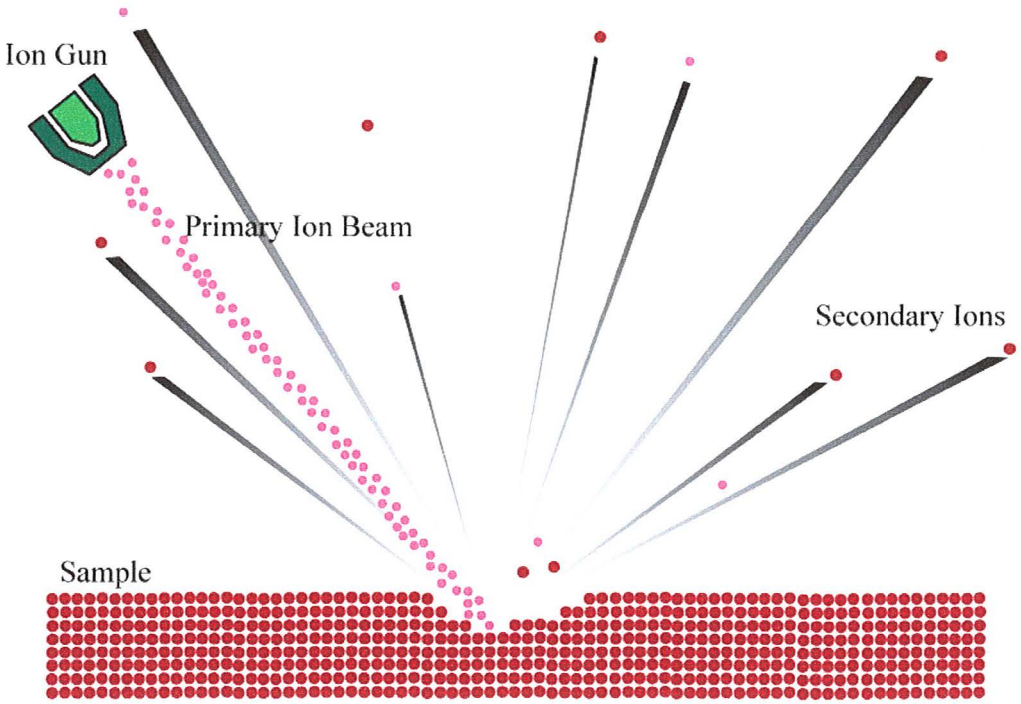

Figure 10. Schematic view of secondary ions showing principle of SIMS analysis. Secondary ions are ejected from a sample surface when bombarded by a primary beam of ions.

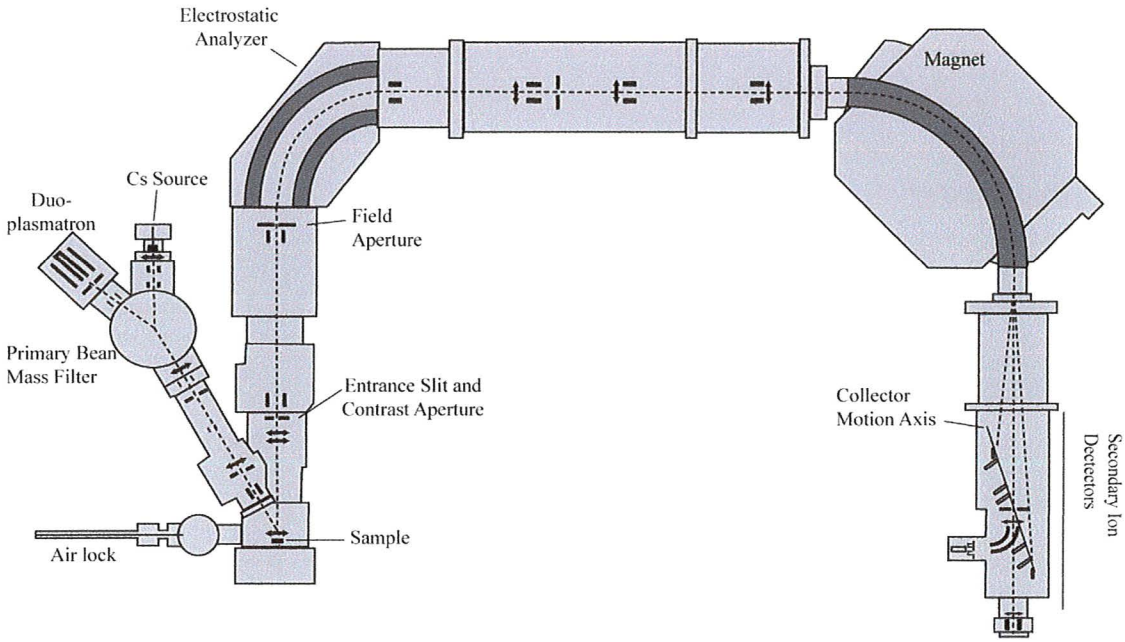

Figure 11 Schematic view of CAMECA IMS-1270. CAMECA IMS-1270 consist of a primary beam source that supplies a bombarding species of positively or negatively charged ions, a sample chamber containing a target sample, a secondary ion collector, an electrostatic analyzer that discriminates based on ion energy, a mass analyzer (magnet) that isolates the ion of interest, and an ion detection system (Figure 13) that records the intensity of the secondary ion signal.

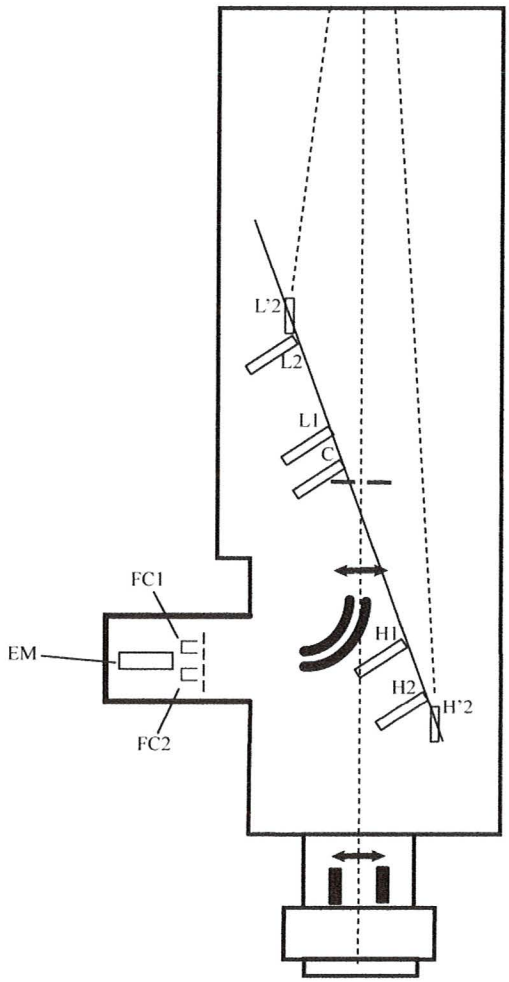

Figure 12 Schematic view of secondary ion multicollector array. The CAMECA IMS 1270 consists of 10 ion detectors: 2 Faraday Cups (FC1 and FC2), 1 Electron multiplier (EM) (used for mono collection system) and 4 Faraday Cups (L'2, L2, L1, C) and 3 Electron multipliers (H1, H2, H'2).

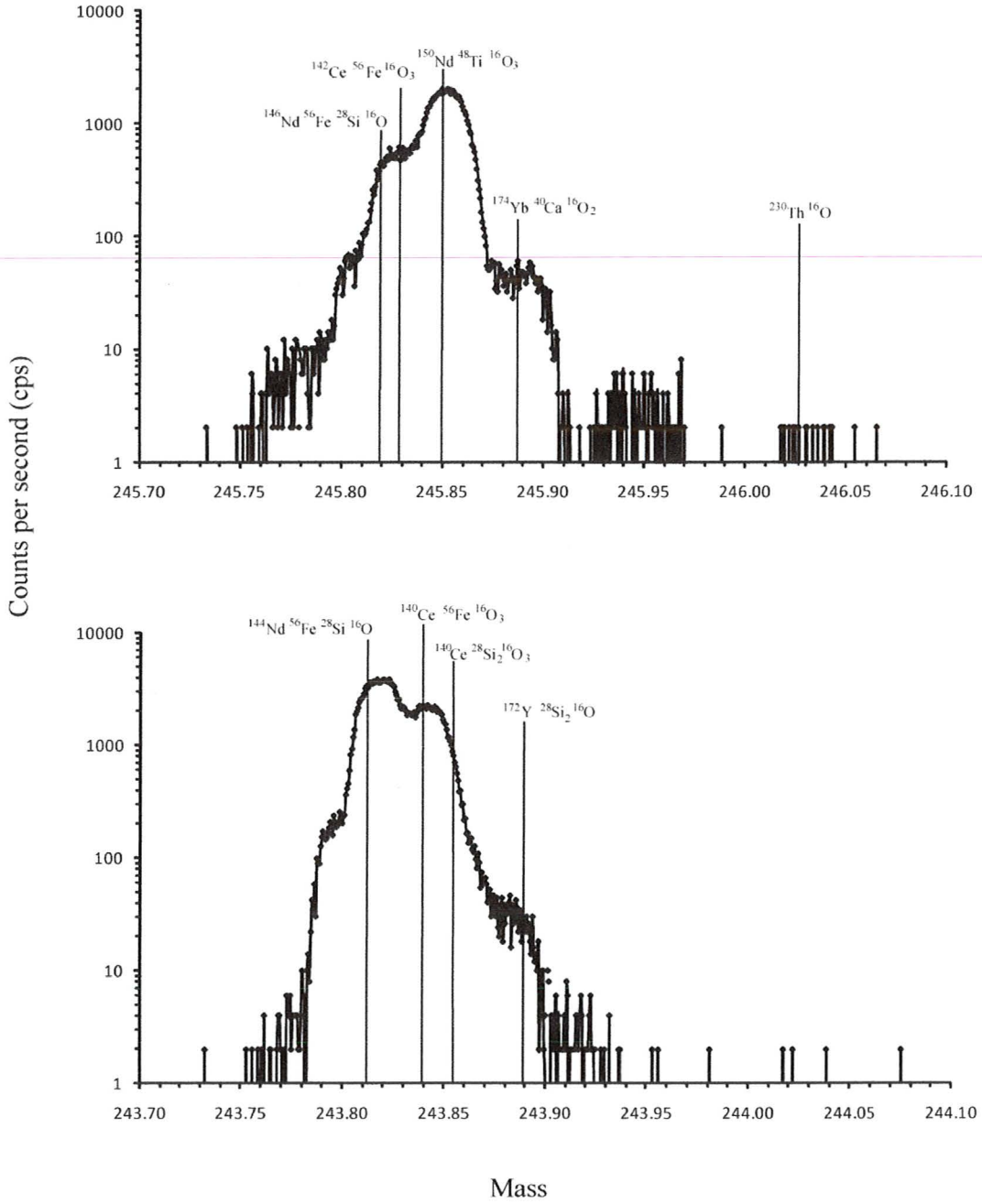

Figure 13 Mass scans of potential isobaric interferences in chevkinite at mass resolving power (m/Δm) of 6000 at 10% peak height. Background is measured at 244.038.

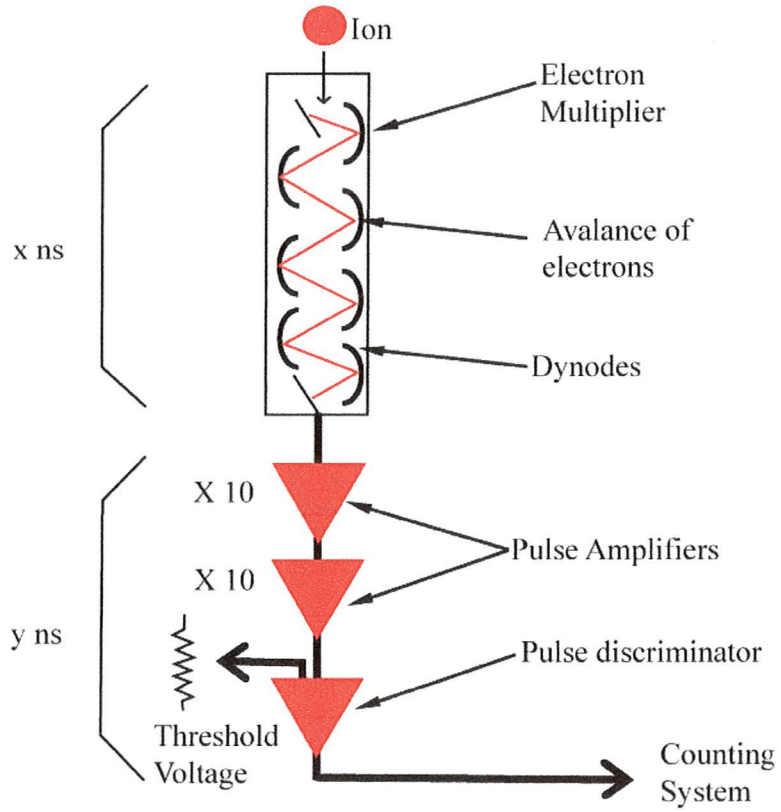

Dead time = x + y ns

Figure 14 Schematic view of an electron multiplier. An electron multiplier is the most sensitive detector (count rate less than 0.01 cps). It consists of a series of electrodes called dynodes connected to a resistor chain. A particle strikes the first dynode and then produces a few secondary electrons which are then accelerated to the second dynode and so on. The pulse coming out of the dynodes is then amplified and passed to the counting circuit. The time taken for the multiplier, amplifier, and discriminator to process a pulse is known as dead time.

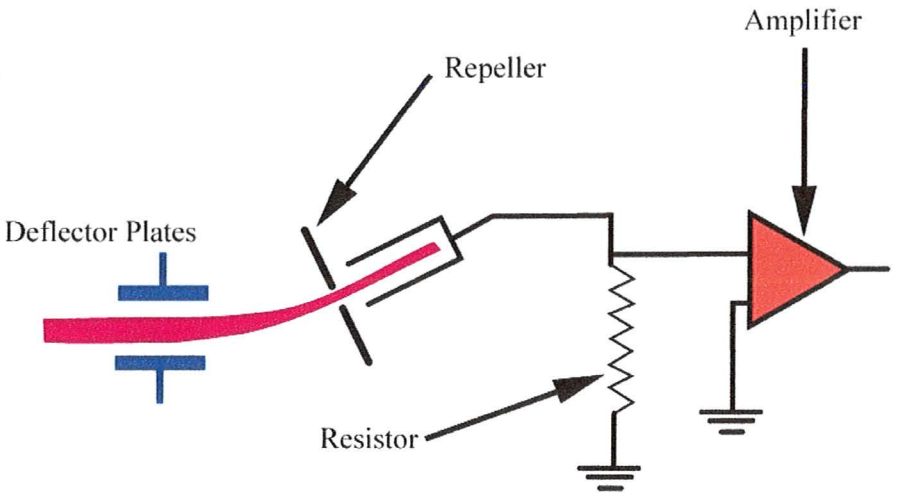

Figure 15 Schematic view of a Faraday cup. A Faraday cup detector can detect rates from $5x10^4$ cps and upwards. Unlike an electron multiplier, it does not discriminate between the type of ion or its energy. The Faraday Cup detector consists of a hollow conducting electrode connected to ground via a high resistance. The ions hitting the collector cause a flow of electrons from ground via a high resistance. The resulting potential drop across the resistor is amplified and passed to the counting circuit.

Table 5 Summary of relative sensitivity factor (RSF) for individual analysis sessions

Standard	Session	RSF	1σ	$(^{230}Th)/(^{238}U)$	1σ	MWSD	n
Arondu Chevkinite	17-Jan-09	0.85	0.08	0.995	0.039	0.5	8
Arondu Chevkinite	17-Nov-08	0.81	0.07	1.010	0.037	0.7	8
AS3 Zircon	18-Jan-09	1.09	0.03	1.005	0.019	0.8	5
AS3 Zircon	1-Oct-08	1.01	0.03	1.013	0.019	2.6	5
AS3 Zircon	18-Nov-08	1.18	0.06	1.003	0.087	N/A	1

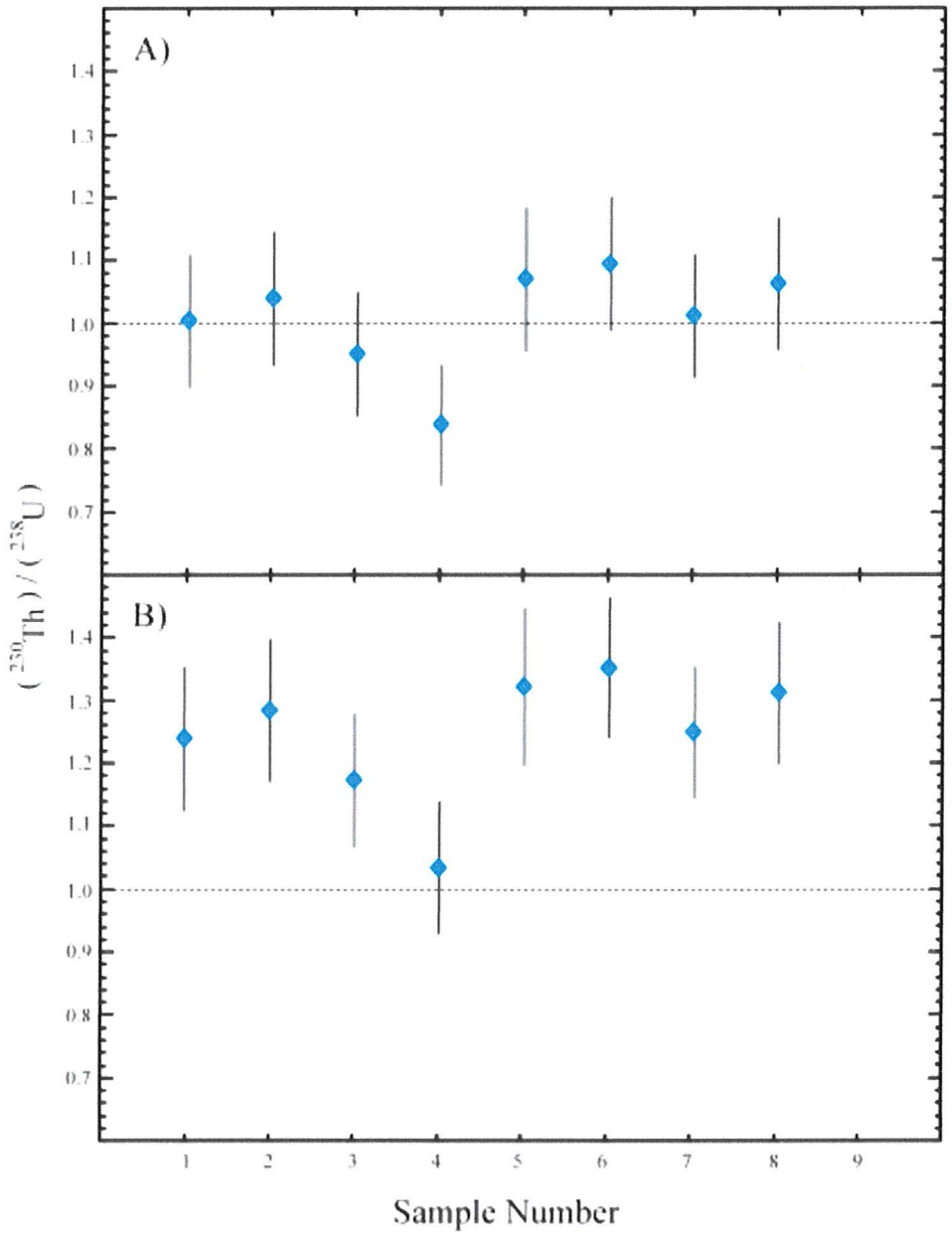

Figure 16 Relative sensitivity factor for November 17, 2008 session in which Arondu chevkinite was used as a standard to determine the detected (^{238}U)/(^{230}Th) relative to the expected secular equilibrium value of (^{238}U)/(^{230}Th) = 1. A) (^{230}Th)/(^{238}U) after application of RSF=0.81 ± 0.07 (MSWD=0.7, N=8). B) (^{230}Th)/(^{238}U) before application of RSF.

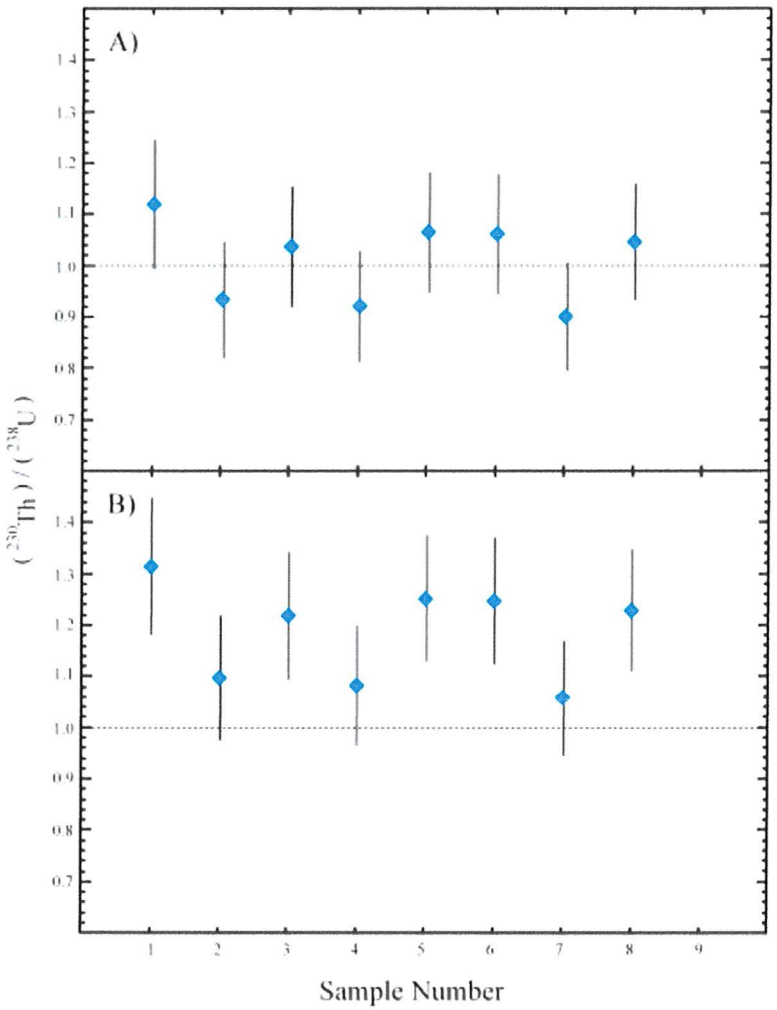

Figure 17 Relative sensitivity factor for January 17, 2009 session in which Arondu chevkinite was used as a standard to determine the detected $(^{238}U)/(^{230}Th)$ relative to the expected secular equilibrium value of $(^{238}U)/(^{230}Th) = 1$. A) $(^{230}Th)/(^{238}U)$ after application of RSF=0.85 ± 0.08 (MSWD=0.5, N=8). B) $(^{230}Th)/(^{238}U)$ before application of RSF.

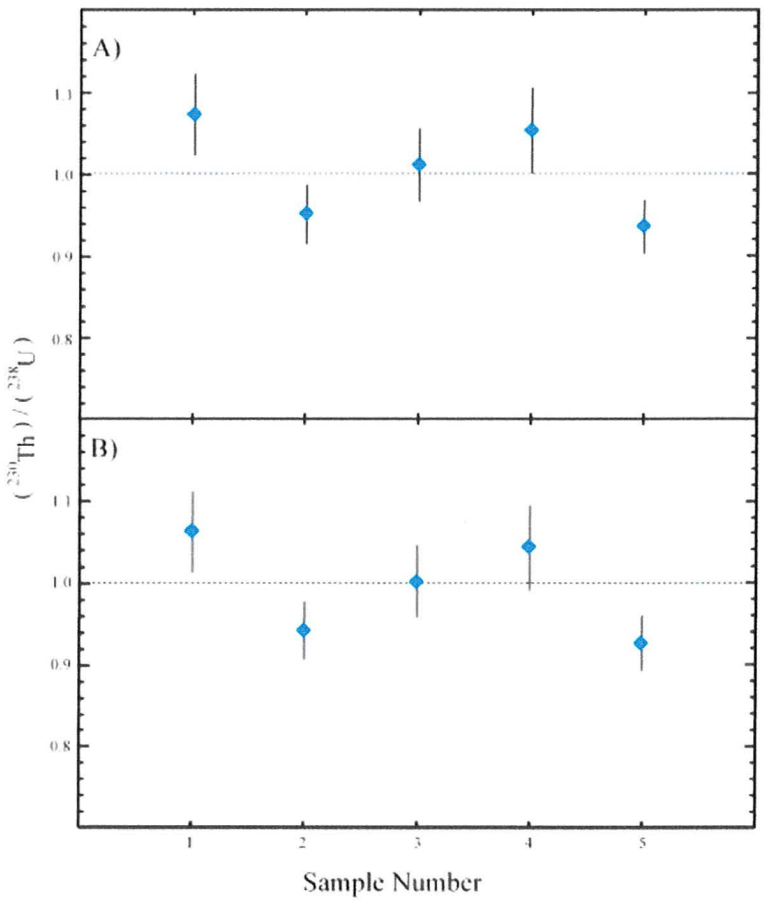

Figure 18 Relative sensitivity factor for October 1, 2008 session in which AS3 zircon was used as a standard to determine the detected (^{238}U)/(^{230}Th) relative to the expected secular equilibrium value of (^{238}U)/(^{230}Th) = 1. A) (^{230}Th)/(^{238}U) after application of RSF=1.01 ± 0.03 (MSWD=2.6, N=5). B) (^{230}Th)/(^{238}U) before application of RSF.

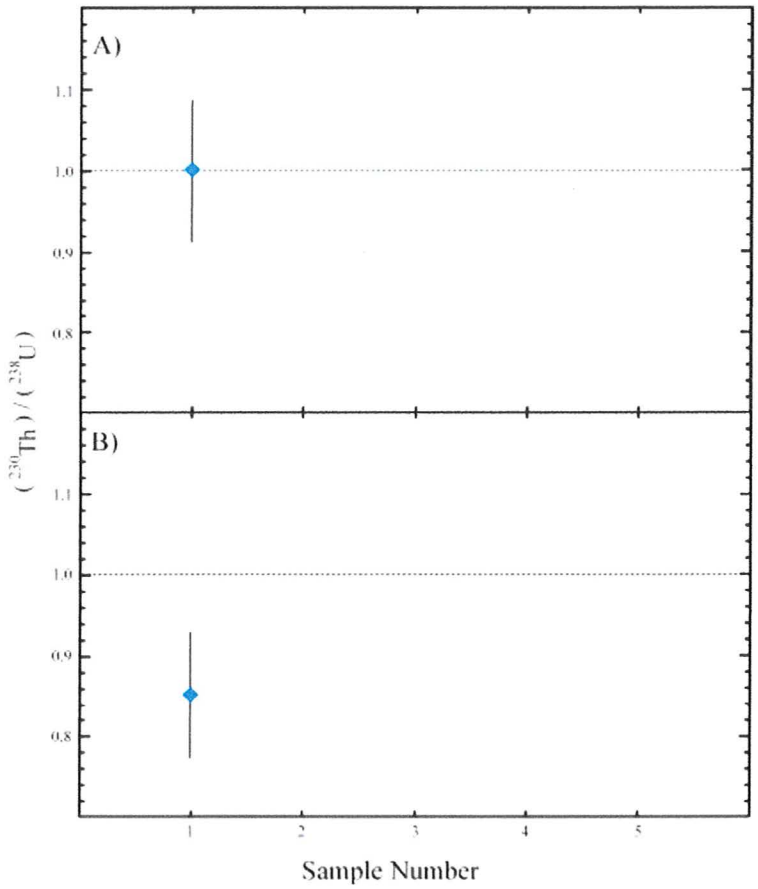

Figure 19 Relative sensitivity factor for November 18, 2008 session in which AS3 zircon was used as a standard to determine the detected (^{238}U)/(^{230}Th) relative to the expected secular equilibrium value of (^{238}U)/(^{230}Th) = 1. A) (^{230}Th)/(^{238}U) after application of RSF=1.18 ± 0.06 (MSWD=N/A, N=1). B) (^{230}Th)/(^{238}U) before application of RSF.

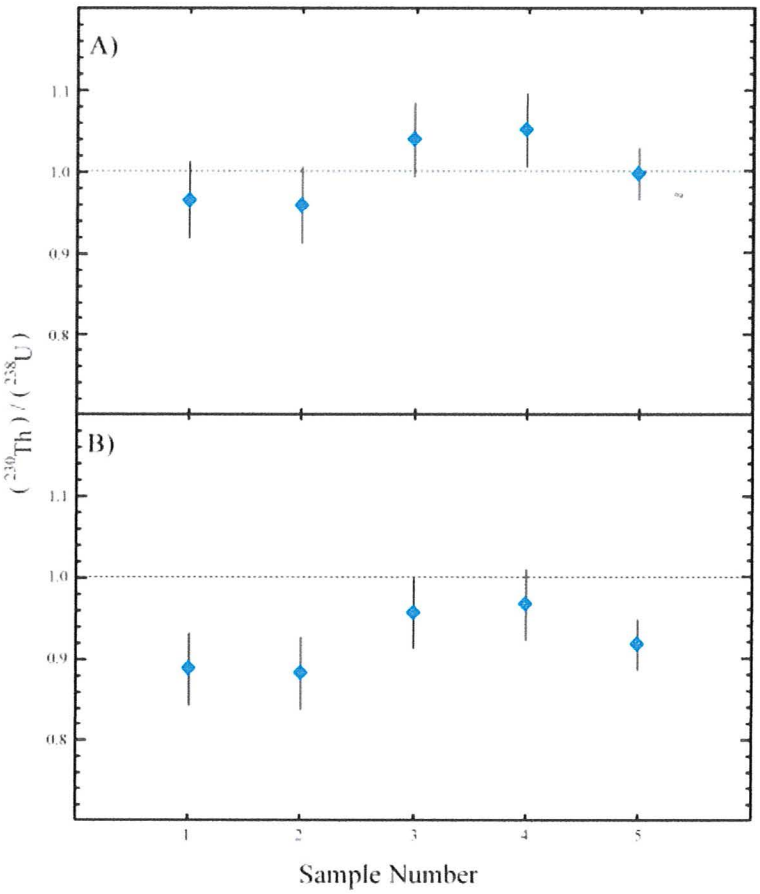

Figure 20 Relative sensitivity factor for January 18, 2009 session in which AS3 zircon was used as a standard to determine the detected (^{238}U)/(^{230}Th) relative to the expected secular equilibrium value of (^{238}U)/(^{230}Th) = 1. A) (^{230}Th)/(^{238}U) after application of RSF=1.09 ± 0.03 (MSWD=0.8, N=5). B) (^{230}Th)/(^{238}U) before application of RSF.

Chapter VI

Results

^{238}U-^{230}Th-^{232}Th Isotope Results

The ^{238}U-^{230}Th-^{232}Th compositions and ratios for chevkinite and zircon from La Primavera samples LP001, LP002B, LP006, and LP008 are summarized in Appendix 4 and Appendix 5. These results report on data from ~4-11 measurements per sample. In several cases where the primary beam overlapped the epoxy, the chevkinites and zircons yielded very high $^{230}Th/^{232}Th$ ratios. These high values likely reflect the generation of $^{232}Th_2{}^{16}O^{12}C^{2+}$ as a result of sputtering of the epoxy surrounding the chevkinite or zircon grains, which interferes at the mass range of $^{230}Th^{16}O^{+}$ (e.g., Schmitt *et al.*, 2006); these spurious results are not considered in the calculation of ages. Other spurious results occur when overlap of chevkinite and zircon occurs(Appendix 3) and yield incoherent results.

Model ^{238}U-^{230}Th ages for individual La Primavera chevkinites and zircons are derived using the U/Th of their host rocks as a model for the initial Th isotope composition of melt during crystallization. Individual model ages reflect the slope of two-point isochrons between single chevkinite analyses and assumed initial $^{230}Th/^{232}Th$ and $^{238}U/^{232}Th$ of whole rock compositions. Initial $^{230}Th/^{232}Th$ and $^{238}U/^{232}Th$ of whole rock for La Primavera samples were not measured directly in this study; instead, they were estimated using the U/Th of host whole rocks as well as the equipoint defined by the $(^{230}Th)/(^{232}Th)$ and $(^{238}U)/(^{232}Th)$ ratios of all the analyzed zircons (Figure 21). The calculated equipoint value is 1.03 ± 0.09. Using U and Th concentrations for 15 postcaldera rhyolites reported by Mahood (1981) and assuming a host melt in ^{230}Th-^{238}U

secular equilibrium, the initial (^{230}Th)/(^{232}Th) is 0.99 ± 0.09 (1 s.d.). These essentially identical values are used to account for the variability of U/Th exhibited by the La Primavera rhyolites for the chevkinite and zircon model ages. Although many rhyolites have ^{230}Th/^{238}U near secular equilibrium (Reagan *et al.*, 2003), peralkaline rhyolites in the literature are reported to have (^{230}Th) excesses of up to 20 % (Bohrson and Reid, 1998; Rogers *et al.*, 2004).

Isochron and model ages (Note: unless otherwise stated, errors reported are given at 1σ or 68% confidence and the model ages are weighted averages) for multiple chevkinites from single lava samples yield variable ages (Appendix 4 and Table 6). The model ages are calculated using a two point isochron between chevkinite or zircon and assumed melt composition based from whole rock U/Th values (described above). Isochron slopes, errors, and ages were calculated using Isoplot 3.0 (Ludwig, 2003).

General results from for this study are as follows: La Primavera chevkinites have average (^{238}U)/(^{232}Th) ratios of 0.098 ± 0.009. Assuming a melt in secular equilibrium during crystallization, 21 chevkinites from lava samples LP001, LP002B, and LP008 define model ages that range from ca. 40 ka to 110 ka (Table 6). The model ages for La Primavera chevkinites have a wide distribution of ages that cluster around 70 ka (Figure 22). In contrast, La Primavera zircons have average (^{238}U)/(^{232}Th) ratios of 5.714 ± 0.188. Assuming a melt in secular equilibrium during crystallization, 29 zircons from samples LP001, LP002, LP006, and LP008 define model ages that range from ca. 65 ka to ca. 120 ka (Appendix 5, Table 6). The model ages for La Primavera zircons show an age distribution that clusters around 115 ka and to a lesser extent at around 70 ka (Figure 23).

Isochron and Model ^{238}U-^{230}Th Ages for La Primavera Chevkinite

Chevkinite model and isochron ages for samples LP001, LP002B, and LP008 are calculated using a whole rock value for (^{230}Th)/(^{232}Th) and (^{238}U)/(^{232}Th) of 1.03 ± 0.09. Reported chevkinite isochrons include this assumed whole rock value because of their restricted U/Th that limits the generation of internal isochrones. Analysis of seven chevkinite crystals from LP001 yields an isochron age of 100 ± 120 ka (MSWD=2.5) (Figure 24) and a mean model age of $88.5^{40.7}_{29.6}$ka with that has a peak probability distribution at ~85 ka (Figure 25). Analysis of seven chevkinite crystals from sample LP002B yields an isochron age of 91 ± 120 ka (MSWD = 3.1) (Figure 26) and a mean model age of $84.0^{40.7}_{29.6}$ka and that has a peak probability distribution ~85 ka (Figure 27). Analysis of seven chevkinite crystals from sample LP008 yields an isochron age of 54 ± 84 ka (MSWD = 3.3) (Figure 28) and a mean model age of $49.4^{29.4}_{23.1}$ka with a peak probability distribution ~ 48 ka (Figure 29).

Isochron and Model ^{238}U-^{230}Th Ages for La Primavera Zircon

Zircon model and isochron ages for samples LP001, LP002B, LP006, and LP008 are calculated without whole rock values because they show sufficient spread in U/Th to form significant internal isochrons. Two isochron ages of LP008 are calculated; one isochron age includes the whole rock value and one does not. Eleven measurements on ten individual zircon crystals from sample LP001 yield a mean model age of $104.9^{14.9}_{13.1}$ka and an isochron age of 115 ± 39 ka (MSWD = 0.47) (Figure 30) with a relative probability distribution which shows unimodal age distribution clustering at ~ 105 ka

(Figure 31). Analyses of seven zircon crystals from sample LP002B yield a mean model age of $113.6^{17.2}_{14.8}$ka and an isochron age of 113 ± 48 ka (MSWD = 0.7) (Figure 32) with a relative probability distribution which shows unimodal age distribution clustering at ~ 113 ka (Figure 33). Analyses of four zircon crystals from sample LP006 yield a model age of $74.1^{12.4}_{11.1}$ka and an isochron age of 56 ± 24 ka (MSWD = 0.47) (Figure 34) with a probability distribution that peaks at ~ 70 ka (Figure 35). Analyses of seven zircon crystals from sample LP008 yield a model age of $101.0^{23.1}_{19.1}$ka and an isochron age of 32 ± 24 ka (MSWD = 0.7) (Figure 36) with a probability distribution that peaks at ~ 90 ka (Figure 37). For sample LP008, an isochron age which includes whole rock for (^{230}Th)/(^{232}Th) and (^{238}U)/(^{232}Th) of 1.03 ± 0.09 gives an age of 102 ± 28 ka (MSWD =1.6, N=8) (Figure 38). Depending on whether a whole rock value is included in the isochron age of LP008, two discordant ages are obtained. The value that includes whole rock composition is preferred since it is concordant with the mean model age. The isochron ages of samples LP001, LP002B, and LP006 do not show a significant age difference when a whole rock value was included in the calculation.

Combined Chevkinite-Zircon Isochron Ages for La Primavera Rhyolite

The isochron ages for each samples LP001, LP002B, and LP008 were calculated using all chevkinite and zircon measurements of each sample (whole rock values were not included). Combining eighteen ^{238}U-^{230}Th-^{232}Th measurements of chevkinite and zircon from sample LP001 yield an isochron age of 102.3 ± 4.1 ka (MSWD = 1.2) (Figure 39) with a peak probability distribution at ~ 105 ka (Figure 40). Fourteen ^{238}U-^{230}Th-^{232}Th measurements of chevkinite and zircon from sample LP002B yield an

isochron age of 108.7 ± 8.2 ka (MSWD = 1.8) (Figure 41) with a peak probability distribution at ~112 ka (Figure 42). Finally, fourteen ^{238}U-^{230}Th-^{232}Th measurements of chevkinite and zircon from sample LP008 yield an isochron age of 92 ± 12 ka (MSWD = 2.3) (Figure 44) with a peak probability distribution which shows an age cluster at ~85 ka and to a lesser extent at ~45 ka (Figure 45).

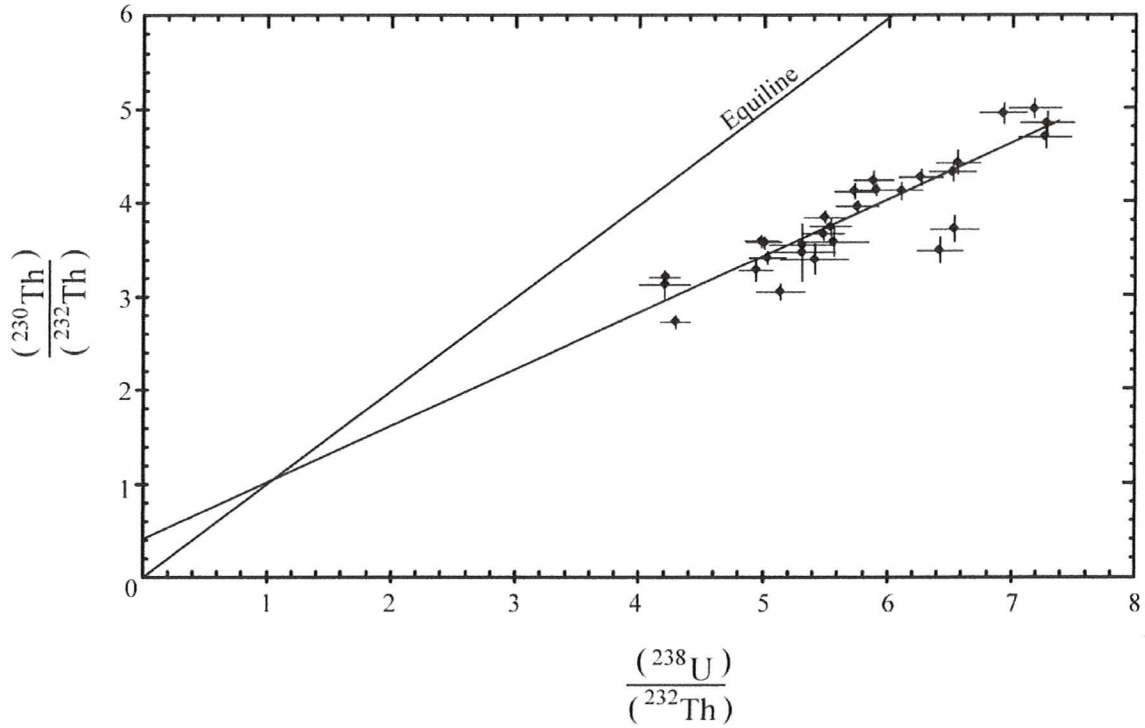

Figure 21. Plot showing intersection of the isochron defined by the (^{230}Th)/(^{232}Th) and (^{238}U)/(^{232}Th) ratios of zircons from all samples and the equiline. Intersection of equiline and isochron indicates an (^{230}Th)/(^{232}Th) and (^{238}U)/(^{232}Th) whole rock value of 1.03 ± 0.09. Whole rock U/Th (Mahood, 1981) suggest a statistically identical value of 0.99 ± 0.09.

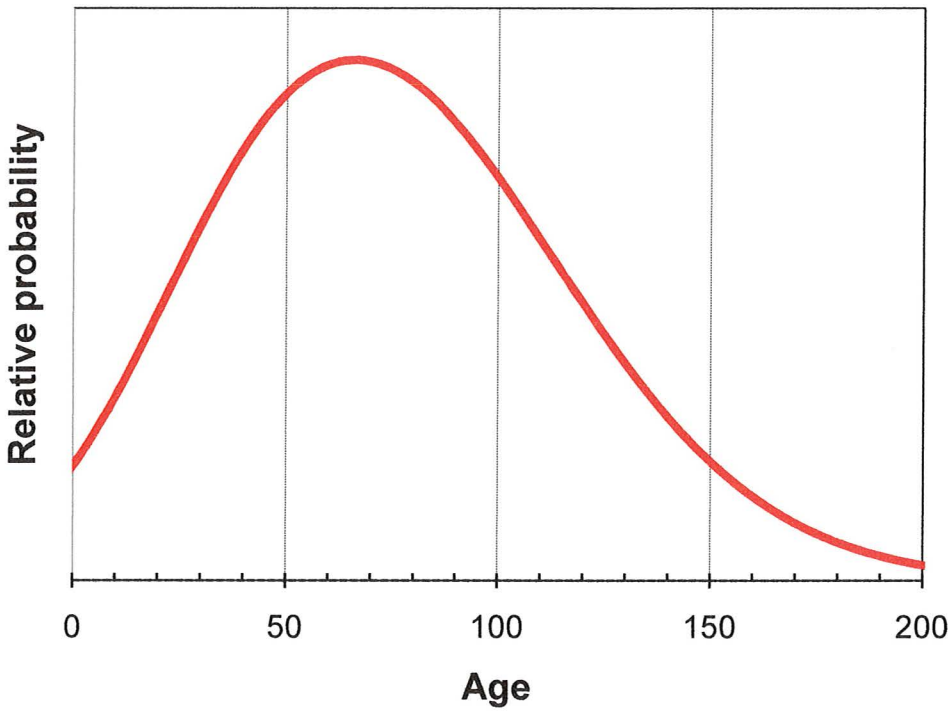

Figure 22. Probability density function curve of model ^{238}U-^{230}Th chevkinite ages of LP001, LP002B, and LP008 (N=21), which shows an age distribution that clusters at ~70 ka.

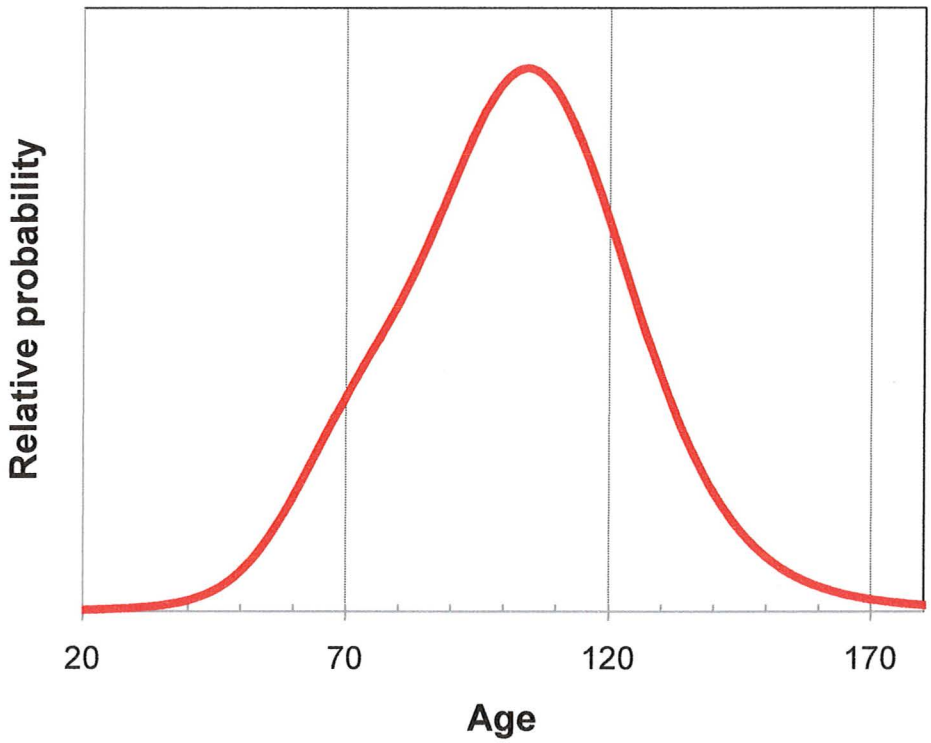

Figure 23. Probability density function curve of model ^{238}U-^{230}Th zircon ages of samples LP001, LP002B, LP006, and LP008 (N=29) shows a well defined age cluster at ~115 ka and a subtle "shoulder" at ~70 ka.

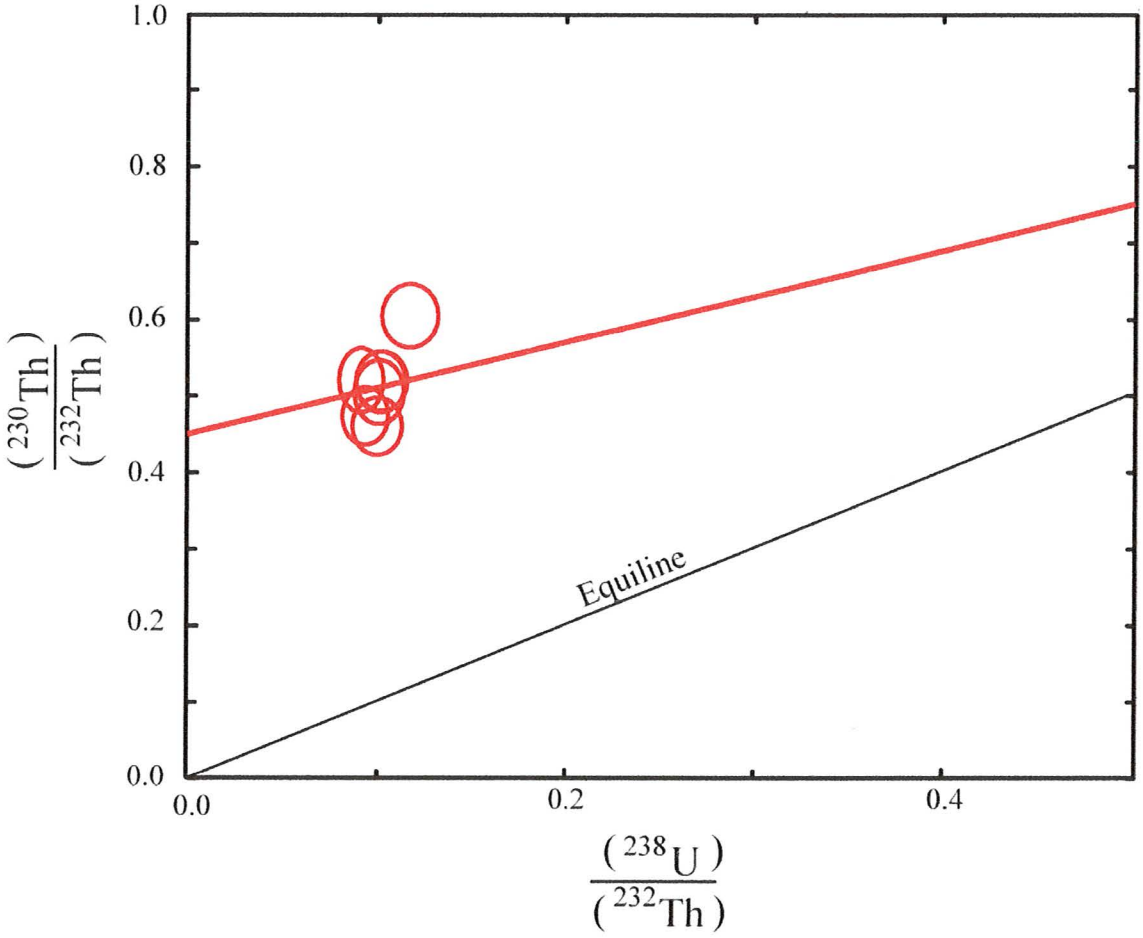

Figure 24. Isochron diagram plotting (^{230}Th)/(^{232}Th) against (^{238}U)/(^{232}Th) for La Primavera chevkinites in sample LP001. LP001 yield a chevkinite-whole rock isochron age of 100 ± 120 ka (MSWD=2.5, N= 8). Isochron age calculation includes whole rock composition (^{230}Th)/(^{232}Th) and (^{238}U)/(^{232}Th) ratios of 1.03 ± 0.09 (Figure 21).

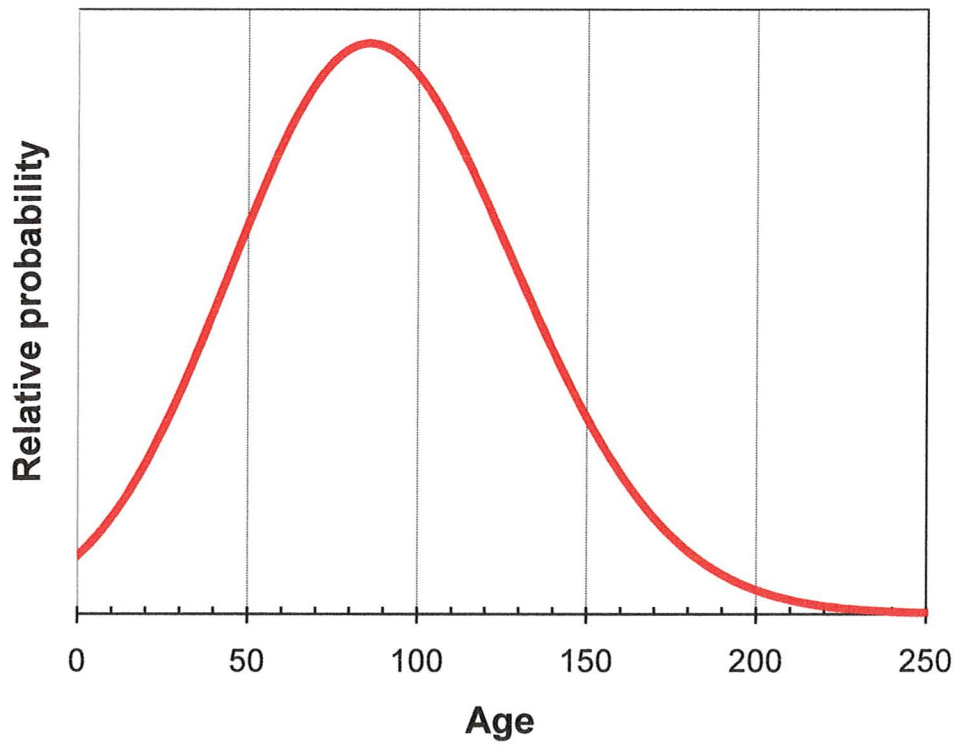

Figure 25 Probability density function curve of model ^{238}U-^{230}Th chevkinite ages of LP001 (N=7) shows unimodal age distribution clustering at ~85 ka.

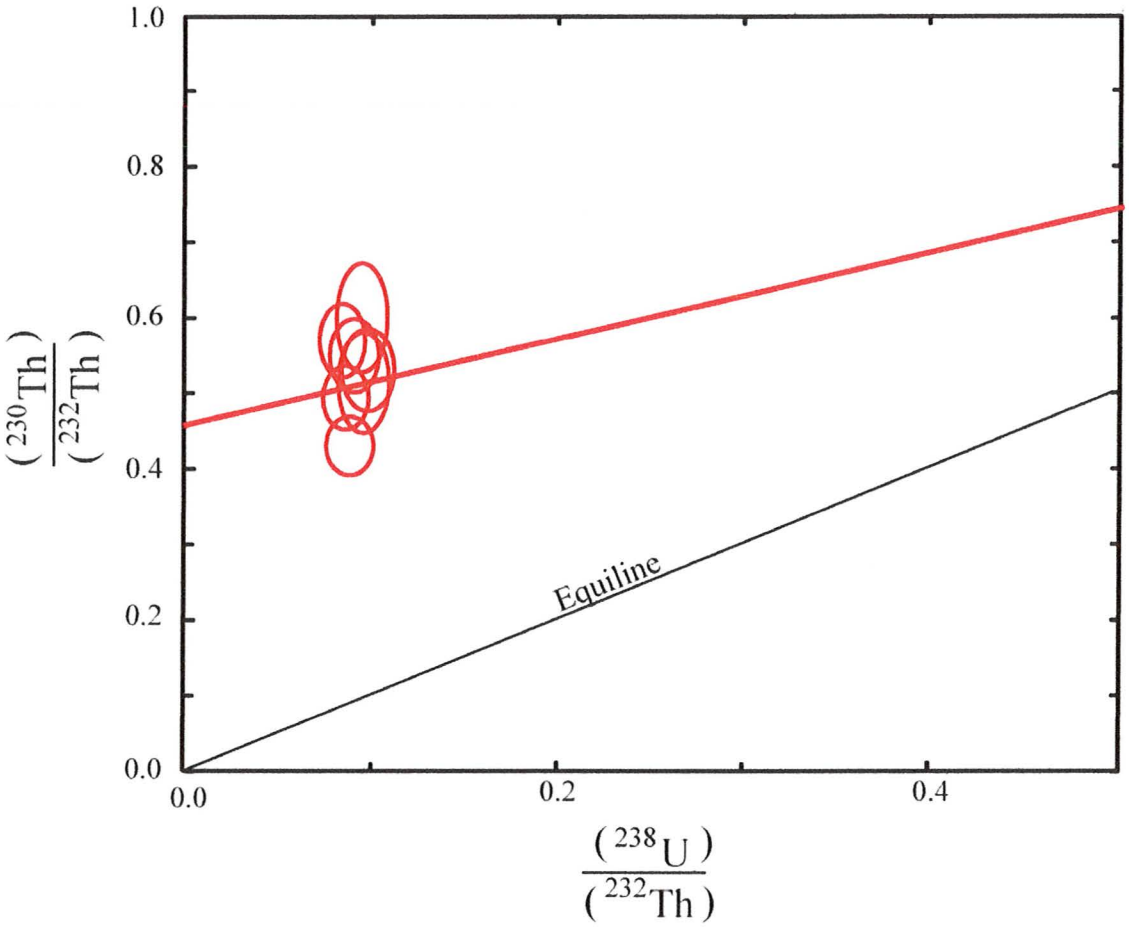

Figure 26 Isochron diagram plotting (^{230}Th)/(^{232}Th) against (^{238}U)/(^{232}Th) for La Primavera chevkinites in sample LP002B. LP002B chevkinite samples yield an isochron age of 91 ± 120 ka (MSWD=3.1, N= 8).Isochron age calculation includes whole rock composition (^{230}Th)/(^{232}Th) and (^{238}U)/(^{232}Th) ratios of 1.03 ± 0.09 (Figure 21).

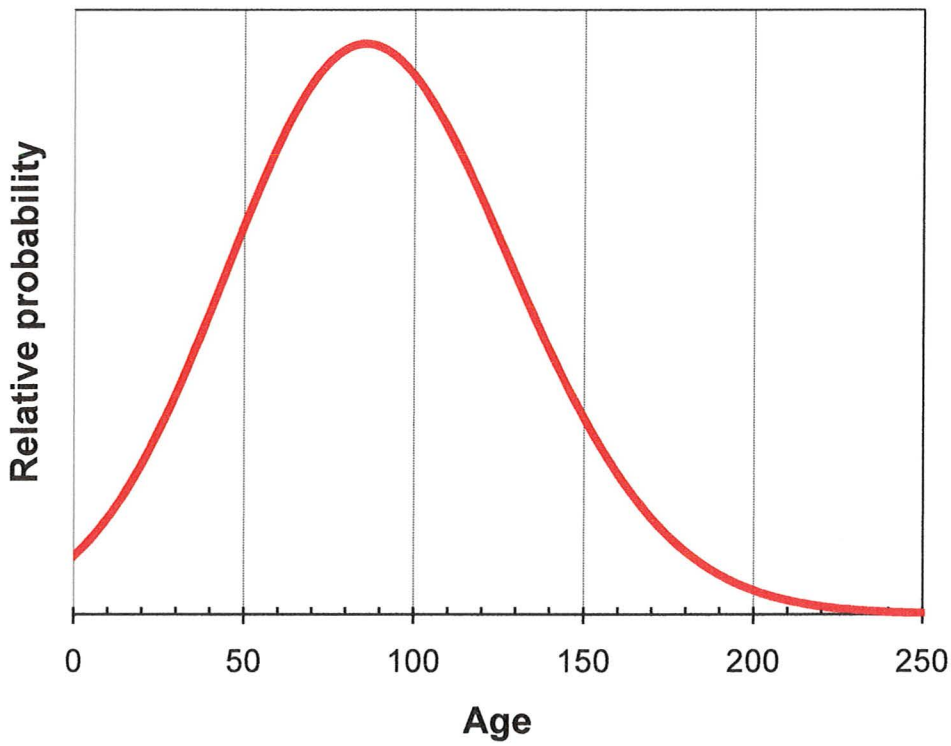

Figure 27 Probability density function curve of model ^{238}U-^{230}Th chevkinite ages of LP002B (N=7) shows unimodal age distribution clustering at ~85 ka.

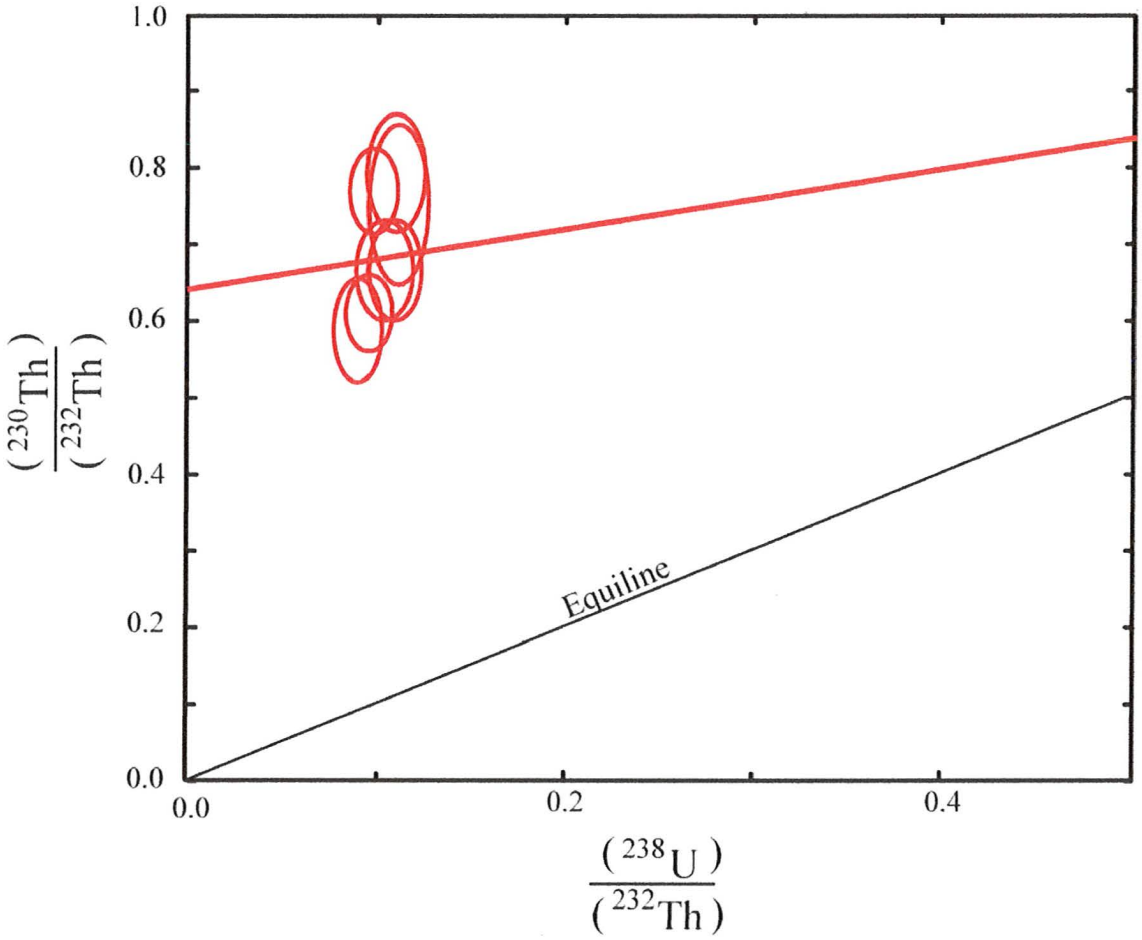

Figure 28 Isochron diagram plotting (^{230}Th)/(^{232}Th) against (^{238}U)/(^{232}Th) for La Primavera chevkinites in sample LP008. LP008 chevkinite samples yield an isochron age of 54 ± 84 ka (MSWD=3.3, N= 8).Isochron age calculation includes whole rock composition (^{230}Th)/(^{232}Th) and (^{238}U)/(^{232}Th) ratios of 1.03 ± 0.09 (Figure 21).

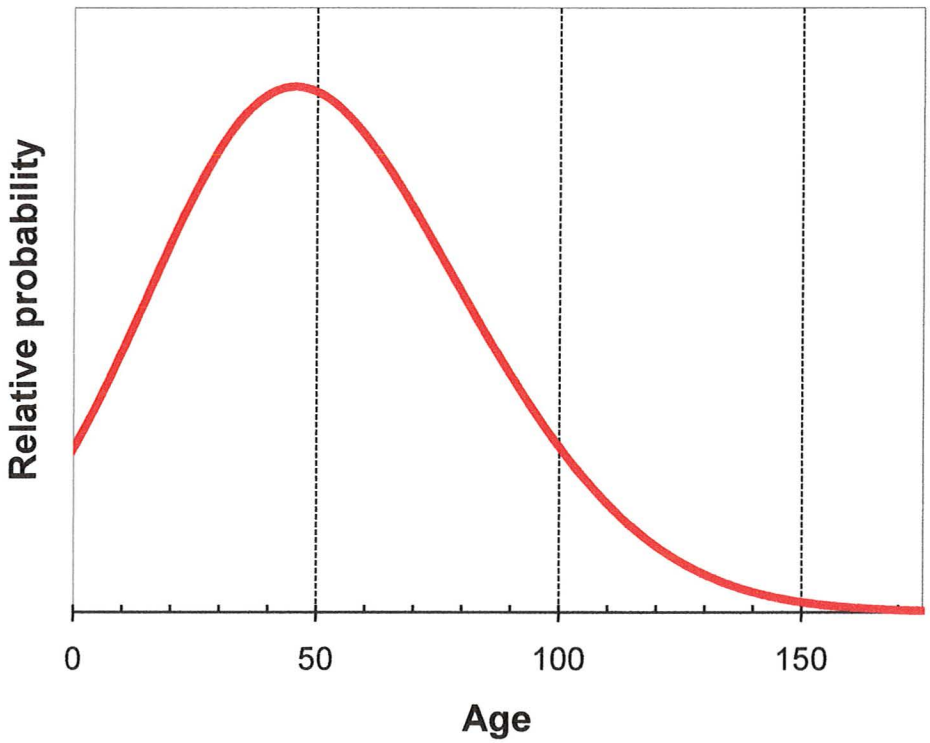

Figure 29 Probability density function curve of model ^{238}U-^{230}Th chevkinite ages of LP008 (N=7) shows unimodal age distribution clustering at ~48 ka.

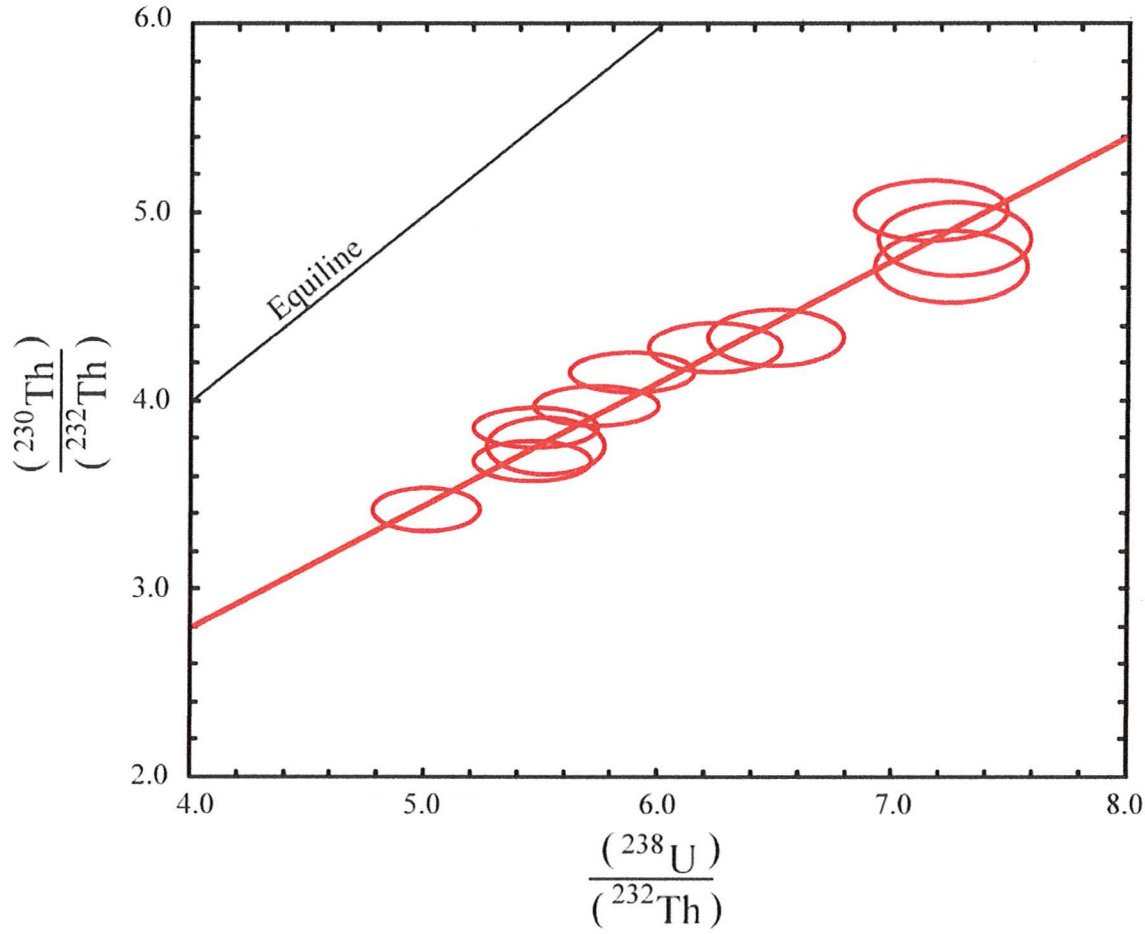

Figure 30 Isochron diagram plotting (^{230}Th)/(^{232}Th) against (^{238}U)/(^{232}Th) for La Primavera zircons in sample LP001. LP001 zircon crystals yield an isochron age of 115 ± 39 ka (MSWD = 0.47, N=11).

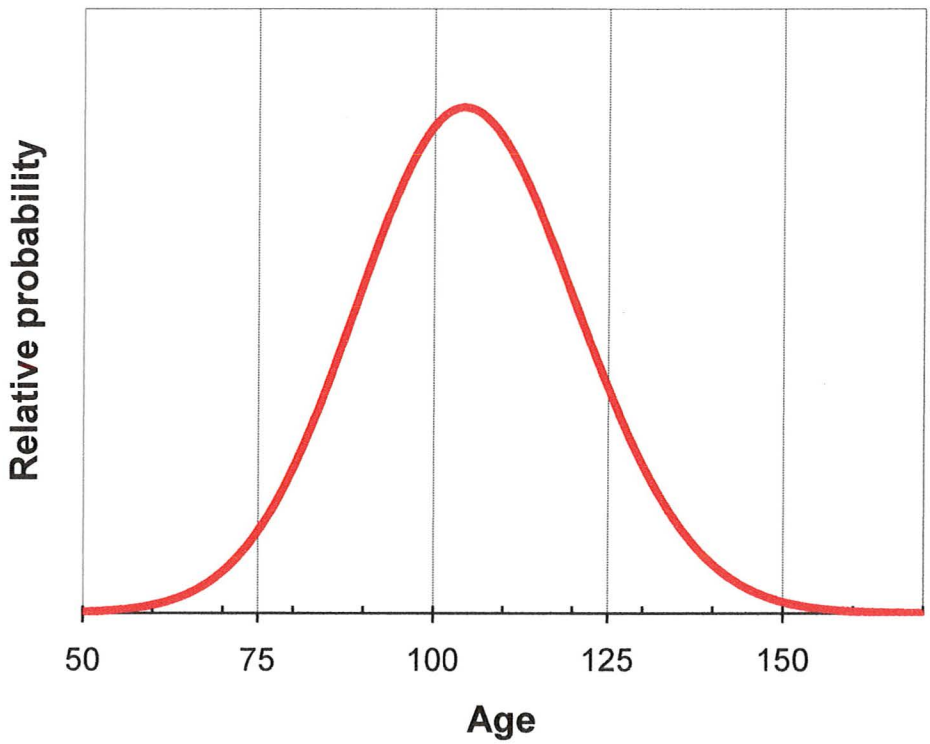

Figure 31 Probability density function curve of model ^{238}U-^{230}Th zircon ages of LP001 (N=11) shows unimodal age distribution clustering at ~105 ka.

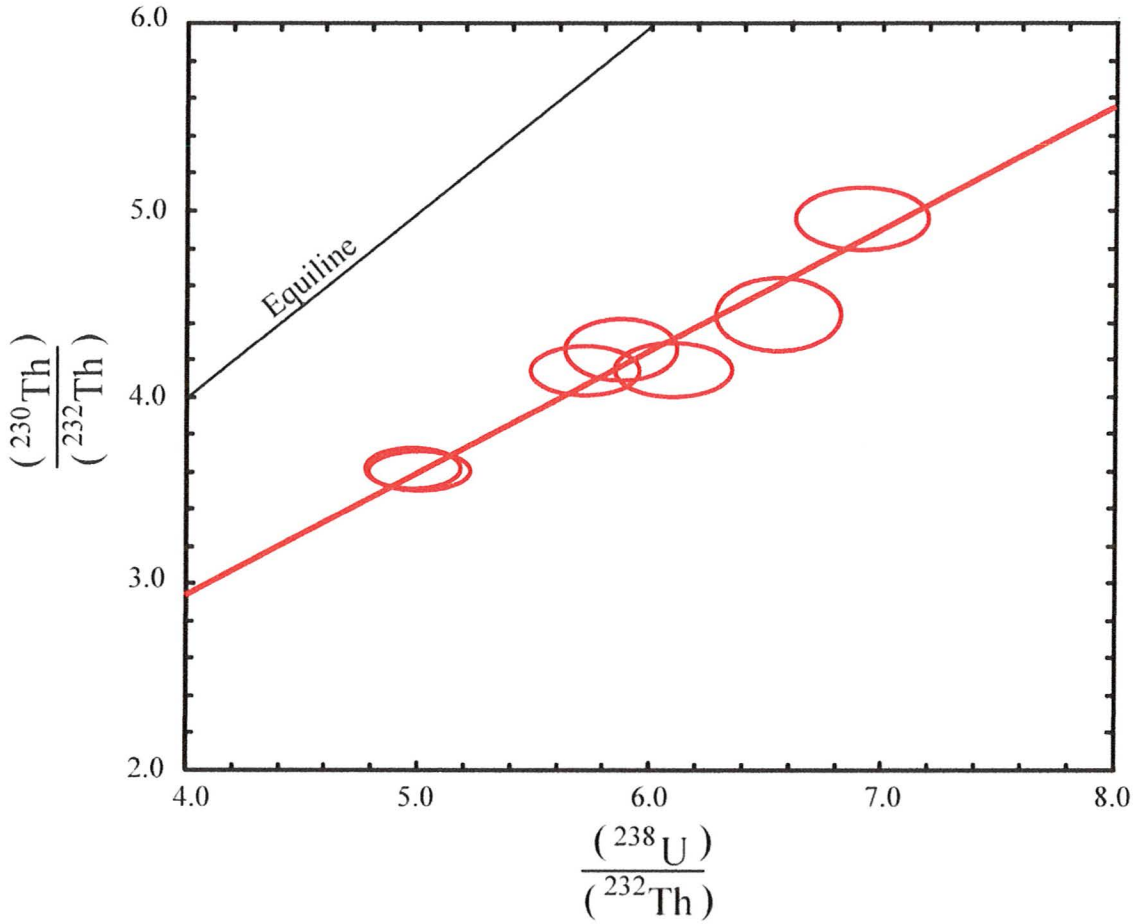

Figure 32 Isochron diagram plotting (^{230}Th)/(^{232}Th) against (^{238}U)/(^{232}Th) for La Primavera zircons in sample LP002B. LP002B zircon samples yield an isochron age of 113 ± 48 ka (MSWD = 0.7, N=7).

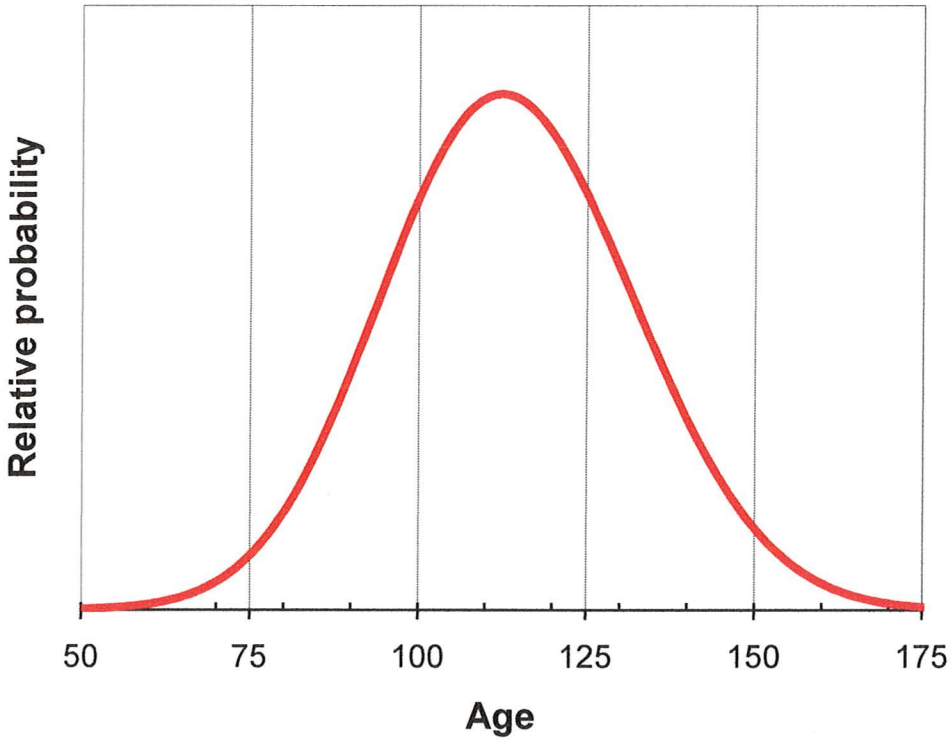

Figure 33 Probability density function curve of model ^{238}U-^{230}Th zircon ages of LP002B (N=7) shows unimodal age distribution clustering at ~113 ka.

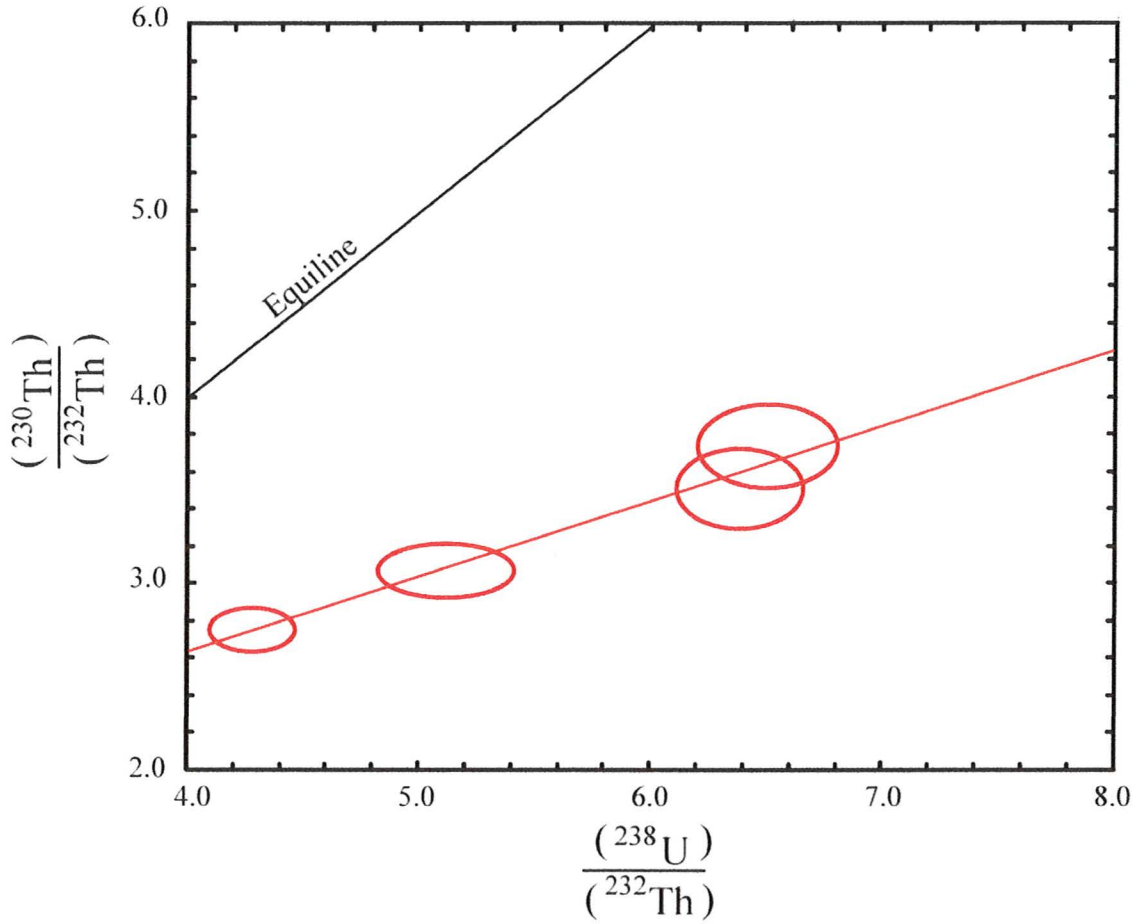

Figure 34 Isochron diagram plotting (^{230}Th)/(^{232}Th) against (^{238}U)/(^{232}Th) for La Primavera zircons in sample LP006. LP006 zircon samples yield an isochron age of 56 ± 24 ka (MSWD = 0.47, N=7).

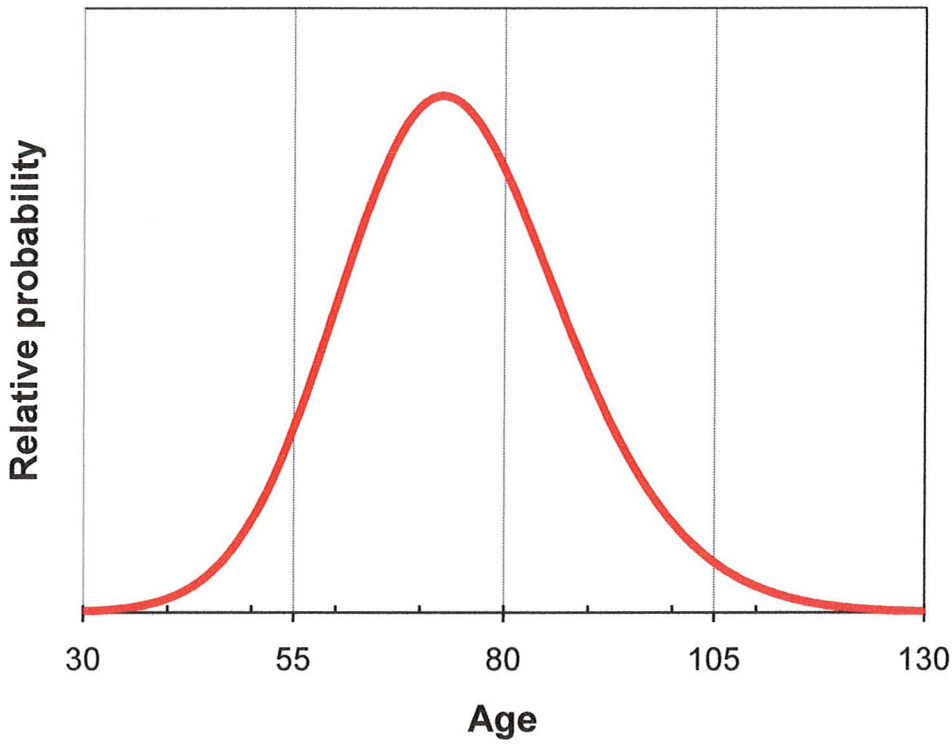

Figure 35 Probability density function curve of model ^{238}U-^{230}Th zircon ages of LP006 (N=4) shows unimodal age distribution clustering at ~70 ka.

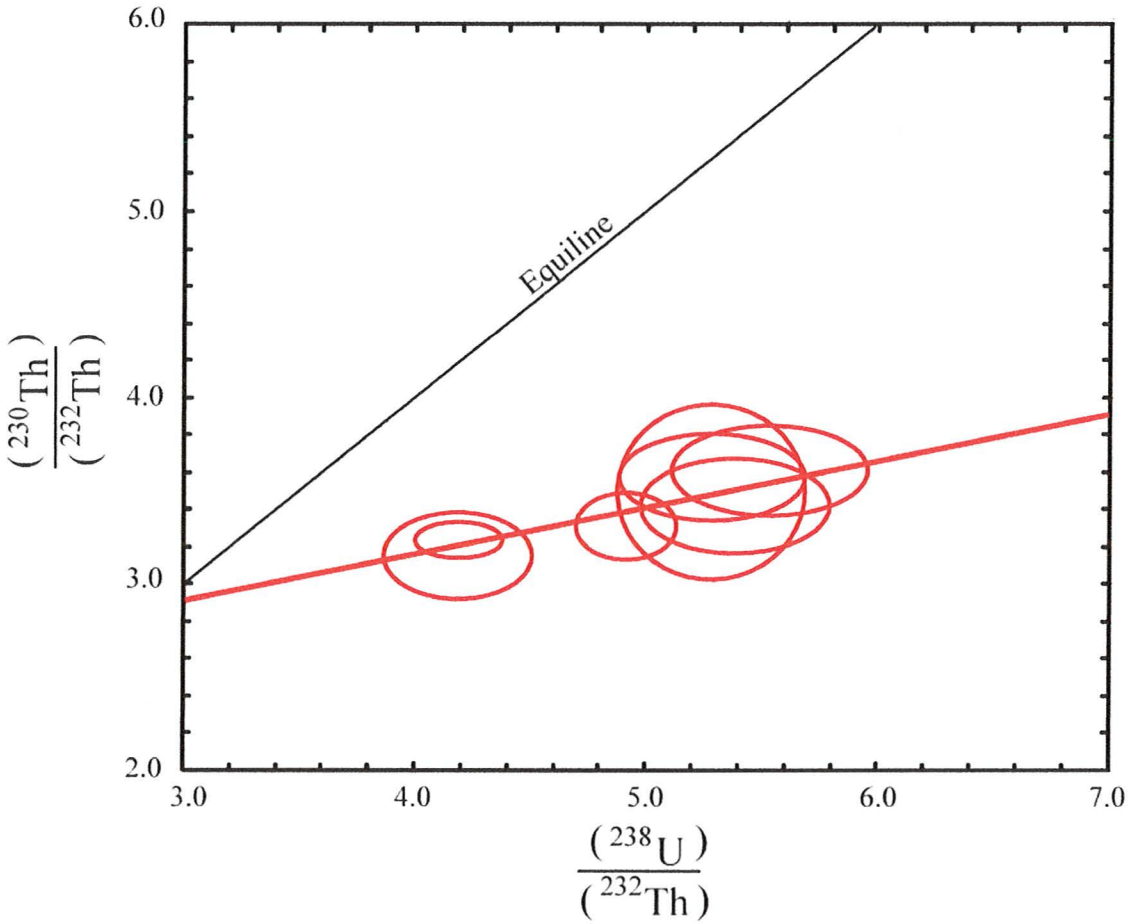

Figure 36 Isochron diagram plotting (^{230}Th)/(^{232}Th) against (^{238}U)/(^{232}Th) for La Primavera zircons in sample LP008. LP008 zircon samples yield an isochron age of 32 ± 24 ka (MSWD=0.27, N= 7).

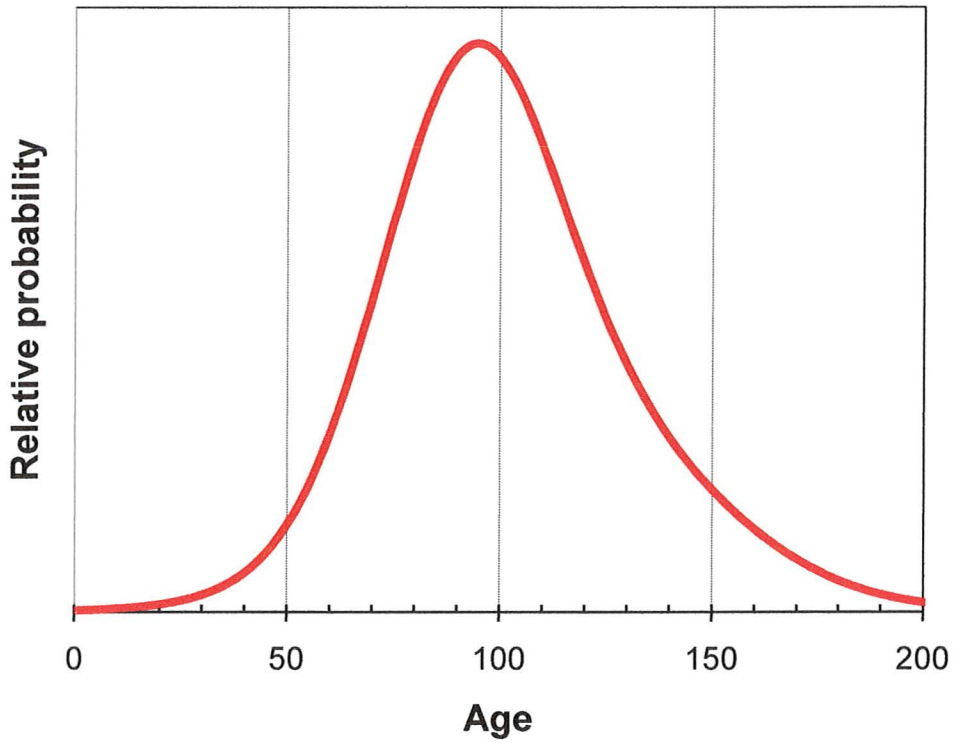

Figure 37 Probability density function curve of model ^{238}U-^{230}Th zircon ages of LP008 (N=7) shows unimodal age distribution clustering at ~90 ka.

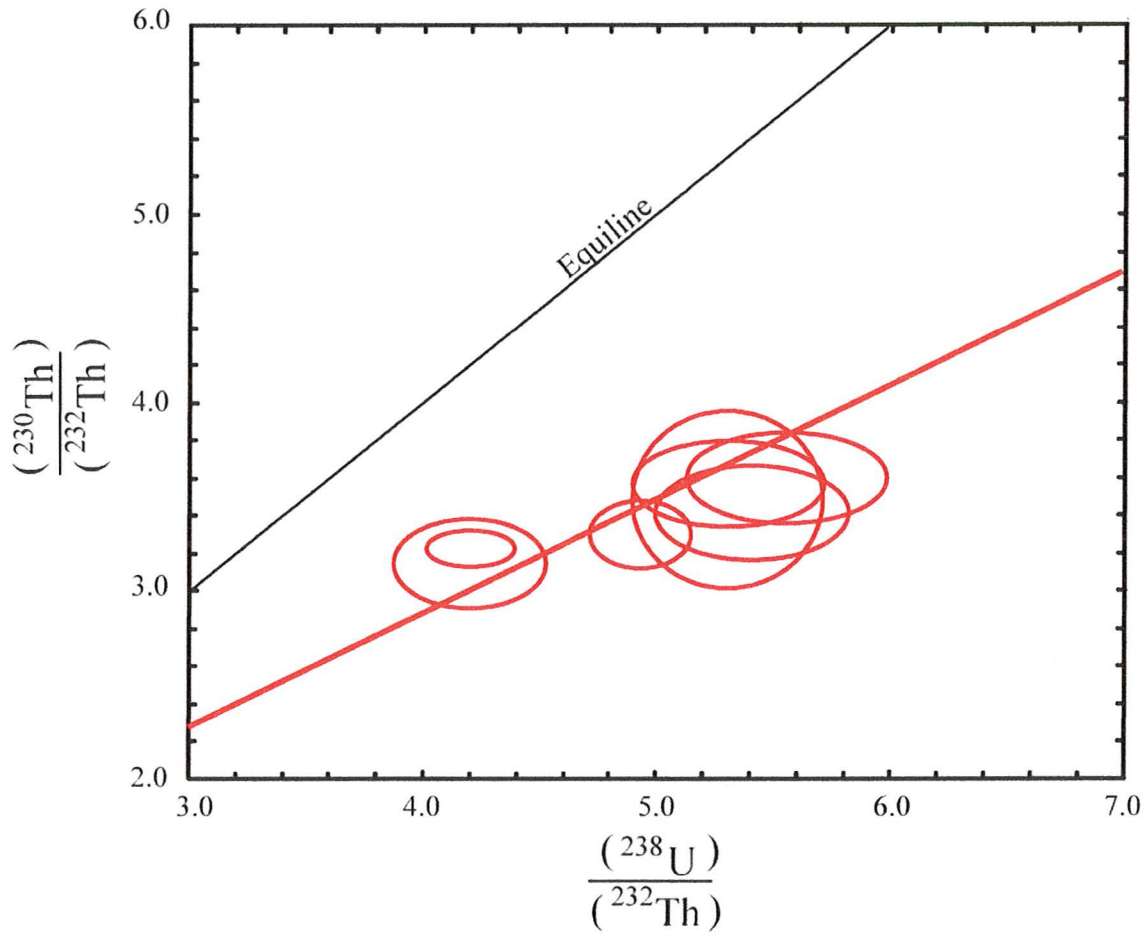

Figure 38 Isochron diagram plotting (^{230}Th)/(^{232}Th) against (^{238}U)/(^{232}Th) for La Primavera zircons in sample LP008. LP008 zircon samples (including whole rock composition) yield an isochron age of 102 ± 28 ka (MSWD=1.6, N= 8).Isochron age calculation includes whole rock composition (^{230}Th)/(^{232}Th) and (^{238}U)/(^{232}Th) ratios of 1.03 ± 0.09 (Figure 21).

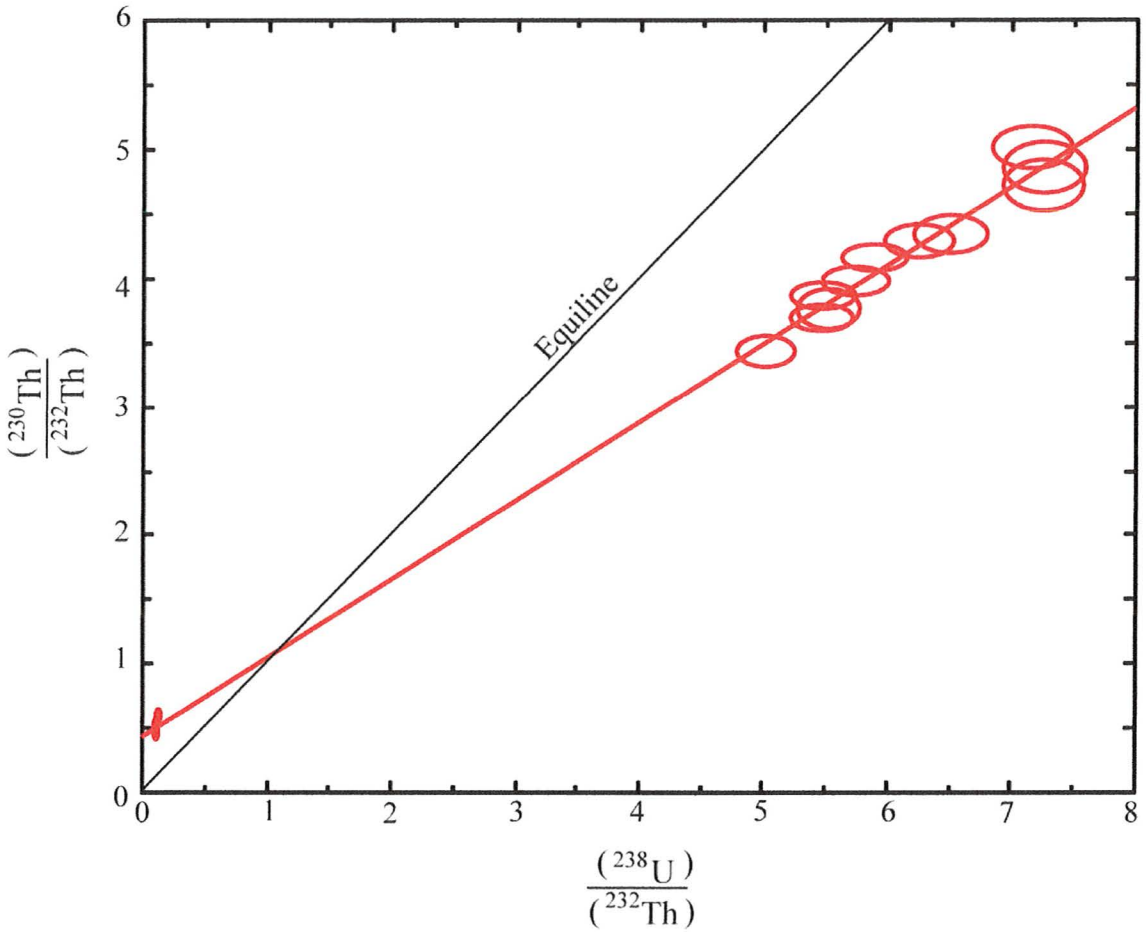

Figure 39 Isochron diagram plotting (^{230}Th)/(^{232}Th) against (^{238}U)/(^{232}Th) for La Primavera chevkinites and zircons in sample LP001. LP001 chevkinite and zircon samples yield an isochron age of 102.3 ± 4.1 ka (MSWD=1.2, N=18).

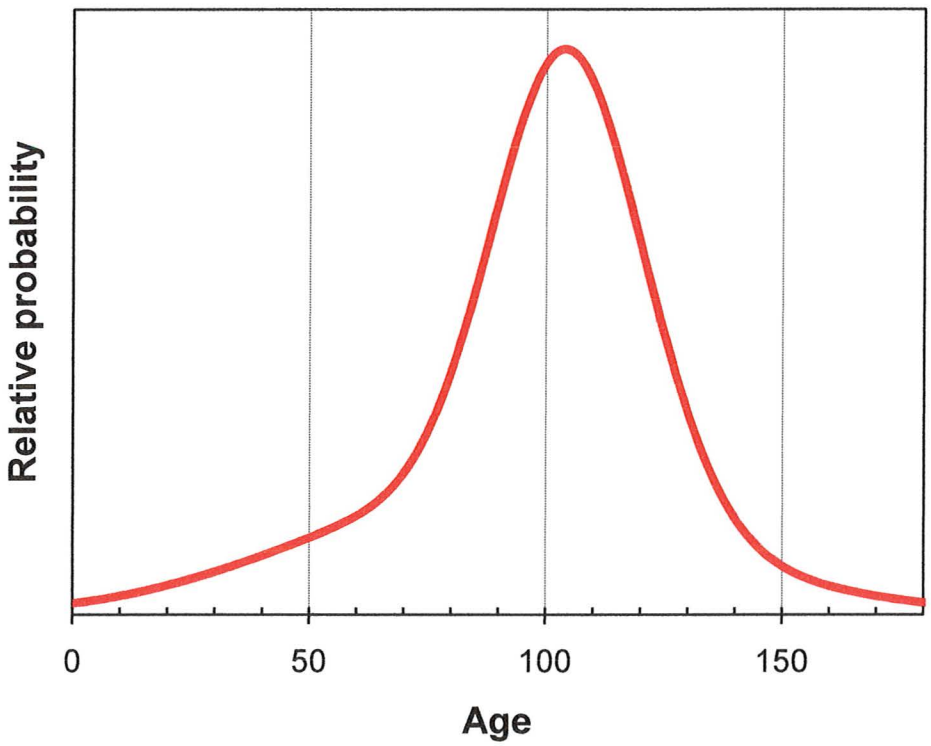

Figure 40 Probability density function curve of model ^{238}U-^{230}Th chevkinite and zircon ages of samples LP001 (N=18) shows a well defined age cluster at ~105 ka.

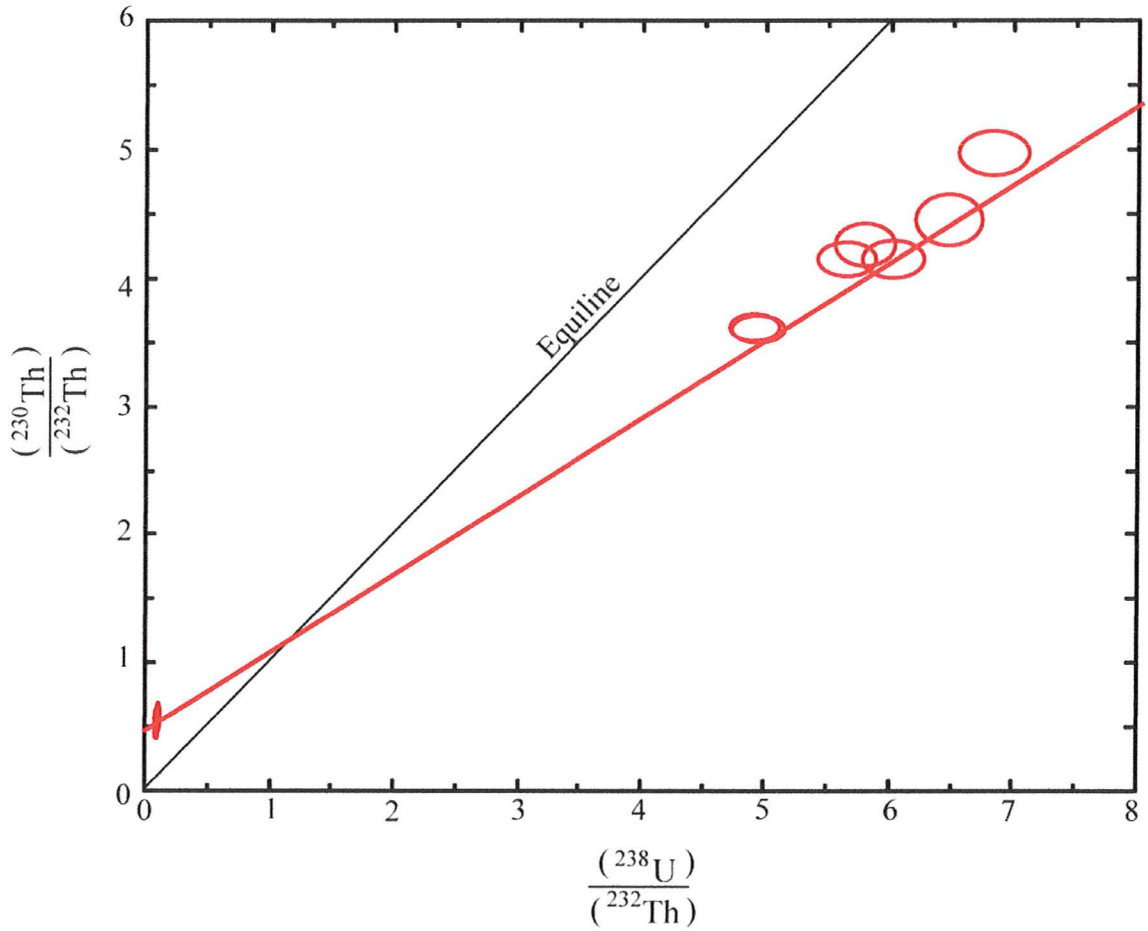

Figure 41 Isochron diagram plotting (^{230}Th)/(^{232}Th) against (^{238}U)/(^{232}Th) for La Primavera chevkinites and zircons in sample LP002B. LP002B chevkinite and zircon samples yield an isochron age of 108.7 ± 8.2 ka (MSWD=1.8, N=14).

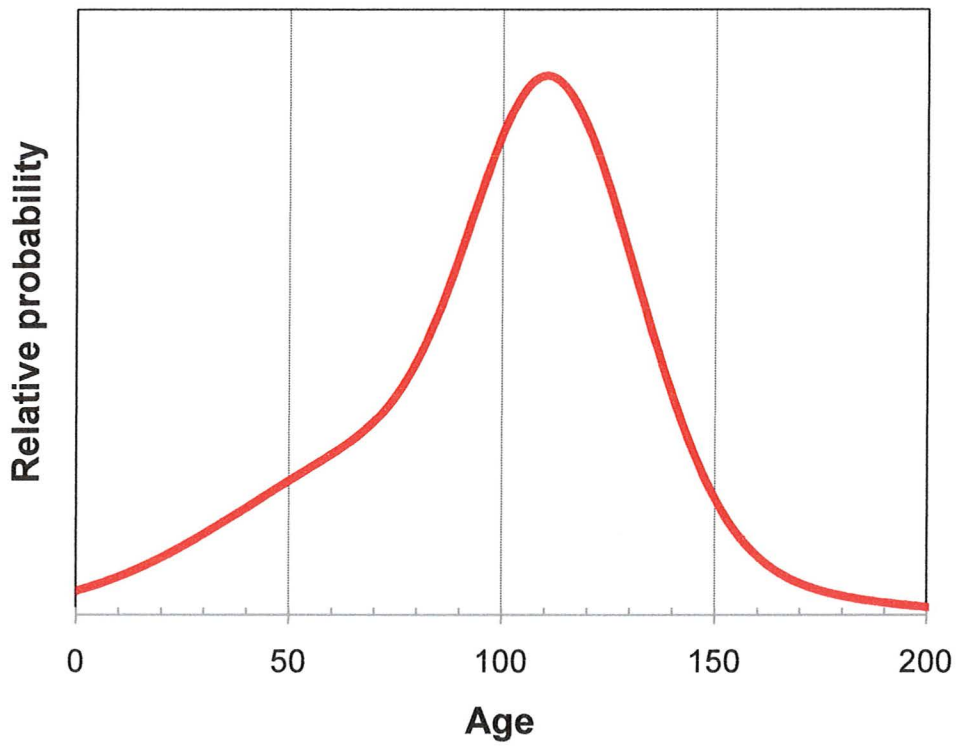

Figure 42 Probability density function curve of model ^{238}U-^{230}Th chevkinite and zircon ages of samples LP002B (N=14) shows a well defined age cluster at ~115 ka.

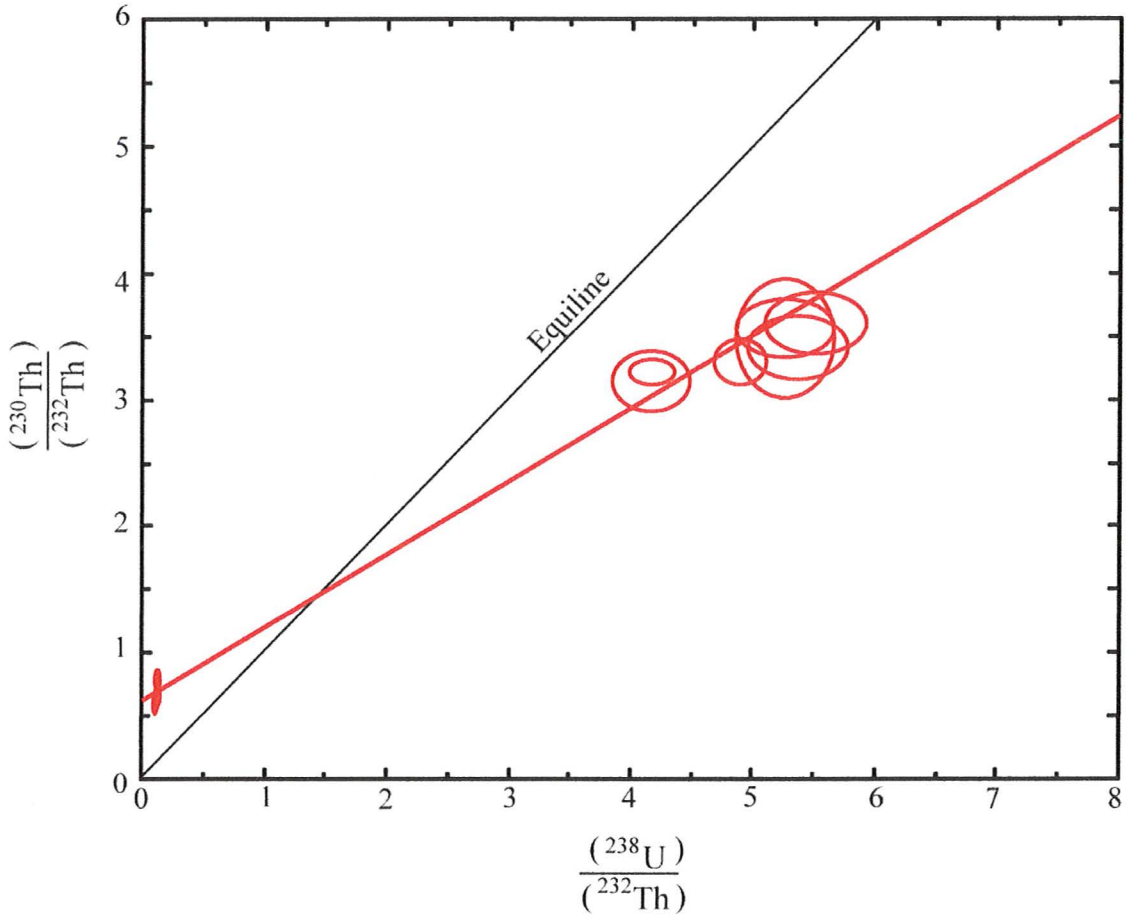

Figure 43 Isochron diagram plotting (^{230}Th)/(^{232}Th) against (^{238}U)/(^{232}Th) for La Primavera chevkinites and zircons in sample LP008. LP008 chevkinite and zircon samples yield an isochron age of 92 ± 2.3 ka (MSWD=2.3, N=14).

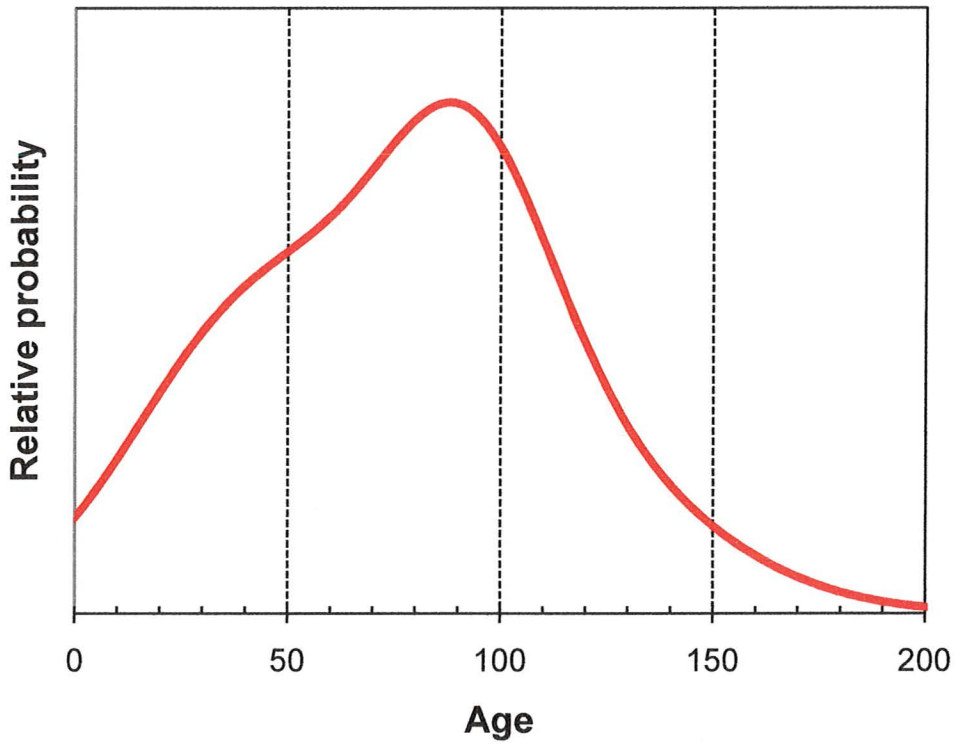

Figure 44 Probability density function curve of model ^{238}U-^{230}Th chevkinite and zircon ages of samples LP001 (N=14) shows an age cluster at ~85 ka and to a lesser extent at ~45 ka.

Chapter VII

Discussion

Given that little is known about U and Th diffusion in chevkinite, it is necessary to establish whether the chevkinite ages reflect crystallization, cooling through a closure temperature, or re-equilibration. The U-Th chevkinite ages may be evaluated by 1) comparing the ages to those from apparently coeval zircon, and 2) comparing the thermochemical conditions at which chevkinite and zircon crystallize. Zircon dating is well established, and zircon crystallization ages in La Primavera rhyolites provide a framework for the timing of magma crystallization which the ages for chevkinite should occur within. The square of weighted deviates (MSWD) values from zircon isochrons of LP001, LP002B, LP006, and LP008 all fall within the 95% confidence intervals for the small number of observations (ages). Hence, a weighted-mean model age or internal isochron age for each zircon population may be calculated (Wendt and Carl, 1991).

The U-Th isotope compositions of La Primavera chevkinite suggest a wider range of crystallization ages than those for associated zircon (Table 1). The MSWD values from chevkinite-whole rock isochrons of LP001, LP002B, and LP008 (2.5, 3.1, 3.3,respectively, n=8 for all three) are outside the 95% confidence interval, suggesting geological scatter, i.e., multiple crystal populations (Wendt and Carl, 1991). Nevertheless, chevkinite and zircon isochron and model ages in samples LP001 and LP002B ages overlap within uncertainties (Table 1). For sample LP008, chevkinite and zircon isochron and model ages overlap within analytical uncertainty but the weighted ages are different; isochron and model ages for chevkinite in sample LP008 are 54 ± 84 ka and $49.4^{29.4}_{23.1}$ka respectively, whereas zircon isochron and model age are 102 ± 28 ka

and $101.0^{23.1}_{19.1}$ka respectevely (Table 1). The uncertainties associated with the chevkinite ages partly reflects the standard error of the ion probe measurements (Table 6). Standard error for chevkinite (^{238}U)/(^{232}Th) and (^{230}Th)/(^{232}Th) activity ratios is on the order of 10% and 5% respectively (compared to standard errors in zircon measurements of less than 3%). This is due to the low amounts of ^{230}Th in the chevkinite, which unlike in zircon, decreases with time. Obviously, the relatively large errors on the measurements of Th-isotope activity has a significant influence the precision of ages derived for a given sample.

The similar ages between chevkinite and zircon are reasonable. Zircon and chevkinite crystallize at similar temperature ranges, 750-1020°C versus 900-1050°C, respectively (Watson and Harrison, 1993; Green and Pearson, 1988). Therefore, it is conceivable that both zircon and chevkinite in the crystal-poor La Primavera rhyolites crystallized close in time. Indeed, there are many examples where chevkinite occurs as inclusions within zircon grains (Figure 6, Appendix 3); which confirms that La Primavera chevkinite and zircon at least partly crystallized under the same thermochemical conditions. Green and Pearson (1988) determined that in evolved, silica-rich magmas, enrichment in REE becomes the key compositional parameter for stabilizing REE-rich minerals. Once chevkinite saturates, its fractionation from the host magma will significantly lower the REE concentrations of derivative melts. As a result, LREE depletion will occur relative to HREE, and magmas derived from fractionation including chevkinite are likely to record a progressive increase in the HREE/LREE ratio (Green and Pearson, 1988). Mahood and Hildreth (1983) conclude that the broad range of apparent partition coefficients for La Primavera rhyolites cannot be attributed to changes

in temperature, pressure of equilibration, or major-element compositions of phenocrysts phases. Instead, bulk composition of the melt is responsible for the broad range of partition coefficients. Accordingly, differences in the ages between zircon and chevkinite may reflect differences between zircon saturation, which is controlled by melt alkalinity and Zr concentration (Watson and Harrison, 1983), and chevkinite saturation which is related to melt LREE concentration (Green and Pearson, 1988).

The ^{238}U-^{230}Th-^{232}Th chevkinite and zircon isochron and model ages obtained in this study are (within error) concordant with K-Ar eruption ages obtained by Mahood and Drake (1982) (Table 6). The ^{238}U-^{230}Th chevkinite crystallization ages for individual samples (with respect to zircon ages and eruption ages) are discussed later in this section but a general discussion follows. The K-Ar eruption ages obtained by Mahood and Drake (1982) and the U-Th crystallization ages of chevkinite and zircon obtained by this study overlap within uncertainty of one another. By analogy to other silicates such as allanite, U-Th within chevkinite is likely to be sufficiently slow so that the isochron ages obtained denote the time of magma crystallization and not a cooling through a lower closure age as with Ar in sanidine. The resolution of inherited U-Th-Pb in chevkinite from granite (Grew and Manton, 1979) suggests that these elements are essentially immobile at magmatic temperatures. Additionally, the concordant crystallization ages of chevkinite and zircon to those of the K-Ar eruption age imply that the studied chevkinite and zircon grains are autocrysts (Miller *et al.*, 2007) rather than antecrysts or xenocrysts (e.g., Reid *et al.*, 1997). From the perspective of isochron ages alone, ^{238}U-^{230}Th isochron ages derived from all chevkinite and zircon analysis of each sample suggest that chevkinite and zircon crystallized at nearly the same time around 105 ka. The near-unity

MSWD values for the combined chevkinite-zircon isochrons for LP001, LP002B, and LP008 suggest that the chevkinite-zircon isochron ages provide the most precise ages of crystallization in the rhyolites. Unlike zircon, the relatively limited spread in U-Th precludes precise dating using chevkinite-only isochron. However, when combined with zircon, extreme leverage is provided for isochrons and highly precise ages may be derived.

Chevkinite and Zircon Ages for Individual Rhyolite Lavas

In the following section, the ages obtained for chevkinite are evaluated and compared against the zircon and K-Ar eruption ages reported in this study and by Mahood and Drake (1982), respectively. In addition, the significance and/or implications of these ages within the La Primavera magmatic system are briefly discussed.

LP001 (Unknown Dome)

Figure 3 shows the locality where sample LP001 was collected. Since LP001 does not lie within the mapped boundaries of the two nearby domes, it is necessary to constrain its source. The LP001 collection locality lies ~100 m east of the (approximate) boundary of the Rio Salado Dome and ~500 m north of the (approximate) boundary of Cerro El Pedernal. Sample LP001 comes from an area that lies within the caldera and is primarily composed of caldera lake sediments that are uplifted (Mahood, 1980). During collection of sample LP001, the uplifted terrain was interpreted to be part of Cerro El Pedernal. However, subsequent re-evaluation of aerial photographs suggests that the sampled locality is not part of Cerro El Pedernal.

Chevkinite and zircon U-Th ages of LP001 give an age of crystallization circa 100 ka (Table 6). Given the somewhat large uncertainty in the individual chevkinite and zircon model ages (Table 6), it is unclear if this sample is part of Rio Salado dome (Pre-caldera lava ~120 ka) or Cerro El Pedernal (younger ring dome ~75 ka) or an unrelated rhyolite of unknown eruption age. One possibility is that sample LP001 represents one of the ~95 ka older ring dome that has been uplifted by resurgence of the caldera. If LP001 came from a pre-caldera lava or an older ring dome, then chevkinite and zircon crystallization occurred at or within several thousand years before eruption. If LP001 came from a ~ 75 ka younger ring dome, then crystallization of chevkinite and zircon would have occurred several tens of thousands of years before eruption. Analysis of the trace element or isotopic composition of LP001, or even K-Ar dating, might help correlate this rhyolite to another dome. Regardless of the eruption age, the model and isochron U-Th ages of chevkinite and zircon in LP001 are essentially identical (Table 6), which supports the validity of the chevkinite ages and the utility of ^{238}U-^{230}Th dating of chevkinite. If we assume that crystallization of chevkinite and zircon occurred concurrently, then a chevkinite-zircon isochron can be used to derive a relatively precise age of 102.3 ± 4.1 ka (1σ) for crystallization.

LP002B (Rio Salado Dome)

The collection locality of sample LP002B lies within the mapped boundaries of the pre-caldera Rio Salado dome (Figure 45 and Appendix 1). Chevkinite isochron age and model age give crystallization somewhat imprecise ages of 90 ± 120 ka and $84.0^{40.7}_{29.6}$ka, respectively, whereas zircon model age and isochron age give a

crystallization age of $113.6^{17.2}_{14.8}$ka and 113 ± 48 ka respectively (Table 6). The chevkinite-zircon isochron yields an age of 108.7± 8.2 ka. The ages obtained for LP002B match the K-Ar eruption age of 123.3±1.9 ka that is reported by Mahood and Drake (1982). The model and isochron U-Th ages of chevkinite and zircon in LP002B agree well given their uncertainties.

LP006 (Pinar de la Venta Dome)

Zircon ages obtained from sample LP006 (Table 6) are younger than the ~95 ka K-Ar age for the same dome obtained by Mahood and Drake (1982). However, the number of dated zircon is too small for robust interpretation. With only four zircon ages and zero chevkinite ages and an uncertain initial ^{238}U-^{230}Th, it is difficult to derive a precise isochron age from the zircons. More dating of zircons from this rhyolite is required (chevkinite was not found for this sample even after multiple attempts at heavy mineral grain separation).

LP008 (Arroyo Ixtahuatonte Dome)

Sample LP008 comes from Arroyo Ixtahuatonte dome (Appendix 1). Mahood and Drake (1982) include this dome in the group of younger ring domes and obtained an eruption age of 83.6 ± 2.0 ka. Individual zircon and chevkinite isochron and model ages give imprecise ages (Table 6). The zircon isochron ages yield an age of 102 ± 28 ka , while chevkinite-zircon isochron ages yield the most precise ages for time of crystallization. If correct, the chevkinite-zircon isochron age 92±12 suggests that crystallization occurred within 8.4 ±12.2 ka before eruption. Hence, the zircon-

chevkinite ages suggest negligible pre-eruptive residence times for the rhyolites (cf. Reid *et al.*, 1997).

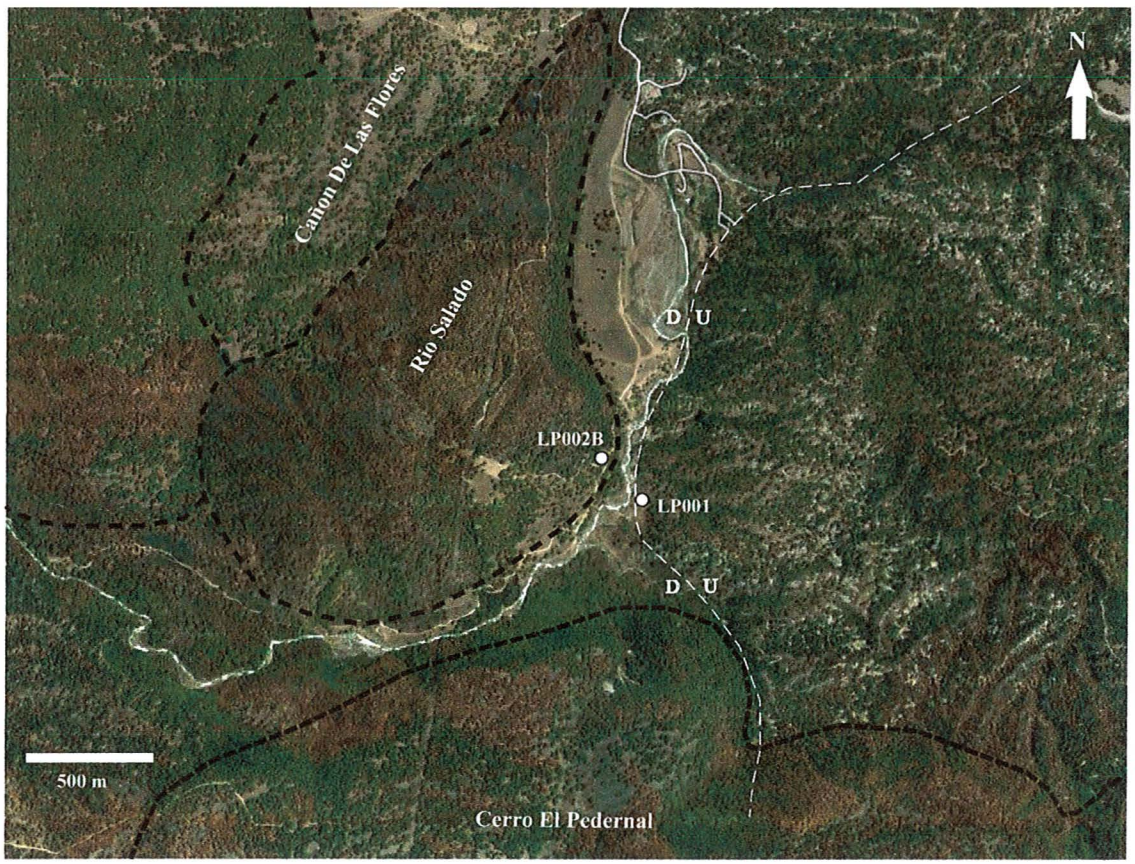

Figure 45 Aerial view map of La Primavera location showing locality of samples LP001 and LP002B with respect to nearby domes. Rio Salado is a pre-caldera lava (~120 ka) and Cerro El Pedernal is a younger ring dome (~75 ka). Sample LP002B was collected within the mapped boundaries of Rio Salado whereas LP001 was collected in an intracaldera area that is primarily composed of uplifted caldera lake sediments. Image is from Google Earth, whereas mapped boundaries are from Mahood (1980).

Table 6 Summary of U-Th chevkinite and zircon isochron and model ages and K-Ar eruption age for analyzed samples.

	Sample			
	LP001	LP002B	LP006	LP008
Chevkinite-whole rock isochron age (ka)	100±120 (MSWD=2.5, N=8)	91±120 (MSWD=3.1, N=8)	-	54±84 (MSWD=3.3, N=8)
Chevkinite mean model age (ka)	$88.5^{40.7}_{29.6}$	$84.0^{40.7}_{29.6}$	-	$49.4^{29.4}_{23.1}$
Zircon internal isochron age (ka)	115±39 (MSWD=0.47, N=11)	113±48 (MSWD=0.7, N=7)	56±24 (MSWD=0.47, N=4)	32±24;102±28** (MSWD=1.6, N=8)
Zircon mean model age (ka)	$104.9^{14.9}_{13.1}$	$113.6^{17.2}_{14.8}$	$74.1^{12.4}_{11.1}$	$101.0^{23.1}_{19.1}$
Chevkinite-zircon isochron age (ka)	102.3±4.1 (MSWD=1.2, N=18)	108.7± 8.2 (MSWD=1.8, N=14)	-	92.0±2.3 (MSDW=2.3, N=14)
K-Ar eruption Age (ka) (Mahood and Drake, 1982)	Unknown dome source	123.3±1.9; 149.6±11.3; <263±87.4*	96.8±3.9	83.6±2.0

** Preferred age for LP008, sample include whole rock composition into age calculation (see chapter VI for discussion)

* Sample error is given as 2σ

Chapter VIII

Conclusion

This study describes a new ion microprobe method for dating the accessory mineral chevkinite based on *in situ* ion microprobe measurement of ^{238}U-^{230}Th radioactive disequilibrium. Analyses of single chevkinite and zircon crystals from four crystal-poor rhyolite samples collected from different localities within the Quaternary La Primavera volcanic complex yield robust isochron and model ages. Chevkinite model and isochron ages for rhyolite samples LP001, LP002B, and LP008 were measured: sample LP001 yields a mean model age of $88.5^{40.7}_{29.6}$ka and a chevkinite-whole rock isochron age of 100 ± 120 ka (MSWD=2.5), sample LP002B yields a mean model age of $84.0^{40.7}_{29.6}$ka and a chevkinite-whole rock isochron age of 91 ± 120 ka (MSWD = 3.1), and sample LP008 yields a mean model age of $49.4^{29.4}_{23.1}$ka and a chevkinite-whole rock isochron age of 54 ± 84 ka (MSWD = 3.3). Zircon model and internal isochron ages for samples LP001, LP002B, LP006, and LP008 were measured: sample LP001 yields a mean zircon model age of $104.9^{14.9}_{13.1}$ka and an internal isochron age of 115 ± 39 ka (MSWD = 0.47), sample LP002B yields a mean model age of $113.6^{17.2}_{14.8}$ka and an internal isochron age of 113 ± 48 ka (MSWD = 0.7), sample LP006 yield a mean model age of $74.1^{12.4}_{11.1}$ka and an internal isochron age of 56 ± 24 ka (MSWD = 0.47), and sample LP008 yields a mean model age of $101.0^{23.1}_{19.1}$ka and a zircon-whole rock isochron age of 32 ± 24 ka (MSWD = 0.7). Finally, the chevkinite-zircon isochron ages for samples LP001, LP002B, and LP008 were calculated using all chevkinite and zircon measurements of each sample: sample LP001 yields a chevkinite-zircon isochron age of 102.3 ± 4.1 ka (MSWD = 1.2), sample LP002B yields a chevkinite-zircon isochron age of

108.7 ± 8.2 ka (MSWD = 1.8), and sample LP008 yields a chevkinite-zircon isochron age of 92 ± 12 ka (MSWD = 2.3). In general, the chevkinite-zircon isochron ages are the most precise.

The results of this research thesis documents the first application of ion microprobe ^{238}U-^{230}Th disequilibrium geochronology using chevkinite from rhyolitic magma. The ages derived from chevkinite and zircon crystals from individual samples are concordant within analytical uncertainties, indicating that ^{238}U-^{230}Th geochronology using chevkinite may be used in lieu of or in combination with zircon in silicic magmas. However, the combination of chevkinite and zircon for isochron dating yields the most precise ages. Compared to the K-Ar ages obtained by Mahood and Drake (1982), the chevkinite-zircon crystallization ages indicate negligible time between crystallization and eruption(i.e.,less than tens of thousands of years). Hence, individual batches of La Primavera rhyolite are likely to have been generated and stored for relatively brief periods prior to eruption.

Works Cited

Bacon, C.R., Persing, H.M., Wooden, J.L., and Ireland, T.R., 2000, Late Pleistocene granodiorite beneath Crater Lake Caldera, Oregon, dated by ion microprobe: *Geology*, v. 28, no. 5, p. 467-470

.

Bacon, C.R., 1989, Crystallization of accessory phases in magmas by local saturation adjacent to phenocrysts: *Geochimicha et Cosmochimicha Acta*, v. 53, p. 1055-1066.

Bailey G., King, G., and Manighetti, I., 2000, Tectonics, Volcanism, Landscape Structure and Human Evolution in the African Rift, in G.N. Bailey, R.Charles and N. Winder (ed.)

Bindeman, I.N., and Valley, J.W., 2001, Low- ^{18}O rhyolites from Yellowstone: magmatic evolution based on analysis of zircons and individual phenocrysts: *Journal of Petrology*, v. 42, p. 1491-1517.

Bohrson, W.A., and Reid, M.R., 1998, Genesis of Evolved Ocean Island Magmas by Deep- and Shallow-Level Basement Recycling, Socorro Island, Mexico: Constraints from Th and other Isotope Signatures: *Journal of Petrology*, v. 39, no. 5, p. 995-1008.

Brown, S.J.A., and Fletcher, I.R., 1999, SHRIMP U-Pb dating of the pre-eruption growth history of zircons form the 340 ka Whakamaru Ignimbrite, New Zealand: evidence for >250 k.y. magma residence times: *Geology*, v. 27, no. 11, p. 1035-1038.

Calvo, C., and Faggiani, R., 1974, A re-investigation of the crystal structure of chevkinite and perrierite: *American Mineralogist*, v. 59, p. 1227-1285.

Charlier, B.L.A., Peate, D.W., Wilson, J.N., Lowenstern, J.B., Storey, M., and Brown, S.J.A., 2003, Crystallization ages in coeval silicic magma bodies: ^{238}U-^{230}Th disequilibrium evidence from the Rotoiti and Earthquake Float eruption Deposits, Taupo Volcanic Zone, New Zealand: *Earth and Planetary Science Letters*, v. 206, pp. 441-457.

Charlier, B., and Zellmer, G., 2000, Some Remarks on U-Th mineral ages from igneous rocks with prolonged crystallization histories: *Earth and Planetary Science Letters*, v. 183, p. 457-469.

Cherniak, D.J., and Watson, E.B., 2003, Diffusion in zircon. *In* Zircon, Reviews in Mineralogy and Geochemistry 53 (J.M. Hanchar, and P.O.W. Hoskin, eds.). The Mineralogical Society of America, Washington, p. 113-143.

Chesner, C.A., and Ettlinger, A.D., 1989, Composition of volcanic allanite from the Toba Tuffs, Sumatra, Indonesia: *American Mineralogists*, v. 74, pp. 750-758.

Condomines, M., Tanguy, J.C., and Allegre, C., 1982, Magmatic evolution of a volcano studied by ^{230}Th-^{238}U disequilibrium and trace elements systematics: the Etna case, *Geochimica et Cosmochimica Acta*, v. 46, pp. 1397-1416.

Costa, F., 2008, Residence times of silic magmas associated with calderas: *Developments in Volcanol*ogy, v. 10, p. 1-55.

Downs, R. T., 2006, The RRUFF Project: an integrated study of the chemistry, crystallography, Raman and infrared spectroscopy of minerals. Program and Abstracts of the 19th General Meeting of the International Mineralogical Association in Kobe, Japan. O03-13

Dicken, A.P., 2005, Radiogenic Isotope Geology: New York, Cambridge University Press, 2nd ed., p. 13, 324-328.

Ferrari, L., Conticelli, S., Vaggelli, G., Petrone, C.M., Manetti., 2000, Late Miocene volcanism and intra-arc tectonics during the early development of the Trans-Mexican Volcanic Belt: *Tectonophysics*, v. 318, pp. 161-185

Fukuoka, T. and Kigoshi, K., 1974, Discordant Io ages and the uranium and thorium distribution between zircon and hosts rocks: *Geochemistry Journal*, v. 8, p. 117-122.

Gill, J. and Condomines, M., 1992, Short-lived radioactivity and magma genesis: *Science*, v. 257, no. 5075, p. 1368-1376.

Green, T.H. and Pearson, N.J., 1988, Experimental crystallization of chevkinite/perrierite from REE-enriched silicate liquids at high pressure and temperature: *Mineralogical Magazine*, v. 52, p. 113-120.

Grew, E.S., and Manton, W.I., 1979, Archean rocks in Antarctica: 2.5-billion-year uranium-lead ages of pegmatites in Enderby Land: Science, v. 206, p.443-445.

Gromet, L.P., and Silver, L.T., 1983, Rare earth element distribution among minerals in a granodiorite and their petrogenetic implications: *Geochimica et Cosmochimica Acta*, v. 47, p. 925-939.

Gunn, B.M., and Mooser, F., 1961, Geochemistry of the volcanics of central Mexico: *Bulletin of Volcanology*, v. 34, 557-614.

Heumann, A., Davies, G.R., and Elliott, T., 2002, Crystallization history of rhyolites at Long Valley, California, inferred from combined U-series and Rb-Sr isotope systematics: *Geochimica et Cosmochimica Acta*, v. 66, no, 10, p. 1821-1837.

Heumann, A., and Davies, G.R., 2002, U-Th disequilibrium and Rb-Sr Age constraints on the magmatic evolution of peralkaline rhyolites from Kenya: *Journal of Petrology*, v. 43, no.3, p. 557-577.

Heaman, L.M., Bowins, R., and Crocket, J., 1990, The Chemical composition of igneous zircon suites: Implications for geochemical tracer studies; *Geochimica et Cosmochimica Acta*, v. 54, p. 1597-1607.

Hildreth W., Christiansen, R.L. and O'Neil, J.R., 1984, Catastrophic isotopic modification of rhyolitic magma at times of caldera subsidence, Yellowstone Plateau volcanic field: *Journal of Geophysical Research*, v. 89, p. 8339-8369.

Hildreth, W., Halliday, A.N., and Christiansen, R.L., 1991, Isotopic and chemical evidence concerning the genesis and contamination of basaltic and rhyolitic magma beneath Yellowstone Plateau volcanic field: *Journal of Petrology*, v. 32, p. 63-138.

Human Ecodynamic: Proceedings of the Association for Environmental Archeology Conference 1998 held at the University of Newcastle upon Tyne, Oxford: Oxbow, p. 31-46.

Ireland, T.R., 1995, Ion microprobe mass spectrometry: Techniques and applications in the cosmochemistry, geochemistry, and geochronology. *Advances in Analytical Geochemistry*, JAI Press 2, Greenwich, pp. 1-118.

Ito, J., 1967, A study of Chevkinite and perrierite. *American Mineralogists*, v. 52, p. 1094-1104.

Izett, G.A., and Wilcox, R.E., 1968, Perrierite, Chevkinite, and Allanite in upper Cenozoic ash beds in the Western United States: *American Mineralogist*, v. 53, p. 1558-1567.

Jiang, N., 2006, Hydrothermal alteration of chevkinite-(Ce) in the Shuiquangou syenitic intrusion, northern China: *Chemical Geology*, v. 227, p. 100-112.

Johnson C.M., Czamanske, G.K. and Lipman, P.W., 1989, Geochemistry of intrusive rocks associated with the Latir volcanic field, New Mexico, and contrasts between evolution of plutonic and volcanic rocks: *Contributions to Mineral Petrology*, v. 103, p. 90-109.

Kauffman, A.J.Jr., and Jaffe, H.W., 1946, Chevkinite (tscheffkinite) from Arizona: *American Mineralogist*, v. 31, p. 582-588.

Lowenstern, J.B., Persing, H.M., Wooden, J.L. Lanphere, M.A., Donnelly-Nollan, J.M., and Grove, T.L., 2000, U-Th dating of single zircons from young granitoid

zenliths; new tools for understanding volcanic processes: *Earth and Planetary Science Letters,* v. 183, p. 291-302.

Ludwig, K.R., 2003, Isoplot/Ex version 3.0. A geochronological tool kit for Microsoft Excel: Berkeley Geochronology Center Special Publication No. 1a, 2455, Ridge Road, Berkeley, CA 94709, USA.

Macdonald, R., Belkin, H.E., Wall, F., and Baginski, B., 2009, Compositional variations in the chevkinite group: new data from igneous and metamorphic rocks: *Mineralogical Magazine,* v. 73, n. 5, p. 777-796.

Macdonald, R., and Belkin, H.E., 2002, Compositional variation in minerals of the chevkinite group: *Mineralogical Magazine*, v. 66(6), p. 1075-1098.

Macdonald, R., Marshall, A.S., Dawson, J.B., Hinton, R.W., and Hill, P.G., 2002, Chevkinite-group minerals from salic volcanic rocks of the East Africa Rift: *Mineralogical Magazine*, v. 66 (2), p. 287-299.

Mahood, G.A., and Halliday, A.N., 1988, Generation of high-silica rhyolite: A Nd, Sr, and O isotopic study of Sierra La Primavera, Mexican Neovolcanic Belt: *Contributions to Mineralogy and Petrology*, 100, p. 182-191.

Mahood, G.A., and Hildred, W., 1983, Large partition coefficients for trace elements in high-silica rhyolites: *Geochimica et Cosmochimica Acta*, v. 47, p. 11-30.

Mahood, G.A., and Drake, R.E., 1982, K-Ar dating young rhyolitic rocks: A case study of the Sierra La Primavera, Jalisco, Mexico: *Geological Society of America Bulletin*, v. 93, p. 1232-1241.

Mahood, G.A., 1981, Chemical evolution of a Pleistocene rhyolitic center: Sierra La Primavera, Jalisco, México: *Contributions to Mineralogy and Petrology*, 77, p. 129-149.

Mahood, G.A., 1980, Geological evolution of a Pleistocene rhyolitic center-Sierra La Primavera, Jalisco, México: *Journal of Volcanology and Geothermal Research*, 8, p. 199-230.

McDowell, S.D., 1979, Chevkinite from the Little Chief Granite, porphyry stock, California: *American Mineralogist*, v. 64, p. 721-727.

Michael, P.J., 1988, Partition coefficients for rare earth elements in mafic minerals of high silica rhyolites: The importance of accessory mineral inclusions: *Geochimica et Cosmochimica Acta*, v. 52, p. 275-282.

Miller, C.F. and Mittlefehldt, 1982, Depletion of light rare-earth elements in felsic magmas: *Geology*, v. 10, no. 3, p. 129-133

Miller, J.S., Matzel, J.E.P., Miller, C.F., Burgess, S.D., and Miller, R. B., 2007, Zircon growth and recycling during the assembly of large, composite arc plutons: *Journal of Volcanology and Geothermal Research*, v. 167, p. 282-299.

Nelson, S.A., and Hagre, JoAnn, 1990, Volcan Las Navajas, a Pliocene-Pleistocene trachyte/peralkaline rhyolite volcano in the northern Mexican volcanic belt: *Bulletin of Volcanology*, v. 52, p. 186-204.

Newhall, C., and Dzurisin, D., 1988, Historical unrest at large claderas of the world: *US Geological Survey Bulletin*, v. 110, p. 1-1108

Oberli, F., Meier, M., Berger, A., Rosenbert, C.L., Giere, R., 2004, U-Th-Pb and $^{230}Th/^{238}U$ disequilibrium isotope systematics: Precise accessory mineral chronology and melt evolution tracing in the Alpine Bergell intrusion: *Geochimica et Cosmochimica Acta*, v. 68, no. 11, p. 2543-2560.

Paces, J.B., and Miller, J.D., 1993, U-Pb ages of Duluth complex and related mafic intrusions, northeastern Minnesota: Geochronological insights to physical, petrogenetic, paleomagnetic, and tectonomagmatic processes associated with the 1.1 Ga mid-continent rift system: *Journal of Geophysical Research*, v. 98, pp. 13997-14013

Rampino, M., R., and Self, S., 1993, Climate-volcanism feedback and the Toba eruption of ~74,000 years ago, *Quaternary Research*, v. 40, pp. 269-280.

Rampino, M.R., and Self, S., 1992, Volcanic winter and accelerated glaciations following the Toba super-Eruption: *Nature*, v. 359, pp. 50-52.

Reagan, M.K., Sims, K.W.W., Erich, J., Thomas, R.B., Cheng, H., Edwards, R.L., Layne, G., and Ball, L., 2003, Times-scales of Differentiation from Mafic Parents to Rhyolite in North American Continental Arcs: *Journal of Petrology*, v. 44, no. 9, p 1709-1726.

Reid, M.R., 2003, Timescales of Magma Transfer and Storage in the Crust: *Treatise on Geochemistry*, Elsevier Ltd, v. 3, p. 167-193.

Reid, M.R., and Coath, C.D., 2000, *In situ* U-Pb ages of zircons from the Bishop Tuff: no evidence for long crystal residence times: *Geology*, v. 28, p. 443-446.

Reid, M.R., Coath, C.D., Harrison, T.M., and McKeegan, K.D., 1997, Prolonged residence times for the youngest rhyolites associated with Long Valley Caldera: ^{230}Th-^{238}U ion microprobe dating of young zircons: *Earth and Planetary Science Letter,* 150, p. 27-39.

Robinson, D.M., and Miller, C.F., 1999, Record of Magma chamber processes preserved

in accessory mineral assemblages, Aztec Wash pluton, Nevada: *The American Mineralogists*, v. 84, p. 1346-1353.

Rogers, N.W., Evans, P.J., Blake, S. Scott, S.C., and Hawkesworth, C.J., 2004, Rates and Timescales of Fractional Crystallization from ^{238}U-^{238}Th-^{226}Ra Disequilibria in Trachyte Lavas from Longonot Volcano, Kenya: *Journal of Petrology*, v. 45, no. 9, p. 1747-1776.

Rossotti, A., Ferrari, L., Lopez-Martinez, M., and Rosas-Elguera, J., 2002, Geology of the boundary between the Sierra Madre Occidental and the Trans-Mexican volcanic Belt in the Guadalajara region, western Mexico: *Revista Mexicana de Ciencias Geologicas*, v. 19, no. 1, pp. 1-15.

Segalstad, T.V., and Larsen, A.O., 1978, Chevkinite and perrierite from Olso region, Norway: *American Mineralogist*, v. 63, p. 499-505.

Scalliet, B., and Macdonald, R., 2001, Phase relations of peralkaline silic magmas and petrogenetic implications: *Journal of Petrology*, v. 42, no. 4, p. 825-845.

Schmitt, A.K., Quaternary Geochronology by SIMS, 2009, *Mineralogical Association of Canada Short Course Series*, v. 41, p. 109-131.

Schmitt, A.K., Stockli, D.F., and Hausback, B.P., 2006, Eruption and magma crystallization ages of Las Tres Virgenes (Baja California) constrained by combined $^{230}Th/^{238}U$ and (U-Th)/He dating of zircon: *Journal of Volcanology and Geothermal Research*, v. 150, pp. 281-295.

Schmitt, A.K., and Vazquez, J.A., 2006, Alteration and remelting of nascent oceanic crust during continental rupture: Evidence from zircon geochemistry of rhyolites and xenoliths from the Salton Trough, California: *Earth and Planetary Science Letters,* 252, p. 260-274.

Schmitt, A.K., Emmermann, R., Trumbull, R.B., Bühn, B., and Henjes-Kunst, F., 2000, Petrogenesis and $^{40}Ar/^{39}Ar$ geochronology of the Brandberg Complex, Namibia: Evidence for a Major Mantle Contribution in Metaluminous and Peralkaline Granites. *Journal of Petrology,* v. 41, no. 8, p. 1027-1239.

Simon, J.I., Vazquez, J.A., Renne, P.R., Schmitt, A.K., Bacon, C.R., and Reid, M.R., 2009, Accessory mineral U-Th-Pb ages and $^{40}Ar/^{39}Ar$ eruption chronology, and their bearing on rhyolitic magma evolution in the Pleistocene Coso volcanic field, California: *Contributions to Mineralogy and Petrology*, no. 158, v. 4, p. 421-446.

Spell, T.L., Y.R. Thousand, M.T. Thirwall, and Campbell A.R., 1993, Isotopic and geochemical constrains on the evolution of postcaldera rhyolites in the Valles caldera, New Mexico: *Journal of Geophysical Research*, v. 98, p. 19723-19739.

Troll, V.R., Sachs, P.M., Schmincke, H.U., and Sumita, M., 2003, The REE-Ti mineral chevkinite in comenditic magmas from Gran Canaria, Spain: a SYXRF-probe study: *Contributions to Mineralogy and Petrology*, no. 145, p. 730-741.

Urrutia-Fucugauchi, J., and Böhnel, H., 1988, Tectonics along the Trans-Mexican volcanic according to paleomagnetic data: *Physics of the Earth and Planetary Interiors*, 52, p. 320-329.

Vazquez, J.A., Kyriazis, S.F., Reid, M.R., Sehler, R.C., and Ramos, F.C., 2008, Thermochemical evolution of young rhyolites at Yellowstone: Evidence for a cooling but periodically replenished postcaldera magma reservoir, *Journal of Volcanology and Geothermal Research*, v. 188, p. 186-196.

Vazquez, J.A., and Reid, M.R., 2004, Probing the accumulation history of the voluminous Toba magma: *Science*, v. 305, p 991-994.

Vazquez, J.A., and Reid, M.R., Time scales of magma storage and differentiation of voluminous high-silica rhyolites at Yellowstone caldera, Wyoming. *Contributions to Mineralogy and Petrology*, v. 144, p. 274-285.

Walker, G.P.L., J.P., Wright, Clough, B.J., and Booth, B., 1981, Pyroclastic geology of the rhyolitic volcano of La Primavera, Mexico: *International Journal of Earth Sciences*, v. 70, no. 3, p. 1100-1118.

Watson, E.B., and Harrison, T.M., 1983, Zircon saturation revisited: temperature and composition effects in a variety of crustal magma types; *Earth and Planetary Science Letters*, v. 64, p. 295-304

Wend, I., and Carl, C., 1991, The statistical distribution of the mean squared weighted deviation; *Chemical Geology (Isotope Geoscience Section)*, v. 86, p. 275-285.

Young, E.J. and Powers, H.A., 1960, Chevkinite in volcanic ash: *The American Mineralogist,* v. 45, p. 875-881.

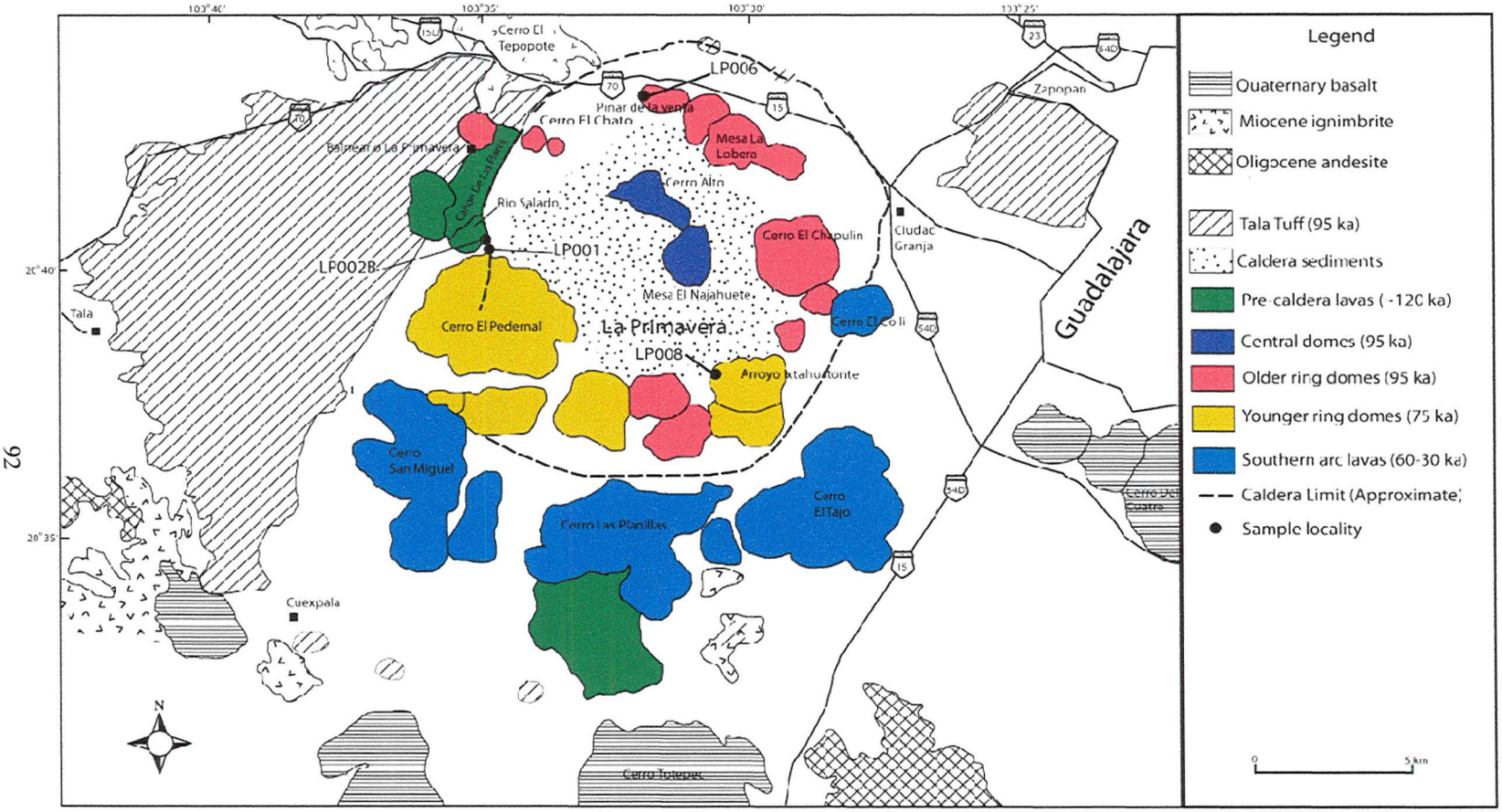

Generalized map of volcanic geology at La Primavera caldera and surrounding areas. For simplicity, only the eruptive units that make up domes within caldera limits are colored. Sample localities are shown by solid circles. Cities are shown by solid squares. After Demant (1978) and Mahood (1980).

Analytical Session: October 1, 2008						
Samples Analyzed: AS3, LP001 Zircon						
Isotope	241.584	243.789	243.789	Zr2 O4	246.02804	244.038
Mass	241.584	243.789	243.789	243.78907	246.02804	244.038
Detector	FC2	H2	FC2	H1	H2	FC2
Analytical Session: Novermber 17, 2008						
Samples analyzed: Arondu, LP001, LP008 Chevkinite						
Isotope	148Nd Ca2 O	246.02804	Th O2	246.3	Th O	U O
Mass	243.836986	246.02804	264.027884	246.3	248.032969	254.0457
Detector	EM	EM	H1	EM	EM	EM
Analytical Session: Novermber 18, 2008						
Samples Analyzed: AS3, LP008 Zircon						
Isotope	243.5	Zr2 O4	244.0381	Zr 92Zr O4	246.02804	246.3
Mass	243.5	243.789066	244.0381	245.789402	246.02804	246.3
Detector	EM	EM	EM	EM	EM	EM
Analytical Session: January 17, 2009						
Samples Analyzed: Arondu, LP002B, LP008 Chevkinite						
Isotope	243.5	Ce Si2 O2	244.03	246.02804	Th O2	246.3
Mass	243.5	227.849117	244.03	246.02804	264.027884	246.3
Detector	EM	L2	EM	EM	H2	EM
Analytical Session: January 18, 2009						
Samples Analyzed: AS3, LP008, LP002B,LP006 zircon						
Isotope	243.5	Zr2 O4	244.0381	Zr 92Zr O4	246.02804	246.3
Mass	243.5	243.789066	244.0381	245.789402	246.02804	246.3
Detector	EM	EM	EM	EM	EM	EM

			Analytical Session: October 1, 2008			
			Samples Analyzed: AS3, LP001 Zircon			
Isotope	244.0381	246.3	248.03	Th O	254.045	U O
Mass	244.03810	246.3	248.03	248.03297	254.045	254.0457
Detector	H1	H2	FC2	H1	FC2	H1
			Analytical Session: Novermber 17, 2008			
			Samples analyzed: Arondu, LP001, LP008 Chevkinite			
Isotope	-	-	-	-	-	-
Mass	-	-	-	-	-	-
Detector	-	-	-	-	-	-
			Analytical Session: Novermber 18, 2008			
			Samples Analyzed: AS3, LP008 Zircon			
Isotope	Th O	U O	-	-	-	-
Mass	248.032969	254.045699	-	-	-	-
Detector	EM	EM	-	-	-	-
			Analytical Session: January 17, 2009			
			Samples Analyzed: Arondu, LP002B, LP008 Chevkinite			
Isotope	Th O	U O	-	-	-	-
Mass	248.032969	254.045699	-	-	-	-
Detector	EM	EM	-	-	-	-
			Analytical Session: January 18, 2009			
			Samples Analyzed: AS3, LP008, LP002B,LP006 zircon			
Isotope	Th O	U O	-	-	-	-
Mass	248.032969	254.045699	-	-	-	-
Detector	EM	EM	-	-	-	-

Appendix 3

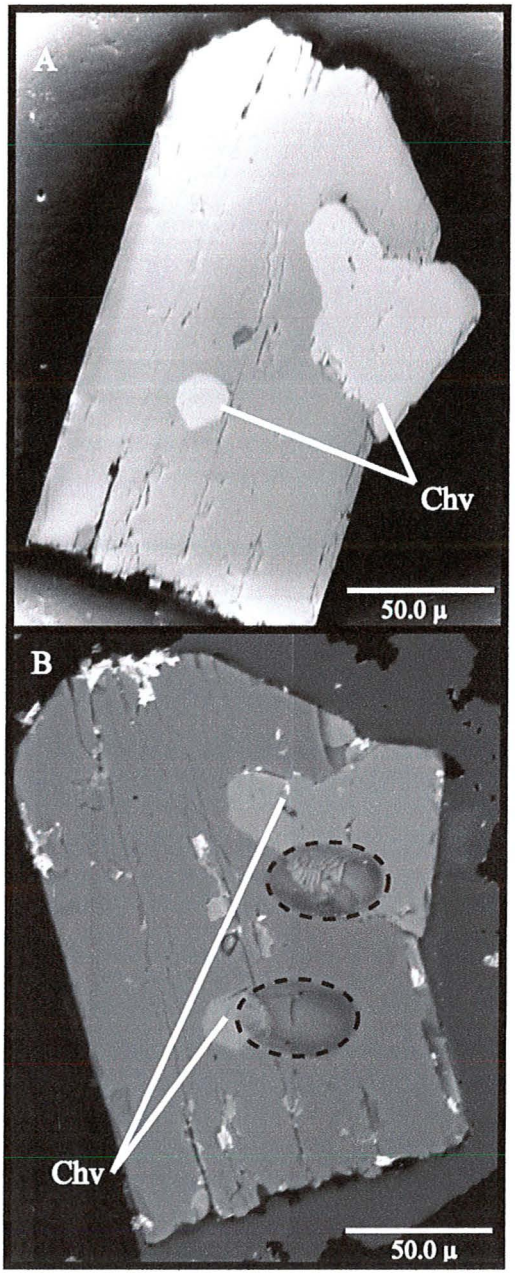

Sample shows chevkinite (Chv) inclusion within a zircon grain before Ion probe analysis (A) and after Ion Probe analysis (B). This particular example shows several points of discussion: 1) Ion beam overlap between chevkinite and zircon creates spurious U/Th ratios that cannot be used to determine crystallization ages. 2) Chevkinite inclusions within zircon grains implies that crystallization of chevkinite occurred shortly after that of zircon. 3) Zircon grains with chevkinite inclusions that can be measured with an Ion Probe would allow to further validate this study. Phenocrysts like the one shown here would have been most useful in determining crystallization ages in our samples; unfortunately they are rare in La Primavera rhyolites.

U-Th isotope data for La Primavera chevkinite

Sample/grain	$(^{238}U)/(^{232}Th)$	1 s.e.	$(^{230}Th)/(^{232}Th)$	1 s.e.	Model Age (ka)	+1σ	-1σ
LP001 (N 20° 40.704'; W 103° 34.711)							
LP001_LPC001B‡	0.093	0.008	0.472	0.025	98.7	45.3	31.9
LP001_LPC002	0.101	0.009	0.504	0.028	91.2	42.6	30.6
LP001_LPC003	0.101	0.009	0.517	0.026	87.7	40.4	29.4
LP001_LPC004	0.102	0.009	0.518	0.025	87.7	40.0	29.2
LP001_LPC005	0.091	0.008	0.520	0.027	85.7	39.1	28.7
LP001_LPC007	0.117	0.010	0.604	0.027	68.6	32.8	25.2
LP001_LPC008	0.100	0.009	0.460	0.025	103.6	48.7	33.6
LP002B (N 20° 40.763'; W 103° 34.776)							
LP002B_LPC_IM_001	0.089	0.008	0.429	0.025	111.1	53.1	35.6
LP002B_LPC_IM_003	0.092	0.009	0.549	0.032	78.6	37.4	27.8
LP002B_LPC_IM_005	0.098	0.009	0.529	0.035	84.3	41.6	30.0
LP002B_LPC_IM_006	0.095	0.009	0.599	0.047	67.6	37.0	27.6
LP002B_LPC_IM_008	0.087	0.008	0.492	0.028	92.2	42.4	30.5
LP002B_LPC_IM_014	0.096	0.009	0.513	0.044	88.1	46.6	32.5
LP002B_LPC_IM_015	0.085	0.008	0.568	0.032	73.2	34.6	26.3
LP008 (N 20° 38.135'; W 103° 30.742)							
LP008_LPC_IM_001	0.111	0.010	0.750	0.069	39.8	32.0	24.7
LP008_LPC_IM_002	0.110	0.010	0.791	0.050	32.9	25.6	20.7
LP008_LPC_IM_004	0.090	0.008	0.587	0.045	69.5	36.8	27.5
LP008_LPC_IM_003	0.104	0.010	0.665	0.043	54.8	31.0	24.1

U-Th isotope data for La Primavera chevkinite (continued)

Sample/grain	$(^{238}U)/(^{232}Th)$	1 s.e.	$(^{230}Th)/(^{232}Th)$	1 s.e.	Model Age (ka)	+1σ	-1σ
LP008_LPC001	0.109	0.009	0.665	0.043	55.2	31.3	24.3
LP008_LPC002	0.096	0.008	0.609	0.033	65.4	32.2	24.8
LP008_LPC004	0.098	0.008	0.767	0.037	36.3	23.5	19.3

Activity calculations using decay constants: $\lambda_{230}= 9.1577 \times 10^{-6}$ year^{-1}; $\lambda_{232}= 4.9475 \times 10^{-11}$ year^{-1}; $\lambda_{238}= 1.55125 \times 10^{-10}$ year^{-1}

Instrumental mass fractionation value for standards were obtained for individual sessions and described in chapter V.

Each measurement comes from an individual chevkinite crystals.

Whole rock values used: $(^{230}Th)/(^{232}Th)= 1.03\pm 0.09$, $(^{238}U)/(^{232}Th)= 1.03\pm 0.09$; calculation discussed in Figure 21.

s.e. (standard error) = 1σ or 68% confidence level.

Table 2 U-Th isotope data for La Primavera Zircon

Sample/grain	$(^{238}U)/(^{232}Th)$	1 s.e.	$(^{230}Th)/(^{232}Th)$	1 s.e.	Model Age (ka)	+1σ	-1σ	U (ppm)
	LP001 (N 20° 40.704'; W 103° 34.711)							
LP001r3g003s1	5.007	0.153	3.422	0.076	100.4	16.4	14.3	1774
LP001r3g004s1	5.731	0.176	3.970	0.072	107.2	15.4	13.5	2442
LP001r3g008s1	5.520	0.166	3.754	0.098	101.9	16.2	14.1	2424
LP001r3g009s1	6.240	0.186	4.281	0.089	106.8	14.8	13.0	1954
LP001r3g009s2	5.883	0.176	4.145	0.069	112.1	15.8	13.8	2598
LP001r4g010s1	6.497	0.193	4.335	0.099	101.3	13.7	12.2	1771
LP001r4g011s1	7.246	0.215	4.711	0.127	98.0	12.9	11.5	1299
LP001r4g014s1	5.461	0.167	3.677	0.068	99.4	14.4	12.7	2392
LP001r4g015s1	5.473	0.174	3.855	0.070	110.3	16.9	14.6	3069
LP001r3g006s2	7.258	0.216	4.854	0.129	103.9	14.0	12.4	2270
LP001r4g007s1	7.159	0.215	5.005	0.105	114.2	15.1	13.3	1619
	LP002B (N 20° 40.763'; W 103° 34.776)							
LP0082B_LPZ_ZM_001	5.710	0.157	4.133	0.088	118.8	18.2	15.6	1795
LP0082B_LPZ_ZM_002	6.912	0.190	4.958	0.112	120.3	16.6	14.4	1312
LP0082B_LPZ_ZM_003	4.965	0.137	3.602	0.072	115.8	19.2	16.3	2285
LP0082B_LPZ_ZM_004	4.991	0.146	3.586	0.072	113.2	18.8	16.0	2483
LP0082B_LPZ_ZM_006	6.547	0.180	4.435	0.132	104.8	15.4	13.5	1266
LP0082B_LPZ_ZM_007	6.092	0.168	4.135	0.096	103.7	14.6	12.8	1552
LP0082B_LPZ_ZM_008	5.865	0.162	4.244	0.109	119.3	19.1	16.2	1581

Table 2 U-Th isotope data for La Primavera zircon
(continued)

Sample/grain	$(^{238}U)/(^{232}Th)$	1 s.e.	$(^{230}Th)/(^{232}Th)$	1 s.e.	Model Age (ka)	+1σ	-1σ	U (ppm)
	LP006 (N 20° 43.232'; W 103° 31.960)							
LP006_LPZ_ZM_002	6.400	0.183	3.504	0.143	67.4	10.5	9.5	692
LP006_LPZ_ZM_002	6.518	0.201	3.733	0.147	74.1	11.4	10.4	693
LP006_LPZ_ZM_004	5.117	0.196	3.057	0.096	74.8	13.2	11.8	929
LP006_LPZ_ZM_005	4.275	0.121	2.741	0.080	81.9	15.5	13.6	896
	LP008 (N 20° 38.135'; W 103° 30.742)							
LP008_LPZ_ZM_001	4.191	0.127	3.214	0.064	128.2	27.1	21.7	2824.5
LP008_LPZ_ZM_002	4.922	0.143	3.292	0.120	95.0	18.1	15.6	964.2
LP008_LP_Zr_001	5.293	0.269	3.480	0.314	93.4	31.4	24.4	1122.1
LP008_LP_Zr_002	4.188	0.214	3.134	0.157	119.9	39.5	28.9	2194.8
LP008_LP_Zr_003	5.545	0.282	3.594	0.161	91.6	20.1	17.0	1164.2
LP008_LP_Zr_004	5.296	0.270	3.560	0.154	98.2	22.6	18.7	1595.7
LP008_LP_Zr_005	5.397	0.275	3.404	0.168	85.7	19.5	16.5	1349.9

Activity calculations using decay constants: $\lambda_{230} = 9.1577 \times 10^{-6}$ year^{-1}; $\lambda_{232} = 4.9475 \times 10^{-11}$ year^{-1}; $\lambda_{238} = 1.55125 \times 10^{-10}$ year^{-1}

Instrumental mass fractionation value for standards were obtained for individual sessions and described in chapter V.

*Different spots measured on same zircon crystal, all other measurement comes from an individual zircon crystals.

Whole rock values used: $(^{230}Th)/(^{232}Th) = 1.03 \pm 0.09$, $(^{238}U)/(^{232}Th) = 1.03 \pm 0.09$; calculation discussed in Figure 21.

s.e. (standard error) = 1σ or 68% confidence level